Critical Evaluation and Thermodynamic Modeling of Phase Equilibria in the Fe-Ca-Mg-Mn-Al-Si-O System

SAIKAT CHATTERJEE

Mining and Materials Engineering Department
McGill University, Montreal

APRIL 2013

A thesis submitted to McGill University in partial fulfillment of the requirements of the degree of MASTER OF SCIENCE (M.Sc.)

ACKNOWLEDGEMENTS

I would like to acknowledge and express my heartfelt gratitude to Dr. In-Ho Jung, whose continuous guidance and support made the completion of this work possible. He not only supervised me, but also challenged and encouraged me to work harder. I would also like to thank him for his helpful advices and constructive criticism.

I also want to thank all my group members for being like a second family to me. I would like to express my appreciation to all my friends and colleagues in lieu of the help and support I received from them. They have been very supportive whenever I faced a problem during my stay in Canada. I will always remain indebted to them.

I am grateful to have a very supportive family back in India and I would like to dedicate the thesis to them. They have never ceased to offer me the moral support to complete my study.

The present study is a part of a bigger project which is funded by National Sciences and Engineering Research Council of Canada in collaboration with Tata Steel, Hyundai Steel, Posco, Nucor Steel, Rio Tinto, Sumitomo Metals, JFE Steel Corporation, Nippon Steel, RHI and Voest Alpine. I would like to express my thankfulness to all of them for the financial support.

ABSTRACT

The knowledge of phase equilibria and thermodynamic properties of liquid and solid oxides can help us better understand metallurgical, ceramic or geological processes. The main aim of the present study is the critical evaluation and thermodynamic optimization of solid and liquid (MnO-Al_2O_3 based) oxides which are of interest to the steelmaking and ferro-Mn industries. These newly developed databases coupled with the previous databases can be used along with any software for Gibbs energy minimization to predict the phase relationships and the thermodynamic properties of any relevant system. Usually, thermodynamic databases can save both cost and time, which, otherwise would have been spent to optimize the existing process and develop any new process.

The production of steels with higher amounts of manganese and aluminum has gained considerable importance in the recent past. Steels with high concentration of manganese and aluminum like TWIP steel and TRIP steel have exceptional properties which classify them as special steels; needless to say the various range of applications they can cater to. Ferromanganese, which contains a large amount of manganese, is also a very useful product required in the production of high manganese steels. The production of these alloys results in the generation of slags which are rich in MnO and Al_2O_3. Hence, knowledge of the phase relations between these two components is of utmost importance in order to maximize the efficiency of the production process. Only a very good knowledge of Gibbs energy of all the phases present in the binary system MnO-Al_2O_3 can allow us to predict the correct equilibrium conditions during the production process.

The critical evaluation and thermodynamic optimization of all the available phase diagram data and thermodynamic properties of the system Mn-Al-O have been carried out in the first part of the present work. Thermodynamic modeling for different phases such as slag, spinel (cubic and tetragonal) and bixbyite has been performed using Modified Quasichemical Model, Compound Energy Formalism and random mixing model, respectively. The sublattice structure of solid solution phases were properly taken into account in the thermodynamic modeling and their thermodynamic properties and structural data were reproduced using the physically meaningful

model parameters. All the reliable experimental data of the Mn-Al-O system were reproduced within error limits from room temperature to above the liquidus temperatures at all compositions and oxygen partial pressure ranging from metal saturation to air. The present $MnAl_2O_4$-Mn_3O_4 spinel solutions can be integrated with all the other spinel solutions developed earlier to obtain an extensive spinel solution database. This database along with the software for Gibbs energy minimization can be utilized to perform various calculations and predict the phase relations at any given condition.

In the next part of the present work, the binary MnO-Al_2O_3 system was extended to the higher order systems like MnO-Al_2O_3-SiO_2, CaO-MnO-Al_2O_3, FeO-MnO-Al_2O_3, MgO-MnO-Al_2O_3 and CaO-MnO-Al_2O_3-SiO_2. Other calculations related to inclusion engineering in steelmaking were also carried out. This was done to check the accuracy of the database developed for the binary MnO-Al_2O_3 system.

The database of model parameters can be used with thermodynamic software like Factsage for thermodynamic modeling of various industrial and natural processes. Calculations pertaining to prediction of thermodynamic properties of phases, cation distribution in spinel solutions, phase equilibria at any temperature, composition and oxygen partial pressure where no experimental data are available can also be performed.

RÉSUMÉ

La connaissance des équilibres de phase et des propriétés thermodynamiques des oxydes solides et liquides peut aider à mieux comprendre les processus métallurgiques, céramiques et géologiques. Le but principal de la présente étude est l'évaluation critique et l'optimisation thermodynamique des oxydes solides et liquides impliquant MnO-Al_2O_3 qui sont d'intérêt pour les industries de l'acier et du ferromanganèse. Les nouvelles bases de données développées, couplées avec d'anciennes bases de données, peuvent être utilisées avec n'importe quel logiciel de minimisation de l'énergie de Gibbs pour prédire les équilibres de phase et les propriétés thermodynamiques de tout système pertinent. Habituellement, les bases de données permettent de sauver temps et argent qui, autrement, auraient pu être utilisés pour optimiser des processus existant et en développer de nouveaux.

La production d'aciers à teneur élevé en manganèse et aluminium a récemment acquis une importance considérable. Les aciers à teneur élevé en manganèse et aluminium, comme l'acier TWIP et l'acier TRIP, ont des propriétés exceptionnelles qui les classifient comme aciers spéciaux; inutile de mentionner le large éventail d'applications auxquels ils peuvent répondre. Le ferromanganèse, qui contient de grandes quantités de manganèse, est aussi un produit très utile dans la production d'aciers à haute teneur de manganèse. La production de tels aciers génère des scories riches en MnO et Al_2O_3. Par conséquent, la connaissance des relations de phases entre ces deux composés est d'une importance capitale pour maximiser l'efficacité du processus de production. Seule une bonne connaissance de l'énergie de Gibbs de toutes les phases présentes dans le système MnO-Al_2O_3 peut nous permettre de prédire les conditions correctes d'équilibre lors du processus de production.

L'évaluation critique et l'optimisation thermodynamique de toutes les données disponibles de diagrammes de phase et de propriétés thermodynamiques du système Mn-Al-O ont été réalisées dans la première partie de ce travail. La modélisation thermodynamique des différentes phases telles que le laitier, le spinelle (cubique et tétragonal) et la bixbyite a été respectivement effectuée à l'aide du Modèle Quasichimique Modifié, du Formalisme de l'Énergie des Composés et du modèle de mélange aléatoire. La structure du sous-réseau des solutions solides fut correctement prise en compte dans la modélisation thermodynamique et les propriétés

thermodynamiques et données structurales furent reproduites en utilisant des paramètres ayant une signification physique. Toutes les données expérimentales fiables du système Mn-Al-O ont été reproduites à l’intérieur des limites d’erreur de la température ambiante à au-dessus du liquidus pour toutes les compositions et à des pressions partielles d’oxygène allant de la saturation en métal jusqu’à l’air. Les solutions de spinelle $MnAl_2O_4$-Mn_3O_4 peuvent être intégrées à toutes les autres solutions de spinelle développées antérieurement afin d’obtenir une base de données étendue pour le spinelle. Cette base de données, combinée à un logiciel de minimisation de l'énergie de Gibbs, peut être utilisée pour effectuer divers calculs et prédire les relations de phase dans n'importe quelles conditions données.

Dans la seconde partie de ce travail, le système binaire MnO-Al_2O_3 a été ajouté aux systèmes d'ordre supérieur tels que MnO-Al_2O_3-SiO_2, CaO-MnO-Al_2O_3, FeO-MnO-Al_2O_3, MgO-MnO-Al_2O_3 et CaO-MnO-Al_2O_3-SiO_2. Des calculs liés à l'ingénierie des inclusions impliquées dans la fabrication de l’acier ont également été effectuées. Ceci a été fait pour vérifier l'exactitude de la base de données développée pour le système binaire MnO-Al_2O_3.

La base de données des paramètres du modèle peut être utilisée avec un logiciel de thermodynamique comme FactSage pour la modélisation thermodynamique de divers procédés industriels et naturels. Les calculs relatifs à la prédiction des propriétés thermodynamiques des phases, la distribution des cations dans les solutions spinelle et les équilibres entre phases à n'importe quelle température, composition et pression partielle d'oxygène où aucune donné expérimentale n’est disponible, peuvent également être effectuées.

TABLE OF CONTENTS

LIST OF TABLES

LIST OF FIGURES

LIST OF SYMBOLS

C_p	Molar Heat Capacity (J/mol-K)
$G^o{}_i$	Standard Gibbs energy of *i*
G^m	Gibbs energy of solution
G^E	Excess Gibbs energy in solution
g^E	Molar excess Gibbs energy in Solution
$g^o{}_i$	Molar Gibbs energy of *i*
Δg_{ij}	Gibbs energy change for the formation of two moles of *i*-*j* pairs
$H^o{}_i$	Standard enthalpy of *i*
ΔH	Molar enthalpy of mixing
ΔH_T	Enthalpy of formation of the compound from the elements
n_{ij}	Number of moles of *i*-*j* bonds in one mole of the solution
$q^{ij}{}_{AB}$	Excess interaction parameter between A and B
$S^o{}_i$	Standard entropy of component *i*
ΔS_T	Entropy of formation of the compound from the elements
ΔS^{conf}	Molar configurational entropy of solution
$S^{non-conf}$	Molar non-configurational entropy of solution
n_i	Number of moles of component *i*
T	Absolute temperature (K)
wt.%	Weight percent
y_i	Site fraction of component *i*
Y_i	Coordination-equivalent fractions
X_i	Mole fraction of component *i* in solution
X_{ij}	Pair fraction of *i*-*j* pairs
Z_i	Coordination number of *i*
I_{ij}	Inversion model parameters for a reaction: $G_{jj} + G_{ji} - 2G_{ij}$
Lij:k	Interaction energies between cations *i* and *j* on one sublattice when the other sublattice is occupied only by k cations.
Δij	Exchange reaction model parameters for a reaction: $G_{ii} + G_{jj} - G_{ij} - G_{ji}$
Δijk	Exchange reaction model parameters for a reaction: $G_{ii} + G_{ik} - G_{ij} - G_{jk}$

Chapter 1

Introduction

Computational thermodynamics have taken a huge leap ahead in the last few decades with the development of computer power. Since then, there have been numerous applications of computational thermodynamics to industrial processes. The availability of an extensive and accurate thermodynamic database is a prerequisite for proper thermodynamic calculations in complex systems. The present study aims at extending the present FactSage [1] oxide databases which can be later used for numerous applications. Prediction of thermodynamic properties and phase equilibria in multicomponent systems is necessary to understand the reaction mechanisms of various industrial processes. This can help us in bringing about considerable improvements and developing new technologies in industries. Numerical simulation is gaining widespread acceptance in almost all industrial applications as this is a powerful tool which helps save both money and time, which would have, otherwise, been spent on performing real experiments. In order to keep pace with the industrial processes, proper thermodynamic models and databases must be developed which would be able to predict the thermodynamic properties and phase equilibria in complex systems.

The aim of the present study is to create an extensive thermodynamic database for multicomponent oxide systems of industrial interest. All the available experimental data in the literature are critically evaluated and this is followed by thermodynamic optimization of the given chemical system which is done by obtaining one set of model equations for the Gibbs energies of all the phases as functions of temperature and composition. The success of this method depends on the choice of the model. The model should predict the Gibbs energy of the phase in a reliable and convenient manner.

The main purpose of the present study is to model the $MnAl_2O_4$ spinel solid solution properly considering the excess solubility of Al_2O_3. Then, the oxide systems containing $MnAl_2O_4$ spinel solution are reoptimized. This includes:

i.) MnO-Mn_2O_3-Al_2O_3
ii.) MnO-Mn_2O_3-Al_2O_3-SiO_2
iii.) MnO-Mn_2O_3-Al_2O_3-SiO_2-CaO
iv.) MnO-Mn_2O_3-Al_2O_3-MgO
v.) MnO-Mn_2O_3-Al_2O_3-FeO

References

[1] FactSage 6.3, www.factsage.com, Montreal, Canada, 2012.

Chapter 2

Thermodynamic modeling

2.1 History of CALPHAD

CALPHAD, an abbreviation for CALculation of PHAse Diagrams, means Computer Coupling of Phase Diagrams and Thermochemistry. Phase diagram is an important tool which helps us understand the thermodynamic phase equilibria that exists between multiple phases. Real industrial processes, almost always, involve multicomponent systems whose phase diagrams are not very well known. The construction of phase diagrams for multicomponent systems based only on experiments is very difficult and time consuming. Hence, an attempt was made to construct multicomponent thermodynamic databases in the late 1960's by using the advancing computational powers. The creation of multicomponent databases would help in understanding the phase equilibria and thermodynamic properties of multicomponent systems in a better manner.

CALPHAD method has been used by several large research groups across the worlds that perform thermodynamic modeling of large systems. The Thermo-Calc group [1] in Sweden, the THERMODATA group [2] in France, Thermotech Inc. [3] in UK, the thermochemical group at NIST [4] in USA, the FACT group (Bale *et al.* [5], Factsage [6]) in Canada, the MTDATA group [7] in UK and the IRSID group in France are some of the well-known groups in this field. The Scientific Group Thermodata Europe [8] was organised as a consortium of research groups to accelerate the development of alloy databases. These groups have developed several useful softwares and databases which have had useful applications in academic and industrial scales.

2.2 The CALPHAD technique

The CALPHAD technique for the thermodynamic database development includes the following steps:

a. Definition of the system which is to be thermodynamically optimized.

b. Collection of all available experimental data in literature: Experimental data includes thermodynamic data, phase diagram data, crystal structure data and if necessary, data related to physical properties.

  i. Thermodynamic data: vapour pressure, chemical potential, activity, heat capacity, enthalpy, etc.
  ii. Phase diagram data: isothermal phase diagram, liquidus projection, isopleths, etc.
  iii. Crystal structure data: cation distribution between different sublattices, lattice parameters, etc.
  iv. Physical properties: magnet data, conductivity, etc.

Moreover, useful data from higher order systems can be interpolated for sub-systems that have very few or no experimental data at all.

c. Selection of proper models:
The choice of a proper thermodynamic model based on the structure of the phase is of utmost importance. This is because only a proper model can yield good predictions for the multicomponent solution properties from the model parameters optimized for model parameters.

d. Critical evaluation of experimental data:
The experimental data on the same system might differ from article to article. Also, two different articles might report different types of experimental data which are actually, connected in terms of Gibbs energy. Hence, all the reported literature data must be evaluated critically based on the sample preparation techniques, experimental conditions involved, experimental and analytical techniques used, etc. The accuracy of the data can be often judged during the optimization of the entire system and in some cases the accuracy of the data in lower-order systems can be evaluated from the data in higher-order systems by interpolation.

e. Optimization of the model parameters:

The next step after the evaluation of experimental data is optimization of the minimum number of reasonable model parameters for each phase. Once back-calculation reproduces the reliable experimental data within the experimental error limits, the optimization process can be considered to be complete.

f. Back-calculation of all thermodynamic and phase diagram data:

Any type of thermodynamic calculations can be made by utilizing the optimized model parameters for each phase. The FactSage^{TM} (FactSage 6.3)[12Fac] thermochemical software was used in the present study to perform all the calculations.

References

[1] Thermo-Calc, www.thermocalc.com, Stockholm, 2002.

[2] THERMODATA, 2002. www.thermodata.online.fr, Grenoble.

[3] Thermotech, 2002. www.thermotch.co.uk, Surrey, UK.

[4] NIST, www.nist.gov, Gaithersburg, 2002.

[5] C. W. Bale, P. Chartrand, S. A. Degterov, G. Eriksson, K. Hack, R. B. Mahfoud, J. Melancon, A. D. Pelton, S. Petersen, "FactSage thermochemical software and databases," *Calphad*, **26**, 189-228 (2002).

[6] FactSage 6.3, www.factsage.com, Montreal, Canada, 2012.

[7] MTDATA, www.npl.co.uk, Teddington, UK, 2002.

[8] SGTE, www.sgte.org, 2002.

Chapter 3

Thermodynamic models

The thermodynamic model for a particular solution should be chosen based on its actual structure. Each thermodynamic model for solution has different function to calculate entropy of solution, which is one of the key factors affecting the Gibbs energy of solution. Therefore, different models can be used for different solutions depending on the crystal structure of the solution. A good model is one which can describe all the thermodynamic properties with the help of a small number of model parameters. The model also has a high predictive ability when it is based on the real structure of the solution.

General relations between thermodynamic properties

Pure substances:

The standard Gibbs energy of a pure component 'i' is written as:

$$G_i^o = H_i^o - TS_i^o \tag{3.1}$$

where G_i^o, H_i^o and S_i^o are the standard Gibbs energy, enthalpy and entropy of component 'i' respectively and T is the absolute temperature.

Bragg-Williams Random Mixing Solution:

Let us consider a solution of two components A and B. When the components are mixed randomly, the entropy of the solution can be expressed by the Bragg-Williams random entropy function. The Gibbs energy of the solution is also affected by the interactions between A and B. We assume that there is no interaction between the constituent components for an ideal solution. The Gibbs energy of an ideal solution can be written as:

$$g^m = (g_A^O X_A + g_B^O X_B) - T\Delta S^{config} \tag{3.2}$$

$$\Delta S^{config} = -R(X_A \ln X_A + X_B \ln X_B) \tag{3.3}$$

where g^m is the molar Gibbs energy of solution, g_i^o is the molar Gibbs energy of the component 'i', ΔS^{config} is the molar configurational entropy of solution and X denotes the mole fraction of any component.

When the interactions between the components are not zero, so the Gibbs energy of solution can be written as:

$$g^m = (g_A^O X_A + g_B^O X_B) - T\Delta S^{config} + g^E \tag{3.4}$$

where G^E is the excess molar Gibbs energy which can be expanded as a polynomial in the mole fractions as:

$$g^E = \sum_{ij} q_{AB}^{ij} X_A^i X_B^j \tag{3.5}$$

where q_{AB}^{ij} terms represent the excess interaction parameters which can be expanded in terms of temperature as a + bT + cT^2+…...

If only q_{AB}^{11} is used to describe the thermodynamic properties of a solution, it is known as a "regular" solution. If q_{AB}^{ij} terms are dependent on temperature then the non-configurational entropy term is non-zero.

In the present study, solution phases such as liquid slag, spinel, bixbyite and monoxide are described using specific thermodynamic models which are based on the real liquid or crystal structures of the solutions.

3.1 Spinel

3.1.1 Crystal structure

Spinel belongs to the space group $Fd\overline{3}m$. The structure of spinel is shown schematically in Fig. 3.1. In the AB_2O_4 unit cell, A atoms are located in the 8 tetrahedral positions (represented by green circles in the Fig. 3.1), B atoms in the 16 octahedral positions (represented by red circles) and oxygen atoms in the 32 positions (represented by blue circles). Since the unit cell contains 32 oxygen atoms, so, there are eight AB_2O_4 formula units. The lattice parameters in oxide spinels generally ranges between 0.8 – 0.9 nm. A simple spinel usually contains two different cations A^{2+} and B^{3+} in the ratio 1:2. All spinels may be classified theoretically into three classes, normal, inverse and mixed based on the distribution of cations in the sites. A normal spinel is one in which the more abundant (B^{3+}) cations reside in the octahedral sites, whereas a fully inverse spinel is one in which the B cations are evenly split between tetrahedral and octahedral sites. However, all real spinels generally fall in the category of 'mixed spinels', i.e. both the cations in a simple spinel are present in both tetrahedral and octahedral sites.

All the well-known spinels, e.g., $MgAl_2O_4$ (spinel), $MnAl_2O_4$ (galaxite), Fe_3O_4 (magnetite), $FeAl_2O_4$ (hercynite), $FeCr_2O_4$ (iron chromite), $MgFe_2O_4$ (magnesium ferrite), $MgCr_2O_4$ (magnesium chromite), $CoAl_2O_4$, $NiAl_2O_4$, $ZnAl_2O_4$, $NiFe_2O_4$ are stable at 1 bar total pressure. However, some spinels are stable at high-pressures because, the olivine structure (A_2SiO_4) transforms to spinel structure at high-pressures. The oxide spinels can dissolve oxides of the type γ-A_2O_3, e.g., γ-Al_2O_3, γ-Fe_2O_3, γ-Cr_2O_3, etc. This leads to the introduction of vacancies in the octahedral sites which eventually results into wide ranges of solid solution.

The distributions of the cations in a spinel structure vary with the temperature. Now, we will define two terms (unquenchable temperature and frozen temperature) in order to elucidate the variation of cation distribution with temperature. The unquenchable temperature, abbreviated as $T_{unquench}$, is the minimum temperature above which cation distribution between the tetrahedral and octahedral sites is unquenchable. The reason for this is that the ordering-disordering process is fast at this temperature and quenching is not a good choice to get a proper value for cation distribution. The frozen temperature, abbreviated as T_{froz}, is the maximum temperature below which an equilibrium distribution of cations is not reached because the ordering-disordering process becomes slow at this temperature. Jung [1] concluded that T_{froz} in the case of $MgAl_2O_4$

spinel was found to be around 973K (i.e. as those samples were cooled from a temperature lower than 973K, the cation distribution for the spinel was found to be frozen). Similarly, he concluded that the $T_{unquench}$ was around 1200K as the high-temperature cation distribution could not be retained by quenching. The probable solution to this problem is *in situ* measurements.

In case of spinels like Fe_3O_4 (magnetite), $FeAl_2O_4$ (hercynite), $FeCr_2O_4$ (iron chromite), etc. which have ferro- or antiferro-magnetic properties or other anomalies, special considerations must be made during the thermodynamic modeling of the spinel solutions.

3.1.2 Compound Energy Formalism (CEF) for spinel solid solution

The two-sublattice spinel model given by Degterov *et al.* [2] in the framework of the Compound Energy Formalism (CEF) (Hillert *et al.* [3]) has been used to model the spinel phase in the present study. The Gibbs energy of spinel solution in the CEF per formula unit can be expressed as:

$$G = \sum_i \sum_j y_i^T y_j^O G_{ij} - TS^{config} + G^{excess} \tag{3.6}$$

where, $\mathrm{y_i^T}$ and $\mathrm{y_j^O}$ represents the site fractions of cations in the tetrahedral and octahedral sites respectively; G_{ij} is the Gibbs energy of any end-member $(i)^{\mathrm{T}}[j]_2^O\mathrm{O_4}$ in which cation 'i' occupies the tetrahedral site and cation 'j' occupies the octahedral site; S^{config} is the configurational entropy which takes into account the random mixing of the cations on each sublattice and it can be expressed as:

$$S^{config} = -R(\sum_i y_i^T \ln y_i^T + 2\sum_j y_j^O \ln y_j^O) \tag{3.7}$$

G^{excess} (G^E) is expressed as:

$$G^E = \sum_i \sum_j \sum_k y_i^T y_j^T y_j^O L_{ij:k} + \sum_i \sum_j \sum_k y_k^T y_i^O y_j^O L_{k:\mathrm{ij}} \tag{3.8}$$

where, $L_{ij:k}$ parameters denote the interaction between cations 'i' and 'j' on the first sublattice when the second sublattice is occupied only by 'k' cations and similarly the parameters $L_{k:ij}$ denote the interaction between cations 'i' and 'j' on the second sublattice when the first sublattice is occupied only by 'k' cations. One important assumption according to the model is that the interaction between the same two cations present on one sublattice will not change on changing the cation on the other sublattice, i.e.,

$$L_{k:ij} = L_{l:ij} = ... \tag{3.9}$$

$$L_{ij:k} = L_{ij:l} = ... \tag{3.10}$$

Redlich-Kister power series expansions given by Redlich and Kister [4] and Pelton and Bale [5] can be used to express the dependence of interaction energies on composition as follows:

$$L_{ij:k} = \sum_{m} {}^{m}L_{ij:k} (y_j^T - y_i^T)^m \tag{3.11}$$

$$L_{k:ij} = \sum_{m} {}^{m}L_{k:ij} (y_j^O - y_i^O)^m \tag{3.12}$$

The end-member Gibbs energies G_{ij} are used to describe the concerned system. However, it is difficult to experimentally determine all the end-member Gibbs energies. Certain linear combinations of the end-member Gibbs energies pertaining to certain site exchange reactions occurring between the cations present in the system were chosen as the model parameters. High predictive ability of the model could be obtained in this case. Moreover, it's more reasonable and logical to choose combinations of G_{ij}, which have certain physical significance, as the model parameters rather than fixing the G_{ij} to some arbitrary value. $G_{AB} = G^O(\mathrm{AB_2O_4})$, the measurable Gibbs energy of pure normal AB_2O_4 is used as a model parameter for a fully normal spinel.

The combinations of Gibbs energies are actually the Gibbs energies of site exchange reactions of the cations present in the tetrahedral and octahedral sites and they are usually denoted as Δ and I parameters.

The Gibbs energies similar to the following reaction:

$$AB + BA = AA + BB \tag{3.13}$$

given by Δ_{AB} (= $G_{AA} + G_{BB} - G_{AB} - G_{BA}$) are used as model parameters. O'Neill and Navrotsky [6] found out that the parameters should have values of about 40kJ/mol.

Inversion (I) parameters, described as:

$$I_{AB} = G_{BB} + G_{BA} - 2G_{AB} \tag{3.14}$$

usually determine the cation distribution of the spinels.

The present study is concerned mainly with the modeling and optimization of spinel containing Mn in variable valency states such as 2+, 3+, and 4+. Therefore, the structure of the spinel solution and the Gibbs energy functions are more complex. These things will be elaborated in chapter 4.

3.2 Slag (molten oxide)

3.2.1 Structure

Fig. 3.2 shows the structure of sodium silicate glass by Warren and Biscoe [7]). The silicon atoms are surrounded by 4 oxygen atoms which are arranged in the form of a tetrahedron. The Si and O atoms form SiO_4 tetrahedra which forms chains or rings joined by bridging oxygens (BO). Cations such as Na^+, Fe^{2+}, Mn^{2+}, Ca^{2+}, etc. tend to break these BO and form non-bridging oxygens (NBO), O^-, or free oxygen ions, O^{2-}. The silicate melt contains various 3 dimensional interconnected anion units such as SiO_4^{4-}, $Si_2O_5^{2-}$, etc. which are observed in the melt. If T is the number of tetrahedrally coordinated atoms such as Si, then the ratio ‘NBO/T’ signifies the degree of depolymerisation of a silicate melt. This ratio affects the physical properties of the melts such as viscosity, thermal conductivity, etc.

3.2.2 The Modified Quasichemical Model (MQM)

The Modified Quasichemical Model (MQM), which takes into account the short-range-ordering of second-nearest-neighbor cations, has been used to describe the molten oxide. The model has been described in details by Pelton and Blander [8] and Pelton and Blander [9] and more recently by Pelton *et al.* [10] and Pelton and Chartrand [11].

The reaction depicting the formation of two 1-2 pair bonds from a 1-1 and a 2-2 pair in a binary system is shown below:

$$(1\text{-}1) + (2\text{-}2) = 2\,(1\text{-}2) \tag{3.15}$$

If the Gibbs energy change for the reaction is considered to be Δg_{12} and the coordination numbers of atoms (or molecules) 1 and 2 be Z_1 and Z_2 respectively, then the total number of bonds emanating from an ‘i’ atom, ion or molecule will be Z_iX_i. The mass balance equations can be written as:

$$Z_1X_1 = 2n_{11} + n_{12} \qquad \text{and} \qquad Z_2X_2 = 2n_{22} + n_{12} \tag{3.16}$$

where n_{ij} is the total number of bonds in one mole of the solution.

Three important quantities, namely pair fractions X_{ij}, overall mole (or site) fractions X_1 (or y_1) and coordination-equivalent fractions Y_1 have been defined in the equations 3.17, 3.18 and 3.19 respectively.

$$X_{ij} = \frac{n_{ij}}{n_{11} + n_{22} + n_{12}} \tag{3.17}$$

$$X_1 = 1 - X_2 = \frac{n_1}{n_1 + n_2} \tag{3.18}$$

$$Y_1 = 1 - Y_2 = \frac{Z_1 X_1}{(Z_1 X_1 + Z_2 X_2)} \tag{3.19}$$

where the total number of pairs in one mole of solution is $(Z_1X_1 + Z_2X_2)/2$. Equation 3.16 can now be rewritten in terms of pair fractions as follows:

$$Y_1 = X_{11} + X_{12} / 2 \qquad \textit{and} \qquad Y_2 = X_{22} + X_{12} / 2 \tag{3.20}$$

Hence, we may express the Gibbs energy of the solution as:

$$G = (n_1 g_1^o + n_1 g_2^o) - T\Delta S^{config} + (n_{12} / 2)\Delta g_{12} \tag{3.21}$$

where g_1^o and g_2^o are the molar Gibbs energies of the pure components, and ΔS^{config} is the configurational entropy of mixing considering random mixing of the (1-1), (2-2) and (1-2) pairs.

$$\begin{aligned}\Delta S^{config} = -R(n_1 lnX_1 + n_2 lnX_2) - R[n_{11} ln(X_{11} / Y_1^2) \\ + n_{22} ln(X_{22} / Y_2^2) + n_{12} ln(X_{12} / 2Y_1Y_2)]\end{aligned} \tag{3.22}$$

The equilibrium distribution can be calculated by minimizing G with respect to n_{12} at constant composition. This gives us a quasichemical equilibrium constant for the reaction (3.15) which may be written as:

$$\frac{X_{12}^2}{X_{11} X_{22}} = 4\exp(-\frac{\Delta g_{12}}{RT}) \tag{3.23}$$

When Δg_{12} = 0, the solution of the equations (3.19) and (3.20) gives a random distribution with $X_{11} = Y_1^2$, $X_{22} = Y_2^2$ and $X_{12} = 2Y_1Y_2$, and equation (3.22) reduces to ideal Raoultian entropy of mixing.

When Δg_{12} becomes very negative, 1-2 pairs predominate resulting in the plot of enthalpy versus composition to become V-shaped and plot of ΔS^{config} versus composition to become m-shaped with minima at $Y_1 = Y_2 = ½$.

When Δg_{12} becomes positive, (1-1) and (2-2) pairs dominate. Hence, the quasichemical model can also treat such clustering which involves positive deviation from ideality. In the modified quasichemical model, Δg_{12} is the model parameter which has to be optimized. The Δg_{12} parameter is usually expanded as a polynomial in terms of equivalent fractions.

3.2.3 Interpolation techniques

The binary model parameters of the liquid phase can be interpolated in order to estimate the properties of ternary and higher order liquid solution. This can be performed using various geometric models (Pelton and Chartrand [11]). The selection of the geometric model for the interpolation of the binary model parameters to ternary system can be made depending on the nature of each binary system bounding the ternary system.

Several geometric models may be proposed for ternary system. Fig. 3.3 illustrates some of the models that may be used.

Fig. 3.3 (a) and (b) show the Kohler and the Muggianu models respectively, which are symmetric models. Fig. 3.3(c) and (d) show the Kohler/Toop and Muggianu/Toop models respectively, which are asymmetric (component 1 is asymmetric). Gibbs energy of ternary or multicomponent solution can be expressed as:

$$G = \sum_i n_i g_i - T\Delta S^{config} + \sum_{i \neq j} \frac{n_{ij}}{2} \Delta g_{ij} \tag{3.24}$$

where $\Delta g_{ij} = \Delta g_{ij}^{o} + \sum_{ij} q_{ij}^{mn} Y_i^m Y_j^n$

Δg_{ij}^{o} and q_{ij}^{mn} are empirical binary coefficients, which may be functions of temperature and pressure and Y_i^m, Y_j^n are equivalent fractions. Depending on the interpolation technique, the interaction energy Δg_{ij} can be expressed differently:

(a). Symmetric Model:

Δg_{12} in the binary subsystem can be expressed as a polynomial in terms of the equivalent fractions as:

$$\Delta g_{12} = (\Delta g_{12}^{o} + \sum_{(i+j)\geq 1} q_{12}^{ij} (\frac{Y_1}{Y_1+Y_2})^i (\frac{Y_2}{Y_1+Y_2})^j) + \sum_{\substack{k\geq 1\\ i\geq 0\\ j\geq 0}} q_{12(3)}^{ijk} (\frac{Y_1}{Y_1+Y_2})^i (\frac{Y_2}{Y_1+Y_2})^j Y_3^k \tag{3.25}$$

The first term of the above equation is constant along line 3-a in Fig. 3.3 (a) and is equal to Δg_{12} in the 1-2 binary at point a. The second summation term consists of 'ternary terms' that are all zero in the 1-2 binary system and it depicts the effect of presence of component 3 on the Δg_{12} term. The empirical coefficients $q_{12(3)}^{ijk}$ are found by the optimization of ternary experimental data.

(b). Asymmetric Model:

Δg_{12} in the ternary solution can be expressed as:

$$\Delta g_{12} = (\Delta g_{12}^{o} + \sum_{(i+j)\geq 1} q_{12}^{ij} Y_1^{\,i} (1-Y_1)^j + \sum_{\substack{k\geq 1\\ i\geq 0\\ j\geq 0}} q_{12(3)}^{ijk}\, \mathrm{Y}_1^{\,i} (1-Y_1)^j (\frac{Y_3}{Y_2+Y_3})^k \tag{3.26}$$

The binary terms are constant along the line a-c and equal to their values at point a in Fig. 3.3 (c).

3.3 Monoxide solution

3.3.1 Crystal structure

The monoxide solid solution belongs to the space group $Fd\bar{3}m$. The monoxide solution is also known as the “halite (rock salt)” solution since its structure is same to that of NaCl (halite). A schematic structure of NaCl is shown in Fig. 3.4. The monoxide is generally of the type MO oxides where M is a divalent cation such as Mn^{2+}, Mg^{2+}, Fe^{2+}, Ca^{2+}, etc. Almost complete solid solubility can be observed across the entire range of compositions in most of the cases. Moreover, additional solubilities of N_2O_3 type of oxides can be observed (N is a trivalent cation such as Fe^{3+}, Cr^{3+}, Al^{3+}, etc.). The mixing occurs only on the cation sites for divalent metals when two MO oxides mix in the monoxide solution. However, it is not quite well understood how the dissolution of the N_2O_3 type of oxides take place.

3.3.2 Random mixing model

The Gibbs energy of the monoxide solution can be expressed as follows:

$$G = \sum_i y_i G_i^O - T\Delta S^{config} + G^E \tag{3.27}$$

$$where\ G^E = y_i^m y_j^n \sum_i \sum_j L_{ij}^{mn} \tag{3.28}$$

y_i, y_j denote the site fraction of cations ‘i’ and ‘j’ respectively in the first sublattice; G_i^O is the Gibbs energy of pure member; L_{ij} is the binary interaction parameter; m, n are the power terms of the interaction parameter.

3.4 Bixbyite solution

3.4.1 Crystal structure

Bixbyite is Mn_2O_3-rich solid solution. It has a cubic structure above room temperature and can dissolve certain amount of trivalent N_2O_3 type oxides (N is a trivalent cation such as Fe^{3+}, Cr^{3+}, Al^{3+}, etc.). Fig. 3.5 shows the schematic crystal structure of bixbyite. The bixbyite solid solution has $I\alpha\overline{3}$ symmetry. Mn and O ions are octahedrally and tetrahedrally coordinated, respectively. Mn and O ions fill 3/4 of the tetrahedral interstitials. The α-Mn_2O_3 transforms from cubic to orthorhombic structure with *Pbca* symmetry below 300K (Cockayne *et al.* [12]).

3.4.2 Random mixing model

The Gibbs energy of the bixbyite solid solution can be expressed in a way similar to that as shown in equation (3.27). The sublattice structure is

$$[Mn^{3+}, N^{3+}]_2 O_3 \tag{3.29}$$

where N^{3+} is a trivalent cation $Al^{3+}, Cr^{3+}, Fe^{3+}$,etc.

3.5 Corundum solution

3.5.1 Crystal structure

Corundum phase implies Al_2O_3-rich solid solutions which have trigonal structure where the O atoms are hexagonally coordinated as shown in Fig. 3.6 (a). Pauling and Hendricks [13] stated that each aluminium atom is surrounded by six oxygen atoms, which are not at the corners of a regular octahedron. Three of the O atoms were nearer to the metal atom than the other three indicating that location of electrons in the outer shells of an ion causes them to have different effective radii in different directions.

They also stated that each O atom was surrounded by four Al atoms, two of which are closer than the other two. Fig. 3.6 (b) shows the findings of Pauling and Hendricks [13]. Corundum crystallizes in the space group $R\overline{3}c$. It can also dissolve N_2O_3 type of oxides (N is a trivalent cation such as Fe^{3+}, Cr^{3+}, Mn^{3+}, etc.). The corundum solid solution can form complete solid solution between Al_2O_3, Cr_2O_3 and Fe_2O_3.

3.5.2 Random mixing model

The Gibbs energy of the corundum solution can be expressed in a way similar to that as shown in equation (3.27). The sublattice structure can be expressed as:

$$[Al^{3+}, M^{3+}]_2O_3 \tag{3.30}$$

where M^{3+} is a trivalent cation like $Mn^{3+}, Cr^{3+}, Fe^{3+}$,etc.

3.6 Liquid Fe solution

A thermodynamic model for the deoxidation equilibria was proposed by Jung *et al.* [14] and it was found to work very well in most of the systems. The parameters related to the Gibbs energy of formation of each associate during deoxidation reactions in steelmaking are stored in the FTmisc-FeLQ database [15]. All the calculations related to liquid iron solution in the present study were performed by using the FTmisc-FeLQ database [15].

References

[1] I.-H. Jung, "Critical evaluation and thermodynamic modeling of phase equilibria in multicomponent oxide systems," département de génie chimique, École Polytechnique de Montréal, Quebec, Canada, 2003.

[2] Sergei A. Degterov, Evgueni Jak, Peter C. Hayes, and Arthur D. Pelton, "Experimental Study of Phase Equilibria and Thermodynamic Optimization of the Fe-Zn-O System," *Metall. Mater. Trans. B,* **32B**, 643-657 (2001).

[3] M. Hillert, B. Jansson and B. Sundman, "*Application of the Compound-Energy Model to Oxide Systems*," Z. Metallkd., **79**, 81-87 (1988).

[4] O. Redlich and A.T. Kister, "Algebraic representation of thermodynamic properties and the classification of solutions," *Industrial and Engineering Chemistry,* **40[2]**, 345-348 (1948).

[5] A. D. Pelton and C. W. Bale, "Legendre polynomial expansions of thermodynamic properties of binary solutions," *Metall. Mater. Trans. A,* **17A**, 1057-1063 (1986).

[6] H. S. C. O'Neill and A. Navrotsky, "Cation distributions and thermodynamic properties of binary spinel solid solutions," *Am. Mineral.*, **69**, 733-753 (1984).

[7] B. E. Warren and J. Biscoe, "Fourier analysis of X-ray patterns of soda-silica glass," *J. Amer. Ceram. Soc.*, **21**, 259-265 (1938).

[8] A. D. Pelton and M. Blander, "Computer-assisted analysis of the thermodynamic properties and phase diagrams of slags," *Proc. 2nd Int. Symp. on Metallurgical Slags and Fluxes*, TMS-AIME, Warrendale, PA, 281-294 (1984).

[9] A. D. Pelton and M. Blander, "Thermodynamic analysis of ordered liquid solutions by a modified quasichemical approach - application to silicate slags," *Metall. Mater. Trans. B,* **17B**, 805-815 (1986).

[10] A. D. Pelton, S.A. Degterov, G. Eriksson, C. Robelin and Y. Dessureault "The modified quasichemical model I- binary solutions," *Metall. Mater. Trans. B,* **31B**, 651-660 (2000).

[11] A. D. Pelton and P. Chartrand, "The modified quasi-chemical model: part II-multicomponent solutions," *Metall. Mater. Trans. A*, **32A**, 1355-1360 (2001).

[12] E. Cockayne, I. Levin, H. Wu and A. Llobet, "The magnetic structure of bixbyite α-Mn_2O_3: a combined density functional theory DFT+U and neutron diffraction study," e-Print Archive, Condensed Matter, Pages1-11 [cond-mat.mtrl-sci]; Preprint 2012.

[13] L. Pauling and S. B. Hendricks, “The crystal structures of haematite and corundum,” *J. Am. Chem. Soc.*, **47 (3)**, 781–790, 1925.

[14] I.-H. Jung, S. A. Decterov and A. D. Pelton, “A Thermodynamic Model for Deoxidation Equilibria in Steel,” *Metall. Mater. Trans. B*, **35B**, 493-507 (2004).

[15] FactSage 6.3, www.factsage.com, Montreal, Canada, 2012.

[16] Patrice Chartrand and Arthur D. Pelton, “On the Choice of “Geometric” Thermodynamic Models,” *Journal of Phase Equilibria*, **21**, 141-147 (2000).

[17] T. Mathew, “Synthesis and characterization of mixed oxides containing cobalt, copper and iron and study of their catalytic activity,” Ph.D. thesis, University of Pune, India (2002).

[18] D. R. Askeland, P. P. Phulé, The Science and Engineering of Materials, (fourth ed.) Books/Cole-Thomson Learning, USA (2003).

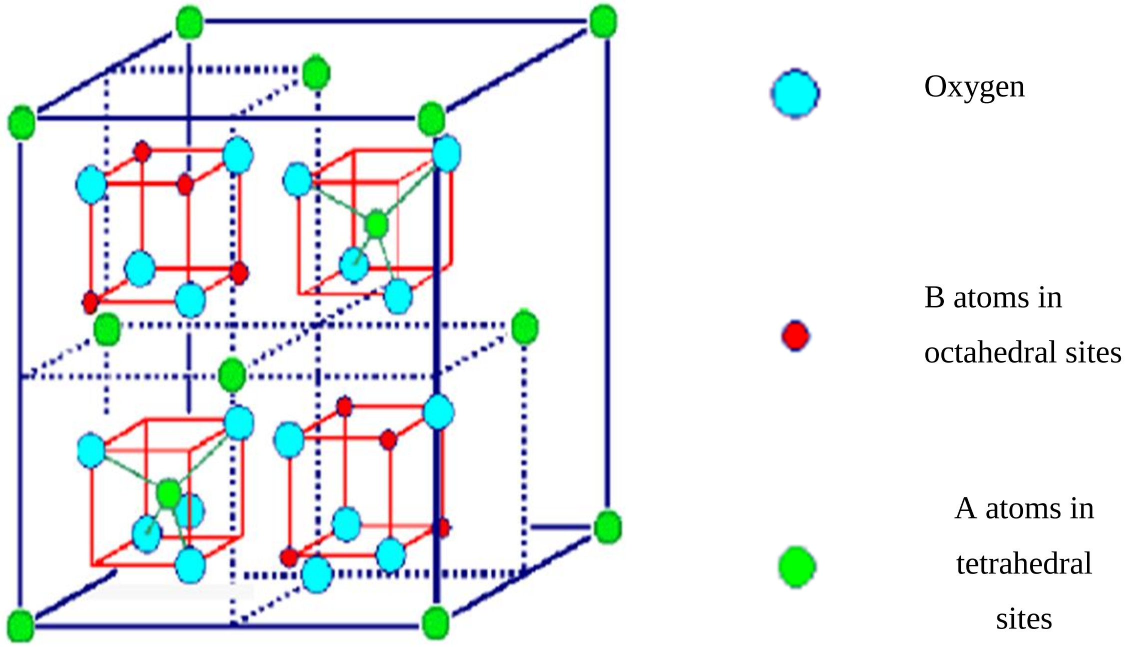

Figure 3.1: Structure of a unit cell of spinel AB_2O_4 (From Mathew [17]).

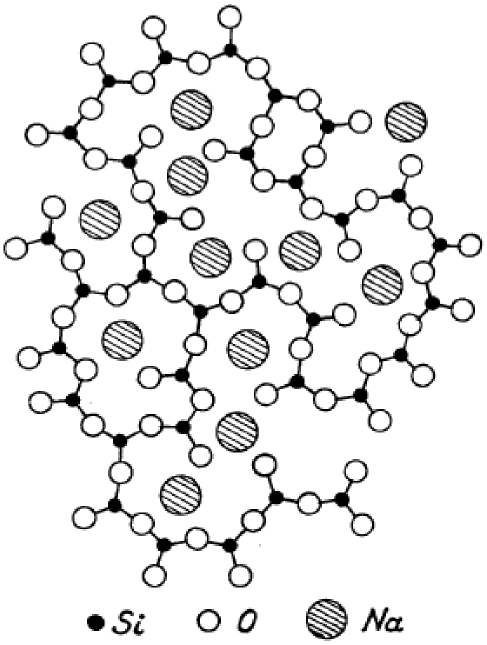

Figure 3.2: Structure of sodium silicate glass by Warren and Biscoe [7].

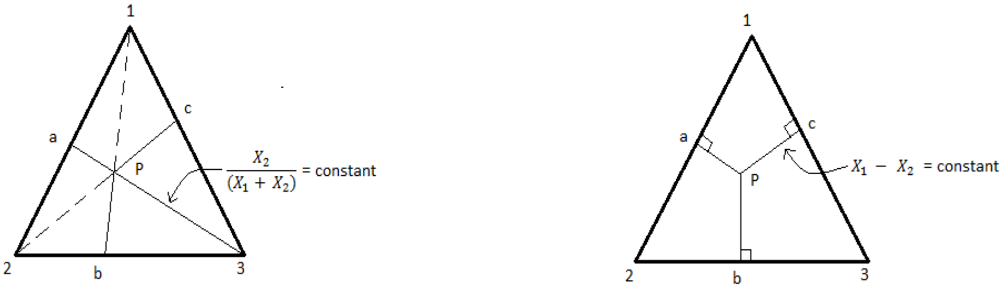

(a): Kohler Model

(b): Muggianu Model

(c): Kohler/Toop Model

(d): Muggianu/Toop Model

Figure 3.3: Geometric models used to estimate ternary thermodynamic data from optimized binary data (Chartrand and Pelton [16]).

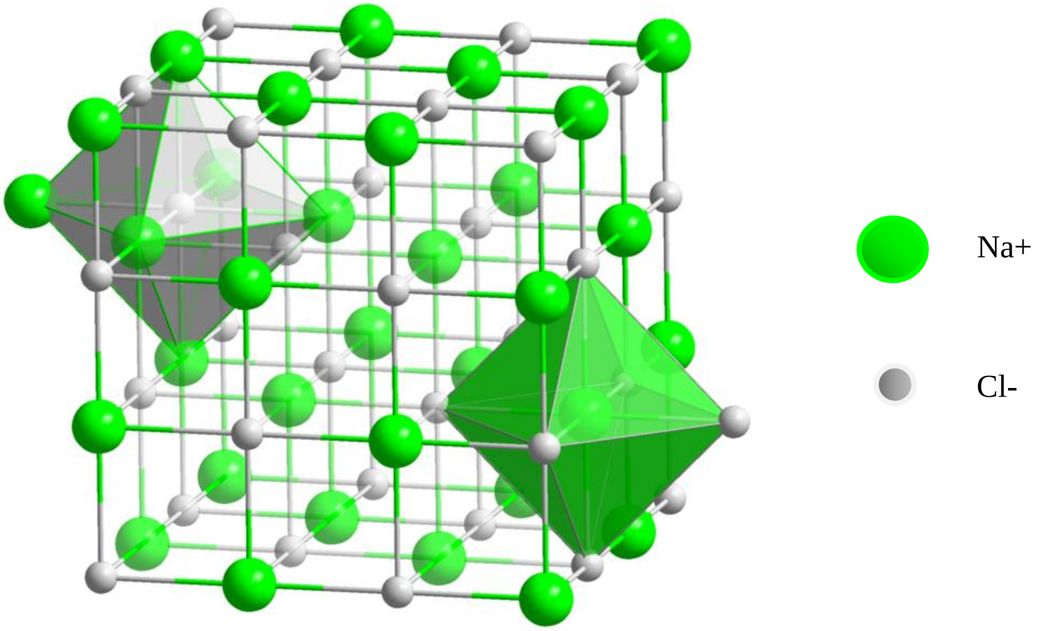

Figure 3.4: Crystal structure of a NaCl which is isostructural with monoxides.

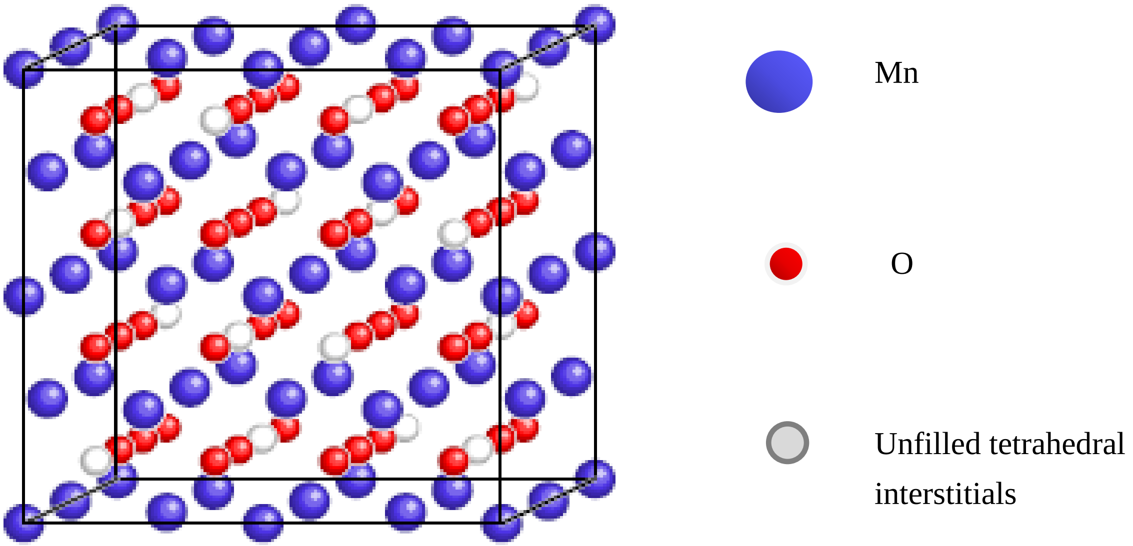

Figure 3.5: Crystal structure of bixbyite (Cockayne *et al.* [12]).

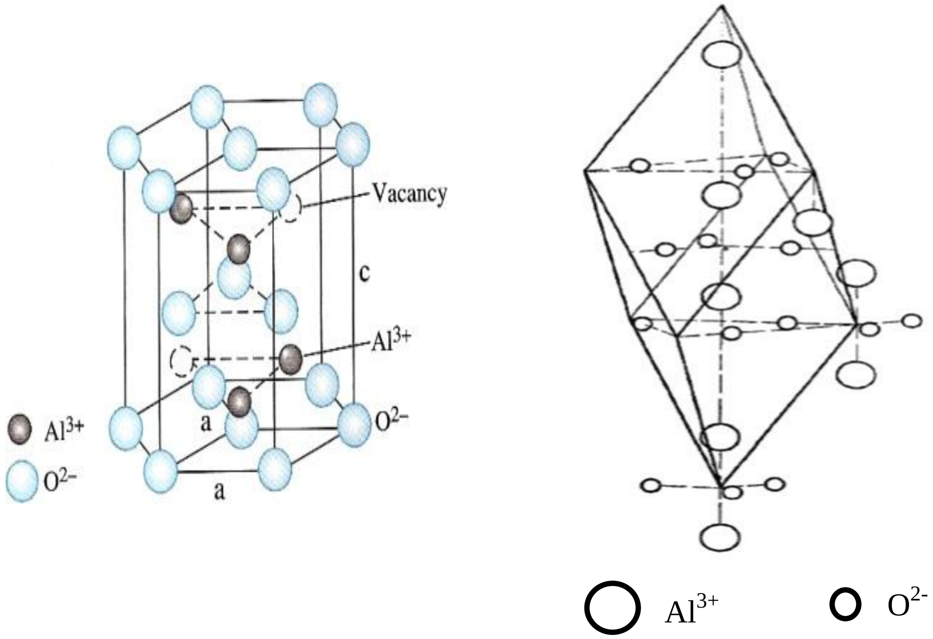

(a)

(b)

Figure 3.6: Crystal structures of corundum (α-Al_2O_3): (a) From Askeland and Phulé [18] and (b) From Pauling and Hendricks [13].

Chapter 4

Thermodynamic modeling of the MnO-Mn_2O_3-Al_2O_3 system

4.1 Introduction

The binary system have been studied by a number of researchers earlier (Hay *et al.* [1], Oelsen and Heynert [2], Ranganathan *et al.* [3], Novokhatskii *et al.*[4], Fischer and Bardenheuer [5], Dekker and Rieck [6], Jacob [7] and Golikov *et al.* [8]). Many researchers also tried to optimize the system previously (Eriksson *et al.* [9], Jung *et al.* [10], Farina and Neto [11] and Navarro *et al.* [12]). Profound experimental data on the Gibbs energy of formation of $MnAl_2O_4$ (the spinel present in the MnO-Al_2O_3 system) is available in the literature. However, the activity data of MnO is limited in the system. Hence, it is of utmost importance that we pay proper attention to the thermodynamic data of $MnAl_2O_4$ in order to achieve good results in optimization. Eriksson *et al.* [9] were able to reproduce the activities of MnO in the '$MnAl_2O_4$ and liquid' two phase region, but, they were unsuccessful in reproducing the activities of MnO in the 'Al_2O_3 and $MnAl_2O_4$' region. The optimized parameters by Eriksson *et al.* [9] when later used to calculate the phase diagrams and thermodynamic properties of the multicomponent systems containing the MnO-Al_2O_3 system gave erroneous results. Jung *et al.* [10] carried out the optimization of the MnO-Al_2O_3 system by considering the spinel solid solution $MnAl_2O_4$ as a line compound. Moreover, they considered only Mn^{2+} species in the slag. The optimized Gibbs energy of $MnAl_2O_4$ by Farina and Neto [11] was not in agreement with any of the experimentally determined values. They were also unable to reproduce the activities of MnO in the 'Al_2O_3 and $MnAl_2O_4$' region although they could calculate the congruent melting behaviour of $MnAl_2O_4$. Recently, Navarro *et al.* [12] modeled the slag phase in the MnO-Al_2O_3 system using the Kapoor-Frohberg-Gaye quasi-chemical model and they considered spinel solid solution $MnAl_2O_4$ as a stoichiometric compound.

In the present study, a complete thermodynamic description of the Mn-Al-O (MnO-Mn_2O_3-Al_2O_3) system has been carried out. The $MnAl_2O_4$ phase has been modeled as a spinel solution which has actual cation distribution using the two sublattice spinel model by Degterov *et al.* [13] in the framework of Compound Energy Formalism (Hillert *et al.* [14]). The slag phase has been modeled considering both the Mn^{2+} and Mn^{3+} species using the Modified Quasichemical Model (Pelton and Blander [15], Pelton and Blander [16], Pelton *et al.* [17], Pelton and Chartrand [18]). The main aim of the present study is to carry out a critical evaluation and thermodynamic optimization of all the properties and phase diagrams related to the $MnO-Al_2O_3$ system at pressures ranging from metal saturation to air in order to obtain Gibbs energies of all phases as functions of temperature and composition.

4.2 Phases and thermodynamic models

The calculated phase diagram of the (Mn-Al-O) $MnO-Mn_2O_3-Al_2O_3$ system at 1000°C and 1 bar total pressure is shown in Fig. 4.1. The following solution phases are found in the Mn-Al-O system:

Cubic spinel (encompassing cubic-Mn_3O_4, $MnAl_2O_4$ with limited solubility of Al_2O_3):
$(Mn^{2+}, Al^{3+})^T[Mn^{2+}, Mn^{3+}, Mn^{4+}, Al^{3+}, Va]_2^O O_4$
Tetragonal spinel (limited solution extended from tetragonal-Mn_3O_4):
$(Mn^{2+}, Mn^{3+}, Al^{3+})^T[Mn^{2+}, Mn^{3+}, Al^{3+}, Va]_2^O O_4$
Slag (molten oxide phase): $MnO-MnO_{1.5}-AlO_{1.5}$
Monoxide: MnO-rich solution containing small amount of $AlO_{1.5}$ and $MnO_{1.5}$
Bixbyite: Mn_2O_3-rich solution containing small amount of Al_2O_3
Corundum: Al_2O_3-rich solution containing small amount of Mn_2O_3
Alloy phases: liquid, bcc, fcc, sigma and so on

Cations shown within a set of brackets for spinels occupy the same sublattice. T and O represent the tetrahedral and octahedral cationic sites in spinel respectively. The magnetic properties of spinel and bixbyite were not seriously modeled in the present study because the critical temperatures are less than 100 K and its contributions to heat capacities were considered to the entropy of 298 K.

4.2.1. Spinel: Cubic and Tetragonal

There are two different cation sites in spinels: tetrahedral and octahedral sites. Thus, distribution of cations between these two sublattices is the most important physical and thermodynamic property of spinel. There are two types of spinel phases in the Mn-Al-O system: cubic and tetragonal spinels. Mn_3O_4 has tetragonal spinel structure and it transforms to cubic spinel over 1180°C in air. Although tetragonal Mn_3O_4 spinel can dissolve small amount of Al, cubic Mn_3O_4 spinel can extend up to Al_3O_4. Dorris and Mason [19] found that these two Mn_3O_4 spinels have different ionic configuration from their electrochemical seed-back experimental technique. In the case of cubic spinel, Mn^{2+} are on tetrahedral sites and Mn^{2+}, Mn^{3+} and Mn^{4+} are on octahedral sites: $(\mathrm{Mn}^{2+})^{\mathrm{T}}[\mathrm{Mn}^{2+},\mathrm{Mn}^{3+},\mathrm{Mn}^{4+}]_2^{\mathrm{O}}\mathrm{O}_4$. However, in the case of tetragonal spinel, both Mn^{2+} and Mn^{3+} cations can enter both tetrahedral and octahedral sites: $(\mathrm{Mn}^{2+},\mathrm{Mn}^{3+})^{\mathrm{T}}[\mathrm{Mn}^{2+},\mathrm{Mn}^{3+}]_2^{\mathrm{O}}\mathrm{O}_4$. When Mn_3O_4 spinel is mixed with $MnAl_2O_4$ spinel to form spinel solid solution, Al^{3+} can enter in both tetragonal and octahedral sites of the spinel. Vacancy could exist on octahedral sites for both cubic and tetragonal spinels. This structural information was properly implemented in the development of the present thermodynamic models for the cubic and tetragonal spinel phases in the Mn-Al-O system.

Both spinel models were developed within the framework of the Compound Energy Formalism (CEF) (Hillert *et al.* [14]). The Gibbs energy expression in the CEF per formula unit is:

$$G = \sum_i \sum_j Y_i^{\mathrm{T}} Y_j^{\mathrm{O}} G_{ij} - TS_{\mathrm{C}} + G^{\mathrm{E}} \tag{4.1}$$

where Y_i^{T} and Y_j^{O} represent the site fractions of constituents *i* and *j* on the tetrahedral and octahedral sublattices, G_{ij} is the Gibbs energy of an "end-member" $(i)^{\mathrm{T}}[j]_2^{\mathrm{O}}\mathrm{O}_4$ of the solution, in which the first sublattice is occupied only by cation *i* and the second only by cation *j*, G^{E} is the excess Gibbs energy, and S_{C} is the configurational entropy assuming random mixing on each sublattice:

$$S_{\mathrm{C}} = -R\left(\sum_i Y_i^{\mathrm{T}} \ln Y_i^{\mathrm{T}} + 2\sum_j Y_j^{\mathrm{O}} \ln Y_j^{\mathrm{O}}\right) \tag{4.2}$$

The excess Gibbs energy is expanded as:

$$\mathrm{G}^{\mathrm{E}}=\sum_i\sum_j\sum_k Y_i^{\mathrm{T}}Y_j^{\mathrm{T}}Y_k^{\mathrm{O}}L_{ij:k}+\sum_i\sum_j\sum_k Y_k^{\mathrm{T}}Y_i^{\mathrm{O}}Y_j^{\mathrm{O}}L_{k:ij} \tag{4.3}$$

where the parameters $L_{ij:k}$ are related to interactions between cations i and j on tetrahedral sites when all octahedral sites are occupied by k cations, and similarly the parameters $L_{k:ij}$ are related to interactions between i and j cations on octahedral sites when the tetrahedral sites are all occupied by k cations. One important assumption according to the model is that the interaction between the same two cations present on one sublattice will not change on changing the cation on the other sublattice, i.e.,

$$L_{k:ij}=L_{l:ij}=\ldots\ldots. \tag{4.4}$$

$$L_{ij:k}=L_{ij:l}=\ldots\ldots. \tag{4.5}$$

Redlich-Kister power series expansions given by Redlich and Kister [20] and Pelton and Bale [21] can be used to express the dependence of interaction energies on composition as follows:

$$L_{ij:k}=\sum_m {}^{m}L_{ij:k}(y_j^T-y_i^T)^m \tag{4.6}$$

$$L_{k:ij}=\sum_m {}^{m}L_{k:ij}(y_j^O-y_i^O)^m \tag{4.7}$$

The main model parameters are the end-member Gibbs energies, G_{ij}. Certain linear combinations of the G_{ij} parameters which have physical significance are used as the optimized model parameters. Degterov *et al.* [13] had already discussed the physical significance of these linear combinations (I and Δ). These linear combinations are related to the energies of classical site exchange reactions of cations. In this way, the model parameters could have certain physical meaning and it was found (Degterov *et al.* [13], Jung *et al.* [22], Jung *et al.* [23], Jung *et al.* [24], and Jung [25]) to be much easier to complete the thermodynamic modeling than individual setting of G_{ij} parameters without any reason. Moreover, high predictive ability of the model could be obtained. Details of the linear combinations of G_{ij} parameters for both cubic and tetragonal spinels are given in Table 1. Please note that notations F, J, K, L and V were used for Al^{3+}, Mn^{2+}, Mn^{3+}, Mn^{4+} and vacancy, respectively.

4.2.1.1. *Cubic spinel*

Cubic spinel has $(Mn^{2+}, Al^{3+})^T[Mn^{2+}, Mn^{3+}, Mn^{4+}, Al^{3+}, Va]_2^O O_4$ structure including vacancy (Va) on octahedral sites. The Gibbs energy diagram for the spinel is depicted in Fig. 4.2. Ten end-member Gibbs energies are required for the model. Among them, four Gibbs energies were already determined from the Mn-O system (Mn_3O_4) (Kang *et al.* [26]) and another two Gibbs energies (G_{FF} and G_{FV}) were determined from the previous study of the Mg-Al-O system (Jung *et al.* [27]). Four other Gibbs energies have been determined in the present study. It should be also noted that many end-members have charges other than neutral. The real spinel solution should have neutral charge. In the diagram of Fig. 4.2, the neutral charge lines are depicted as dotted lines.

In order to determine the Gibbs energy of end-members, physically meaningful combinations of G_{ij} have been considered. These are the model parameters optimized in the present study.

G_{JF}: Gibbs energy of completely normal $MnAl_2O_4$ spinel end-member (4.8)

2JF = FF + FJ: $\Delta G_{rxn} = I_{JF} = G_{FF} + G_{FJ} - 2G_{JF}$ (4.9)

FF + JK = FK + JF: $\Delta G_{rxn} = \Delta_{FJ:KF} = G_{FK} + G_{JF} - (G_{FF} + G_{JK})$ (4.10)

FF + JL = FL + JF: $\Delta G_{rxn} = \Delta_{FJ:LF} = G_{FL} + G_{JF} - (G_{FF} + G_{JL})$ (4.11)

For example, the reaction (4.9) is basically a site exchange reaction between the normal and the inverse spinel. Hence, the Gibbs energy of this reaction (I_{JF}) should be the one which affects the degree of inversion of the spinel the most. So, proper variation in this 'I' parameter has been performed in order to reproduce the experimental cation distribution data and Gibbs energy of formation of the spinel, after determination of G_{JF}. Similarly, Δ parameters of two other site exchange reactions ($\Delta_{\mathrm{FJ:KF}}$ and $\Delta_{\mathrm{FJ:LF}}$) have been optimized in such a way that they are able to correctly reproduce all other experimental phase diagram data. Excess Gibbs energy parameters have also been mainly optimized in order to reproduce the solubility of corundum in the spinel phase at high temperature along with the cation distribution data. All the optimized model parameters are listed in Table 4.1.

4.2.1.2. *Tetragonal spinel*

Tetragonal spinel has $(Mn^{2+}, Mn^{3+}, Al^{3+})^{T}[Mn^{2+}, Mn^{3+}, Al^{3+}, Va]_{2}^{O}O_{4}$ structure including vacancy (Va) on octahedral sites. Like cubic spinel, among twelve end-members Gibbs energies eight Gibbs energies had already been determined from the Mn-O (Kang *et al.* [26]) and Al-O (Jung *et al.* [27]) systems. Four other Gibbs energies have been determined in the present study. The model parameters are presented in Table 4.1. Due to the limited homogeneity region (small solubility of Al), the most important model parameter is Gibbs energy of tetragonal $MnAl_2O_4$ spinel ($(Mn^{2+})^{T}[Al^{3+}]_{2}^{O}O_{4}$) that is unstable in normal condition. This Gibbs energy has been determined to reproduce the solubility limit of Al in tetragonal spinel.

The G_{JF} (Gibbs energy of normal spinel, $(Mn^{2+})^{T}[Al^{3+}]_{2}^{O}O_{4}$) and one Δ (Δ_{JFK}) parameter have been optimized and all the remaining parameters are set to zero. The optimization of the parameters for the tetragonal spinel has been performed in a manner similar to the one done for the cubic spinel.

4.2.2. *Molten Oxide (slag)*

The Modified Quasichemical Model (Pelton and Blander [15], Pelton and Blander [16], Pelton et al. [17], Pelton and Chartrand [18]) which takes into account the short-range ordering of second-nearest-neighbor cations in the ionic melt, is used for modeling the slag.

The components of the slag are taken as MnO-$MnO_{1.5}$-$AlO_{1.5}$. Although Mn can have higher oxidation states, only the divalent and trivalent oxidation states which predominate at oxygen partial pressures less than 1.0 bar are considered in the present study. Mn_2O_3 and Al_2O_3 are taken as $MnO_{1.5}$ and $AlO_{1.5}$ to indicate that all Mn^{3+} and Al^{3+} cations are distributed independently between oxygen.

In the binary MnO-$AlO_{1.5}$ solution, for example short range ordering is taken into account by considering the second-nearest-neighbor pair exchange reaction:

$$(\text{Mn-Mn}) + (\text{Al-Al}) = 2\,(\text{Mn-Al}):\ \Delta g_{MnAl} \tag{4.12}$$

where (m-n) represents a second-nearest-neighbor pair. The Gibbs energy of the solution is given by

$$G = (n_{MnO} g^{O}_{MnO} + n_{AlO_{1.5}} g^{O}_{AlO_{1.5}}) - T\Delta S^{config} + n_{MnAl}(\Delta g_{MnAl}/2) \tag{4.13}$$

where n_i and g_i^O are the number of moles and molar Gibbs energies of the components, n_{MnAl} is the number of moles of (Mn-Al) bonds at equilibrium. ΔS^{config} is the configurational entropy of mixing expression for the random mixing of the bonds over 'bond sites' in the Ising approximation and is a function of n_{MnAl}. Δg_{MnAl} is the molar Gibbs energy change of reaction (4.12). It can be expanded as an empirical polynomial function in the mole fractions of the components. The coefficients of this polynomial are obtained by optimization of the available experimental data. The value of n_{MnAl} at equilibrium is obtained by setting $\partial G/\partial n_{MnAl} = 0$ at constant composition. This results effectively in a 'quasichemical equilibrium constant' for the reaction (4.12). The equilibrium shifts to the right or left as Δg_{MnAl} is negative or positive, respectively. For small Δg_{MnAl}, the model reduces in the limit to a random mixture of Mn^{2+} and Al^{3+} ions on cation sites, with the excess Gibbs energy expressed as a polynomial expansion in the component mole fractions.

All second-nearest-neighbor "coordination numbers" used in the present model for the slag are the same as in previous studies (Kang *et al.* [26]). The binary sub-system MnO-$MnO_{1.5}$ (Kang *et al.* [26]) has been already critically evaluated and optimized, and these optimized model parameters are used in the present study without any modification. Optimized binary parameters for the MnO-$AlO_{1.5}$ and $MnO_{1.5}$ -$AlO_{1.5}$ slag solutions have been obtained in the present study as described in the following sections. These are listed in Table 4.1. The Gibbs energy of the ternary liquid solution has been estimated using the symmetric “Kohler-like” (Pelton [28]) interpolation technique. No ternary model parameter has been used in the present study.

4.2.3. MnO (monoxide)

Monoxide solution has rock-salt structure. It is modeled as a simple random mixture of Mn^{2+}, Mn^{3+} and Al^{3+} ions on cation sites. It is assumed that cation vacancies remain associated with Mn^{3+} or Al^{3+} ions and so do not contribute to the configurational entropy. Binary excess Gibbs energies were modeled by simple polynomial expansions in the mole fraction (Pelton [28]). The properties of the ternary monoxide solution were calculated from the binary parameters of the MnO-$AlO_{1.5}$ (Eriksson *et al.* [9]) and MnO-$MnO_{1.5}$ (Kang *et al.* [26]) solutions with the symmetric “Kohler-like” approximation (Pelton [28]). The Gibbs energy per mole of the solution is expressed as follows:

$$G_m = \sum_i X_i G_i^o + RT\sum_i X_i \ln X_i + \sum_i \sum_j X_i X_j \left(\frac{X_i}{X_i + X_j} \right)^m \left(\frac{X_j}{X_i + X_j} \right)^n q_{ij}^{mn} + g_{ternary}^{ex} \qquad (4.14)$$

where G_i^o is the Gibbs energy of component like MnO, $MnO_{1.5}$ and $AlO_{1.5}$, and X_i is mole fractions of component. The binary model parameters q_{ij}^{mn} of MnO-$AlO_{1.5}$ (Eriksson *et al.* [9]) and MnO-$MnO_{1.5}$ (Kang *et al.* [26]) were optimized previously. There is no binary parameter for the $MnO_{1.5}$-$AlO_{1.5}$ system and no ternary excess parameter $g_{ternary}^{ex}$ has used in the present study.

4.2.4. Mn_2O_3 (bixbyite) and Al_2O_3 (corundum)

Bixbyite phase is Mn_2O_3-rich solid solution which has a cubic structure above room temperature and dissolves certain amount of Al oxide (Al_2O_3). On the other hand, corundum phase is Al_2O_3 rich solid solution which has trigonal structure based on the hcp oxygen-packing scheme. Small amount of Mn oxide (Mn_2O_3) can be dissolved into corundum phase. The Gibbs energy per mole of the each binary solution is expressed as:

$$G_m = (X_A G_A^o + X_B G_B^o) + 2RT(X_A lnX_A + X_B lnX_B) + \sum q_{AB}^{mn} (X_A)^m (X_B)^n \qquad (4.15)$$

where G_i^o is the Gibbs energy of components like Mn_2O_3 and Al_2O_3, and X_i is mole fraction of the component. The binary model parameters q_{ij}^{mn} for the bixbyite phase have been optimized in the present study. The binary model parameters q_{ij}^{mn} for the corundum phase were optimized previously (Eriksson *et al.* [9]). The optimized model parameters for the corundum phase have been used in the present study without any modification. All the optimized model parameters are listed in Table 4.1.

4.2.5. Metallic phases

In this study, FSStel database [29] is used for Al-Mn metallic system. There are many intermetallic phases. The thermodynamic properties of all phases were optimized previously (Jansson [30]) based on phase diagrams, activities, heat of mixing, etc. This is used for the calculations of phase equilibria at metallic saturation.

4.3 Critical evaluation and optimization

4.3.1 Thermodynamic properties of $MnAl_2O_4$ spinel solution

4.3.1.1 Heat capacity of $MnAl_2O_4$

Fig. 4.3 shows the calculated heat capacity of $MnAl_2O_4$ from the present spinel model in comparison with experimental data by Navarro *et al.* [12]. It should be noted that the calculated curve is not obtained from theoretical end-member spinel model but the real $MnAl_2O_4$ spinel solution which has cation distribution. Navarro *et al.* [12] recently measured the heat capacity (C_p) of stoichiometric $MnAl_2O_4$ spinel using thermal relaxation calorimetry at the temperatures from 2 to 300K. The experimental data are the average value of 3 independent C_p measurements at each temperature. They calculated the molar entropy of $MnAl_2O_4$ spinel at 298.15K ($S^0_{298.15}$)

to be 116 ± 5 J/mol-K by integrating the low temperature C_p data. High temperature ($323 < T < 873K$) Cp measurements were done with the help of a differential scanning calorimeter. First of all, the $MnAl_2O_4$ samples were heated from 373K to 873K at constant rate of 20 K/min. Then they were cooled from 873K to 323K at constant rate of 20 K/min with isothermal stages at systematically separated temperatures. Each isothermal temperature was maintained for two minutes, enough to reach a constant heat flux. A polynomial function of temperature was used to fit the measured isothermal flux. The heat capacity of $MnAl_2O_4$ was then calculated based on the knowledge of few properties of standard (Al_2O_3) and the crucible (Al).

Experimental C_p in fig 4.3 is in fact the C_p of $(Mn^{2+}, Al^{3+})^T[Mn^{2+}, Al^{3+}]_2^O O_4$ spinel at stoichiometric $MnAl_2O_4$ composition. This means that the cation distribution may change with change in temperature. However, the cation distribution data of $MnAl_2O_4$ spinel show highly normal distribution (inversion is less than 0.05 at 500K), the heat capacity should be close to the experimental heat capacity of $(Mn^{2+})^T[Al^{3+}]_2^O O_4$ end-member. In the present study, the heat capacity of $(Mn^{2+})^T[Al^{3+}]_2^O O_4$ was determined from this experimental data. However, the calculated line in Fig. 4.3 is obtained after considering cation distribution of real stoichiometric spinel, which will be discussed below. The calculated heat capacity curve is in very good agreement with the experimental Cp data. Our calculations give a value of 115.32 J/mol-K for the $S^0_{298.15}$ which is nearly equal to the experimental value of 116 ± 5 J/mol-K.

4.3.1.2 Gibbs energy of $MnAl_2O_4$

Many researchers carried out independent measurements of the Gibbs energy of formation of $MnAl_2O_4$ from MnO and Al_2O_3 as shown in Fig. 4.4. Lenev and Novokhatskii [31] were the first to carry out the investigation on the Gibbs energy of formation of the $MnAl_2O_4$ spinel by employing the reduction reaction of $MnAl_2O_4$ with hydrogen gas. From $MnAl_2O_4$ + Mn + O_2 + Al_2O_3 equilibration with known partial pressure of O_2, they could evaluate the Gibbs energy of formation of $MnAl_2O_4$ from MnO and Al_2O_3 at the temperature range from 1550 to 1700°C. Kim and McLean [32] equilibrated liquid Fe and Al_2O_3 with additions of $FeAl_2O_4$-$MnAl_2O_4$ spinel solid solutions at 1550, 1600 and 1650°C. From the known activities of Mn and O in liquid Fe, the Gibbs energy of $MnAl_2O_4$ was calculated. Jacob [7] and Zhao *et al.* [33] also performed similar experiment where $MnAl_2O_4$ and Al_2O_3 were equilibrated with Pt-Mn and Ag-Mn alloys under fixed partial pressure of oxygen, respectively. From the known activity of Mn in the alloys and the analyzed Mn concentration, the Gibbs energy of $MnAl_2O_4$ was calculated. Timucin and Muan [34] equilibrated NiO-MnO/$NiAl_2O_4$-$MnAl_2O_4$/Ni under fixed partial pressure of oxygen at 1300 and 1400°C. After the equilibration experiment, they were able to calculate the Gibbs energy of formation of the spinel $MnAl_2O_4$ from MnO and Al_2O_3 using a ternary Gibbs-Duhem integration technique. Dimitrov *et al.* [35] equilibrated liquid Fe with Al_2O_3 and $MnAl_2O_4$ and used a solid electrolyte to measure the partial pressure of oxygen. They calculated the Gibbs energy of $MnAl_2O_4$ from measurements of partial pressure of oxygen from emf and calculated activities of Mn in liquid Fe.

As can be seen in Fig. 4.4, the optimized Gibbs energy of $MnAl_2O_4$ spinel solid solution is in good agreement with experimental data within the experimental error ranges. It should be noted that the previous thermodynamic modeling result regarding Gibbs energy of $MnAl_2O_4$ by Navarro *et al.* [12] is far away from the experimental data. In addition, the compiled data from Barin [36] are much more negative than the experimental data. It should be noted that the Gibbs energy of $MgAl_2O_4$ from MgO and Al_2O_3 is also about – 40 kJ/mol at 1600°C (Jung *et al.* [27]) which is similar to the Gibbs energy of $MnAl_2O_4$ in Fig. 4.4.

4.3.1.3 Cation distribution of $MnAl_2O_4$ spinel solution

$MnAl_2O_4$ is considered as a normal spinel (Greenwald et al. [37], Roth [38], Murthy *et al.* [39], Essene and Peacor [40], Lucchesi [41], Tristan *et al.* [42], Halenius [43], Halenius [44]) at low temperature (that is, Mn^{2+} and Al^{3+} cations occupy the tetrahedral and octahedral sites respectively). However, there is a certain degree of disorderliness of cations between the sites, and this degree of inversion also increases with increasing temperatures. Fig. 4.5 shows the variation of cation distribution in $MnAl_2O_4$ as a function of temperature.

Greenwald et al. [37] prepared the spinel sample and annealed at 1400°C for 1 or 2 hours followed by quenching to room temperature. The cation distribution of the quenched samples was determined using XRD technique to be 0.29±0.04. Roth [38] prepared $MnAl_2O_4$ samples under controlled partial pressure of oxygen, annealed them and the structural analysis was performed using neutron diffraction technique. They obtained a value of 0.084±0.044 for the degree of inversion of the samples. Tristan *et al.* [42] carried out similar experiment using XRD with Rietveld analysis and obtained a value of 0.06 for the degree of inversion. Tristan *et al.* [42] obtained a value which is lower than that obtained by Roth [38] probably because of lower sample preparation temperature as compared to that of Roth [38]. Roth [38] stated that cation diffusion below 600°C is negligible. Tristan *et al.* [42] believed that only at temperatures greater than 500°C mixing of cations from different sites can occur. Jung *et al.* [27] considered the T_{froz} of $MgAl_2O_4$ spinel to be 700°C. Since no specific temperature was mentioned in the studies of Roth [38] and Tristan *et al.* [42], the T_{froz} (i.e. the temperature below which there is no inversion due to slow kinetics) was chosen as 700°C in the case of $MnAl_2O_4$ based on logical reasoning and critical evaluation of literature data. Recently, Halenius [44] determined the cation distribution of $MnAl_2O_4$ sample quenched from 900°C using single crystal structural refinement technique. They obtained a value of 0.16 for the degree of inversion of the spinel at 900°C.

As can be seen in Fig 4.5, the variation of cation distribution of $MnAl_2O_4$ with temperature can be well reproduced by the present spinel model.

4.3.1.4 Activity of MnO in the MnO-Al_2O_3 system

Sharma and Richardson [45] and Jacob [7] equilibrated the MnO-Al_2O_3 mixtures with Pt-Mn foils under fixed partial pressures of oxygen at 1600 and 1650°C. Then, the activity of MnO in MnO-Al_2O_3 mixture was calculated from the known activity of Mn and controlled oxygen partial pressure. The experimental data are plotted in Fig. 4.6.

The optimization of the activity of MnO in the MnO-Al_2O_3 system is compared with experimental data in Fig. 4.6. The present results are very similar to those of previous optimization by Jung *et al.* [10]. It should be noted that the activity of MnO in two phase region of 'Al_2O_3+$MnAl_2O_4$' is directly related to the Gibbs energy of $MnAl_2O_4$ shown in Fig. 4.4. The experimental activities of MnO on the MnO-rich side are well reproduced in the present study.

4.3.2 Phase diagram of the $MnO-Mn_2O_3-Al_2O_3$ system

4.3.2.1 Under reducing atmosphere: $MnO-Al_2O_3$

Fig. 4.7 shows the calculated phase diagram of the Mn-Al-O system at reduced oxygen partial pressures along with the experimental data.

Hay *et al.* [1] employed heating and cooling curve measurement to determine the phase diagram at MnO-rich (wt.% $Al_2O_3 \leq 50\%$) region. They reported the liquidus of spinel (they claimed it was $MnAl_2O_4$) and MnO and also the eutectic reaction at MnO-rich region. They also proposed peritectic melting of spinel at 1560°C. Unfortunately, the gas atmosphere at the experiment was not tightly controlled and it seems that the oxygen partial pressure was not sufficiently low. Later, Oelsen and Heynert [2] reported the phase diagram of $MnO-Al_2O_3$ system at reduced condition from the extrapolation of the liquidus of the $FeO-MnO-Al_2O_3$ system saturated with liquid Fe. The samples contained in Al_2O_3 crucible were quenched after equilibration to determine the phase. They reported eutectic and peritectic temperatures of 1520°C at MnO-rich region and 1720°C at Al_2O_3-rich region, respectively, measured by a calorimetric technique. However, no experimental details are given. Fischer and Bardenheuer [5] also employed similar technique and reported the eutectic reaction at MnO-rich region to occur at about 70 wt. % MnO and 1580 ± 5°C. Novokhatskii *et al.* [4] investigated the melting points of $MnAl_2O_4$ spinel phase using visual observation under controlled oxygen partial pressure using a gas mixture of Ar and H_2. They reported the congruent melting of $MnAl_2O_4$ spinel at 1850°C and eutectic reactions of MnO-rich side at 1520 ± 10°C and of Al_2O_3-rich side at 1770± 15°C. Novokhatskii *et al.* [4] claimed, from XRD results, that Al_2O_3 and $MnAl_2O_4$ exhibit virtually no mutual solid solubility.

Jacob [7] measured the liquidus temperatures shown in Fig. 4.7 at 1600^oC and 1650^oC by equilibration under controlled oxygen pressures of 10^{-5} to 10^{-6} bar, followed by quenching and electron microprobe analysis. These same experiments showed approximately 1 % solubility of Al_2O_3 in solid MnO and no solubility of MnO in $MnAl_2O_4$. In similar experiments, Jacob heated Mn and MnO in sealed Al_2O_3 crucibles at 1600°C and 1650°C, followed by quenching and electron microprobe analysis (EPMA). A solubility of MnO in Al_2O_3 of approximately 1 % and a solubility of Al_2O_3 in $MnAl_2O_4$ of approximately 3 % were observed. The invariant temperatures and the melting points of pure MnO, Al_2O_3 and $MnAl_2O_4$ were measured by Jacob [7] by examination, either visual or under an optical microscope, of pellets quenched from high temperature under purified Ar. He reported that $MnAl_2O_4$ melts congruently at 1850°C and hence that the invariant shown at 1769°C in Fig. 4.7 is actually a eutectic.

The calculated phase diagram of MnO-Al_2O_3 system at oxygen pressures of 10^{-5} to 10^{-6} atm are presented in Fig. 4.7. Fig 4.7 shows a predicted phase diagram at 10^{-8} atm. At the reducing conditions, the amount of Mn^{3+} in liquid phase is negligible. The maximum amount of Mn_2O_3 in the slag at 1600°C is around 2.7 wt%. Therefore, Gibbs energy of liquid phase is mainly determined by the interaction between MnO and Al_2O_3. That is, in the present modeling, the MQM parameters for liquid MnO-Al_2O_3 solution was determined to reproduce the phase diagram in Fig. 4.7, after the Gibbs energy of $MnAl_2O_4$ spinel phase was determined as shown in Fig. 4.4. The experimental liquidus reported by Jacob [7], which is considered to be the most reliable one out of all the experimental results, is well reproduced except the congruent melting of $MnAl_2O_4$ spinel. The same difficulty was found in the previous optimization by Jung *et al.* [10]. As it was mentioned in the previous work by Jung *et al.* [10], in order to reproduce the phase diagram accurately with congruent melting, the Gibbs energy of $MnAl_2O_4$ spinel in Fig. 4.4 should be much more negative. As pointed out by Jung *et al.* [10], more negative Gibbs energy of $MnAl_2O_4$ induces more negative interaction of MnO and Al_2O_3 in liquid phase, which causes the poor description of activity of MnO in MnO-Al_2O_3-CaO-SiO_2 system. The optimized MQM parameters for liquid MnO-Al_2O_3 are listed in Table 1.

The newly optimized phase diagram in MnO-rich region is almost the same as the one optimized previously Jung *et al.* [10]. It should be noted that $MnAl_2O_4$ was considered as stoichiometric phase in the previous study by Jung *et al.* [10]. In the present modeling, the spinel solution between Mn_3O_4 and $MnAl_2O_4$ with excess solubility of Al_2O_3 was considered. As can be seen in Fig. 4.7, the wide spinel solution at sub-solidus temperature is predicted nearly from Mn_3O_4 (MnO side) at the oxygen partial pressures of 10^{-5} to 10^{-6} bar. The amount of excess Al_2O_3 solubility in $MnAl_2O_4$ at Al_2O_3-rich side is a bit larger than the experimental data by Jacob. In the modeling, however, it is found that this solubility is highly related to the excess solubility of Al_2O_3 in oxidizing condition shown in Fig. 4.8.

4.3.2.2. Under oxidizing atmosphere: Mn_2O_3-Al_2O_3 system

Fig. 4.8 shows the calculated phase diagram of the Mn-Al-O system in air from the present optimization along with the experimental data.

Ranganathan *et al.* [3] were the first to determine the phase relations in the Mn_2O_3-Al_2O_3 system in air using the classical quenching technique followed by optical microscopy and XRD phase determination. They prepared the samples of entire composition and equilibrated them at the temperature range between 800 and 1700°C. The main feature of the phase diagram in air was determined by Ranganathan *et al.* [3]. Dekker and Rieck [6] used the similar technique to determine the sub-solidus phase equilibria. Bobov *et al.* [46] prepared the sample at Mn_3O_4 rich region at temperature range from 800 to 1000°C to determine the phase boundary of tetragonal spinel more accurately. Golikov *et al.* [8] also concentrated their investigation at the temperature between 900 and 1300°C to determine the phase boundary of tetragonal spinel and cubic spinel using quenching technique and in-situ high temperature radiography technique.

Due to the presence of a Jahn-Teller effect in spinel structure with Mn^{3+} ion, the quenched cubic spinel phase is tetragonally distorted and is easily misinterpreted as tetragonal spinel. In the present study, the tetragonally distorted cubic spinel due to Jahn-Teller effect is treated as second order transformation of cubic spinel, which is different from first order transformation to tetragonal spinel. For example, Ranganathan *et al.* [3] using the quenching technique reported that Mn_3O_4-rich region ($Mn/(Mn+Al) > 0.4$) at about 1000°C was occupied by tetragonal Mn_3O_4 spinel (Hausmannite). This region was more carefully studied by Dekker and Rieck [6], Bobov *et al.* [46] and Golikov *et al.* [8] to clearly distinguish the boundary of tetragonal spinel and cubic spinel as can be seen in Fig. 4.8(b).

The present modeling for the spinel solution can successfully reproduce the experimental phase diagram data as can be seen in Fig. 4.8. As discussed above, the phase boundary of two spinels regions (tetragonal + cubic spinels) was determined mostly based on the studies of Dekker and Rieck [6], Bobov *et al.* [46] and Golikov *et al.* [8], while other areas are determined mostly based on the experimental data of Ranganathan *et al.* [3]. As mentioned in the previous section, the excess solubility of Al_2O_3 in $MnAl_2O_4$ spinel in reducing condition in Fig. 4.7 is related to the limit of homogeneity range of cubic spinel phase toward Al-rich side at about 1700°C (up to Al/(Mn+Al) = 0.75) in Fig. 4.8. That is, in order to reproduce the extent of the homogeneity range of cubic spinel towards Al_2O_3 side in air, the noticeable amount of excess solubility of Al_2O_3 in $MnAl_2O_4$ is also expected in reducing condition. The homogeneity range of tetragonal spinel was mainly determined by the end-member Gibbs energy of tetragonal $(Mn^{2+})^T[Al^{3+}]_2^O O_4$. The homogeneity range of bixbyite was also reproduced by excess interaction parameter. The MQM parameter for Mn_2O_3-Al_2O_3 binary system was determined to reproduce the liquidus and solidus of Mn-Al-O system in air. All the optimized model parameters are summarized in Table 1.

4.3.2.2. Predictions in the Mn-Al-O system

Based on the optimized model parameters, the experimentally unexplored phase diagrams can be predicted. For example, the oxygen partial pressure – composition diagrams for the Mn-Al-O system at various temperatures (1000 - 1600°C) are calculated in Fig. 4.9 with the help of newly optimized database and the FSStel [29] database.

4.4 Summary

All the thermodynamic and phase diagram data in the Mn-Al-O system from reducing condition to oxidizing condition were collected and critically evaluated for the thermodynamic optimization of the system. Compared with previous optimizations, the present optimization properly takes into account of the cubic and tetragonal spinel solution phases (Mn_3O_4-$MnAl_2O_4$ with excess Al_2O_3) for the first time. All the cation distribution data and thermodynamic data of the spinel and phase diagram related to the spinel solution were well reproduced. The optimized model parameters can reproduce all the reliable experimental data of the Mn-Al-O system at any oxygen partial pressure from room temperature to above liquidus temperature. The optimized database has been also used to predict the experimentally unexplored phase diagrams of the Mn-Al-O system.

References

[1] R. Hay, J. White and A. B. MacIntosh, “Slag systems,” *J. West Scot. Iron and Steel Inst.*, **42[6]**, 99-104 (1935).

[2] W. Oelsen and G. Heynert, “The reactions between iron-manganese melts and the melts of their aluminates,” *Arch. Eisenhuttenwes.*, **26**, 567-575 (1955)

[3] T. Ranganathan, B. E. Mackean, and A. Muan, “The system manganese oxide-alumina in air,” *J. Am. Ceram. Soc.*, **45**, 279-281 (1962).

[4] I. A. Novokhatskii, L. M. Lenev, A. A. Savinskaya and A. V. Gorokh, “Diagram of phase equilibrium in MnO-Al2O3 (corundum) system,” *Zh. Neorg. Khim.*, **11 [2]**, 427-428 (1966).

[5] W. A. Fischer and P. W. Bardenheuer, “Equilibria between manganese, aluminium and oxygen-containing iron melts and their slags in a manganese oxide crucible at 1530 to 1700°C,” *Arch. Eisenhuttenwes.*, **39[9]**, 637-643 (1968).

[6] E. H. L. J. Dekker and G. D. Rieck, “Revised phase diagram and X-ray data of the Mn_3O_4-Al_2O_3 system in air,” *Z. Anorg. Allg. Chem.*, **415**, 69-80 (1975).

[7] K. T. Jacob, “Revision of thermodynamic data on MnO-Al_2O_3 melts,” *Can. Metall. Quater.*, **20[1]**, 89-92 (1981).

[8] Y. V. Golikov, S. A. Petrova, A. V. Antonov and V. F. Balakirev, “Phase diagrams of the Mn-Al-O system,” *J. Phys. Chem. Solids*, **56[5]**, 767-775 (1995).

[9] G. Eriksson, P. Wu and A.D. Pelton, “Critical evaluation and optimization of the thermodynamic properties and phase diagrams of the MgO-Al_2O_3, MnO-Al_2O_3, FeO-Al_2O_3, Na_2O-Al_2O_3, and K_2O-Al_2O_3 systems,” *CALPHAD: Computer Coupling of Phase Diagrams and Thermochemistry*, **17[2]**, 189-205 (1993).

[10] I.-H Jung, Y.-B Kang, S.A. Decterov, and A.D. Pelton “Thermodynamic evaluation and optimization of the MnO-Al_2O_3 and MnO-Al_2O_3-SiO_2 systems and applications to inclusion engineering,” *Metall. Mater. Trans. B*, **35B**, 259-268 (2004).

[11] A. B. Farina and F. B. Neto, “Thermodynamic modelling of an Al_2O_3-MnO system using the ionic model,” *CALPHAD: Computer Coupling of Phase Diagrams and Thermochemistry*, **33**, 711-718 (2009).

[12] R. C. S. Navarro, A. M. S. Gomez, R. R. de Avillez, “Heat Capacity of stoichiometric Al_2MnO_4 spinel between 2 and 873K,” *CALPHAD: Computer Coupling of Phase Diagrams and Thermochemistry*, **37**, 11-17 (2012).

[13] S. A. Degterov, E. Jak, P. C. Hayes, and A. D. Pelton, “Experimental Study of Phase Equilibria and Thermodynamic Optimization of the Fe-Zn-O System,” *Metall. Mater. Trans. B,* **32B**, 643-657 (2001).

[14] M. Hillert, B. Jansson and B. Sundman, “Application of the Compound-Energy Model to Oxide Systems,” *Z. Metallkd.*, **79**, 81-87 (1988).

[15] A. D. Pelton and M. Blander, “Computer-assisted analysis of the thermodynamic properties and phase diagrams of slags,” *Proc. of 2nd Int. Symp. on Metallurgical Slags and Fluxes*, TMS-AIME, Warrendale, PA, 281-294 (1984).

[16] A. D. Pelton and M. Blander, “Thermodynamic analysis of ordered liquid solutions by a modified quasi-chemical approach - application to silicate slags,” *Metall. Mater. Trans. B*, **17B**, 805-815 (1986).

[17] A. D. Pelton, S.A. Degterov, G. Eriksson, C. Robelin and Y. Dessureault “The Modified Quasichemical Model I-Binary Solutions,” *Metall. Mater. Trans. B,* **31B**, 651-660 (2000).

[18] A. D. Pelton and P. Chartrand, “The modified quasi-chemical model: part II. multicomponent solutions,” *Metall. Mater. Trans. A*, **32A**, 1355-1360 (2001).

[19] S. E. Dorris and T. O. Mason, “Electrical properties and cation valencies in Mn_3O_4,” *J. Am. Ceram. Soc.*, **71[5]**, 379-385 (1988).

[20] O. Redlich and A.T. Kister, “Algebraic representation of thermodynamic properties and the classification of solutions,” *Industrial and Engineering Chemistry,* **40[2]**, 345-348 (1948).

[21] A. D. Pelton and C. W. Bale, “Legendre polynomial expansions of thermodynamic properties of binary solutions,” *Metall. Mater. Trans. A*, **17A**, 1057-1063 (1986).

[22] I.-H Jung, S. A. Decterov and A. D. Pelton “Thermodynamic evaluation and modeling of the Fe-Co-O system,” *Acta Mater.*, **52**, 507-519 (2004).

[23] I.-H Jung, S. A. Decterov and A. D. Pelton “Critical thermodynamic evaluation and optimization of the Fe-Mg-O system,” *J. Phys. Chem. Solids*, **65**, 1683-1695 (2004).

[24] I.-H Jung, S. A. Decterov, and A. D. Pelton “Thermodynamic modeling of the MgO-Al_2O_3-CrO-Cr_2O_3 system,” *J. Am. Ceram. Soc.*, **88[7]**, 1921-1928 (2005).

[25] I.-H Jung "Critical evaluation and thermodynamic modeling of the Mn-Cr-O system for the oxidation of SOFC interconnect," *Solid State Ionics*, **177**, 765-777 (2006).

[26] Y.-B. Kang, I.-H. Jung and H.-G. Lee, "Thermodynamic modeling of the Mn-O system," personal communication.

[27] I.-H Jung, S. A. Decterov, and A. D. Pelton "Critical thermodynamic evaluation and optimization of the MgO-Al_2O_3, CaO-MgO-Al_2O_3 and MgO-Al_2O_3-SiO_2 systems," *Journal of Phase Equilibria and Diffusion*, **25[4]**, 329-345 (2004).

[28] Arthur D. Pelton, "A General "Geometric" Thermodynamic Model for Multicomponent Solutions," *CALPHAD: Computer Coupling of Phase Diagrams and Thermochemistry*, **25 [2]**, 319-328 (2001).

[29] P. Spencer, FSStel database, www.factsage.com (2004).

[30] A. Jansson, COST 507 (1998) ISBN 92-828-3902-8 p 54-58

[31] L. M. Lenev and I.A. Novokhatskii, "Constitutional diagram of the system MnO-Al_2O_3 and the thermodynamic properties of $MnAl_2O_4$," *Izv. Akad. Nauk. SSSR Metally.*, **3**, 73-78 (1966).

[32] C. K. Kim and A. McLean, "Thermodynamics of iron-manganese aluminate spinel inclusions in steel," *Metall. Trans. B*, **10B**, 575-584 (1979).

[33] Y. Zhao, K. Morita, and N. Sano, "Thermodynamic Properties of the $MgAl_2O_4$-$MnAl_2O_4$ Spinel Solid Solution," *Metall. Mater. Trans. B*, **26B**, 1013-17 (1995).

[34] M. Timucin and A. Muan, "Activity-Composition Relations in $NiAl_2O_4$-$MnAl_2O_4$ Solid Solutions and Stabilities of $NiAl_2O_4$ and $MnAl_2O_4$ at 1300° and 1400°C," *J. Am. Ceram. Soc.*, **75**, 1399-406 (1992).

[35] S. Dimitrov, A. Weyl, and D. Janke, "Control of the manganese-oxygen reaction in pure iron melts," *Steel Res.*, **66**, 87-92 (1995).

[36] I. Barin, Thermochemical Data of Pure Substances, VCH, Weinheim, Germany, 1989.

[37] S. Greenwald, S. J. Pickart, and F. H. Grannis, "Cation distribution and g factors of certain spinels containing Ni^{++}, Mn^{++}, Co^{++}, Al^{+++}, Ga^{+++}, and Fe^{+++}," *J. Chem. Phys.*, **22**, 1597-1600 (1954).

[38] W. L. Roth, "Magnetic properties of normal spinels with only A-A interaction," *Journal de Physique (Paris)*, **25(5)**, 507-515 (1964).

[39] N. S. S. Murthy, L. M. Rao, R. J. Begum, M. G. Natera and S. I. Youssef, “Neutron scattering studies of some spinels,” *J. Phys.*, **1**, 318-319 (1971).

[40] E. J. Essene and D. R. Peacor, “Crystal chemistry and petrology of coexisting galaxite and jacobsite and other spinel solutions and solvi,” *Am. Mineral.*, **68**, 449-455 (1983).

[41] S. Lucchesi, U. Russo and A. D. Giusta, “Crystal chemistry and cation distribution in some Mn-rich natural and synthetic spinels,” *Eur. J. Mineral.*, **9**, 31-42 (1997).

[42] N. Tristan, J. Hemberger, A. Krimmel, H-A. K. V. Nidda, V. Tsurkan, and A. Loidl, “Geometric frustration in the cubic spinels MAl_2O_4 (M = Co, Fe, and Mn),” *Phys. Rev. B*, **72**, 174404-1-9 (2005).

[43] U. Halenius, F. Bosi, and H. Skogby, “Galaxite, $MnAl_2O_4$, a spectroscopic standard for tetrahedrally coordinated Mn^{2+} in oxygen-based mineral structures,” *Am. Mineral.*, **92**, 1225-1231 (2007).

[44] U. Halenius, F. Bosi, and H. Skogby, “A first record of strong structural relaxation of TO_4 tetrahedra in a spinel solid solution,” *Am. Mineral.*, **96**, 617-622 (2011).

[45] R. A. Sharma and F. D. Richardson, “Activities of manganese oxide, sulfide capacities and activity coefficients in aluminate and silicate melts,” *Trans. Metall. Soc. A.I.M.E.*, **233**, 1586-1592 (1965).

[46] A. P. Bobov, A. G. Zalazinskii, V. F. Balakirev, Y. V. Golikov and G. I. Chufarov, “Phase equilibria during the reduction of $M_{0.25}Mn_{2.75}O_4$ solid solutions,” Zhurnal Fizicheskoi Khimii, 58[3], 750-751 (1984).

[47] FactSage 6.3, www.factsage.com, Montreal, Canada, 2012.

[48] E. L. Singleton, L. Carpenter and R. V. Lundquist, “Studies of the MnO-SiO_2 binary system,” U.S. Bur. Mines. Rept. Of Invest. No. 5938, 1-31 (1962).

[49] G. Trömel, W. Fix, K. Koch and F. Schaberg, “The phase diagram of the manganese-oxygen system,” *Erzmetall.*, **29**, 234-237 (1976).

[50] O. Kubashchewski and E. Evans, “Metallurgical thermochemistry,” Pergamon, London, 1958.

Table 4.1: Optimized model parameters of all the solutions present in the MnO-Mn_2O_3-Al_2O_3 system (J/mol and J/mol K).

Cubic Spinel: $(Mn^{2+}, Al^{3+})^T (Mn^{2+}, Mn^{3+}, Mn^{4+}, Al^{3+}, Va)_2^O O_4$

$$\Delta H_{298.15}^{O} = -2,073,402$$

$$\Delta S_{298.15}^{O} = 115.3203912$$

$$C_p = 156.0116005 + 0.028696657T - 3294506.682T^{-2} - 0.00000426112T^{2} \ (T < 2500\mathrm{K})$$

$$G_{JK} = -1,327,895.531 + 1,454.74T - 225.89T\ln T - 289,129.75T^{-1} - 2552.69$$
$$T^{-0.5} - 16,033.5\ln T (298K < T < 3000K)^{a}$$

$$G_{JJ} = -1,443,047 + 1,460.26T + 1,890,756T^{-1} - 240.5906T\ln T - 0.0162984T^{2}$$
$$(298K < T < 3000K)^{a}$$

$$I_{JF} = G_{FF} + G_{FJ} - 2G_{JF} = 31,380 + 12.552T$$

$$\Delta_{FJ:KF} = G_{FK} + G_{JF} - (G_{FF} + G_{JK}) = 41,840$$

$$\Delta_{FJ:LF} = G_{FL} + G_{JF} - (G_{FF} + G_{JL}) = 125,520$$

$${}^{1}L_{FJ:V} = {}^{1}L_{FJ:B} = {}^{1}L_{FJ:F} = {}^{1}L_{FJ:J} = {}^{1}L_{FJ:K} = {}^{1}L_{FJ:L} = -13,388.8$$

$$G_{JV} = 5/7G_{JK} + 679,021.36 - 264.99T^{a}$$

$$I_{JK} = G_{JL} + G_{JJ} - G_{JK} = 26,210 - 17.46T^{a}$$

Notations F, J, K, L and V were used for Al^{3+}, Mn^{2+}, Mn^{3+}, Mn^{4+} and vacancy, respectively. The model parameters for Al-O spinel solution could be found elsewhere (Jung *et al.* [27]).

Tetragonal Spinel: $(Mn^{2+}, Mn^{3+}, Al^{3+})^T (Mn^{2+}, Mn^{3+}, Al^{3+}, Va)_2^O O_4$

$$\Delta H_{298.15}^{O} = -2,045,579$$

$$\Delta S_{298.15}^{O} = 115.3203912$$

$$C_p = 156.0116005 + 0.028696657T - 3294506.682T^{-2} - 0.00000426112T^{2} \ (T < 2500\mathrm{K})$$

$$G_{JK} = -1,345,888.32 + 1,469.23T - 225.89T\ln T - 289,129.75T^{-1} - 2552.69$$
$$T^{-0.5} - 16,033.5\ln T (298K < T < 3000K)^{a}$$

$$G_{KJ} = G_{JK}{}^{a}$$

$$G_{KV} = 8G^{O}(\gamma\text{-Mn}_2\text{O}_3) - 2RT(5\ln 5 - 6\ln 6) - 5G_{JK} - 5I_{JK},$$

where $G^{O}(\gamma\text{-Mn}_2\text{O}_3) = G^{O}(\beta\text{-Mn}_2\text{O}_3) + 20,920^{a}$

$$\Delta_{FJ} = G_{FF} + G_{JJ} - G_{JF} - G_{FJ} = 0$$

$$\Delta_{JFK} = G_{FF} + G_{JK} - G_{JF} - G_{FK} = -125,520$$

$$\Delta_{BKF} = G_{KK} + G_{BF} - G_{BK} - G_{KF} = 0$$

$$I_{JK} = G_{KK} + G_{KJ} - 2G_{JK} = 98,324^{a}$$

$$\Delta_{JK:JK} = G_{JJ} + G_{KK} - G_{JK} - G_{KJ} = 40,000^{a}$$

$$\Delta_{JK:JV} = G_{JJ} + G_{KV} - G_{KJ} - G_{JV} = -941,190.8 + 627.6T^{a}$$

Notations F, J, K, L and V were used for Al^{3+}, Mn^{2+}, Mn^{3+}, Mn^{4+} and vacancy, respectively. The model parameters for Al-O spinel solution could be found elsewhere (Jung *et al.* [27]).

Liquid Oxide: $MnO\text{-}MnO_{1.5}\text{-}AlO_{1.5}$

$$G(\text{MnO}) = G^{O}(\text{MnO,liquid})$$

$$G(\text{MnO}_{1.5}) = 1.25G^{O}(\text{MnO,liquid}) + 25,731.6^{a}$$

$$G(\text{AlO}_{1.5}) = 1/2G^{O}(\text{Al}_2\text{O}_3\text{,liquid})$$

$$q^{00}_{\text{MnO,AlO}_{1.5}} = -6,694.4$$

$$q^{20}_{\text{MnO,AlO}_{1.5}} = 5,439.2$$

$$q^{01}_{\text{MnO,AlO}_{1.5}} = -39,329.6$$

$$q^{00}_{\text{MnO}_{1.5}\text{,AlO}_{1.5}} = -25,104$$

$$q^{01}_{\text{MnO}_{1.5}\text{,AlO}_{1.5}} = 31,380$$

$$q^{10}_{\text{MnO}_{1.5}\text{,AlO}_{1.5}} = -25,104$$

The quasichemical parameters are defined in Refs. Pelton et al. [17] and Pelton and Chartrand [18].

Monoxide: $MnO\text{-}MnO_{1.5}\text{-}AlO_{1.5}$

$$G(\text{monoxide}-\text{MnO}) = G^{O}(\text{MnO})$$

$$G(\text{monoxide}-\text{MnO}_{1.5}) = 0.5G^{O}(\text{Mn}_2\text{O}_3, \beta) + 12,001.8 - 4.87\text{T}^{a}$$

$$G(\text{monoxide}-\text{AlO}_{1.5}) = 0.5G^{O}(\text{Al}_2\text{O}_3) + 38,702$$

$$q^{31}_{\text{MnO},\text{MnO}_{1.5}} = -20,920^{a}$$

No excess parameter was required for the $MnO_{1.5}$-$AlO_{1.5}$ solution.

Bixbyite: Mn_2O_3-Al_2O_3
$G(\text{bixbyite-Mn}_2\text{O}_3) =^{a}$
$-1,512,892 + 26,796.59T - 5081T\ln T + 15.56T^{2} - 0.0081T^{3}$
$(298\text{K} < T < 320\text{K})$
$-945,439 + 813.45T - 133.5T\ln T - 0.006T^{2} + 143,152.38T^{-1} - 10,000\ln T$
$(320K < T < 3000K)$
$G(\text{bixbyite-Al}_2\text{O}_3) = G^{O}(\text{Al}_2\text{O}_3) + 37,656$
$q^{31}_{\text{Mn}_2\text{O}_3,\text{Al}_2\text{O}_3} = 8,368 - 13.3888T$

Corundum: Al_2O_3-Mn_2O_3
$G(\text{corundum-Al}_2\text{O}_3) = G^{O}(\text{corundum-Al}_2\text{O}_3)^{b}$
$G(\text{corundum-Mn}_2\text{O}_3) = G^{O}(\text{bixbyite-Mn}_2\text{O}_3)^{b}$

Other Gibbs energies of the gas components are obtained from the FACTPS database (Factsage [47]).

[a] The model parameters for the Mn-O system were optimized previously by Kang *et al.* [26].

[b] The Gibbs energy of the corundum species are obtained from the FToxid database (Factsage [47]).

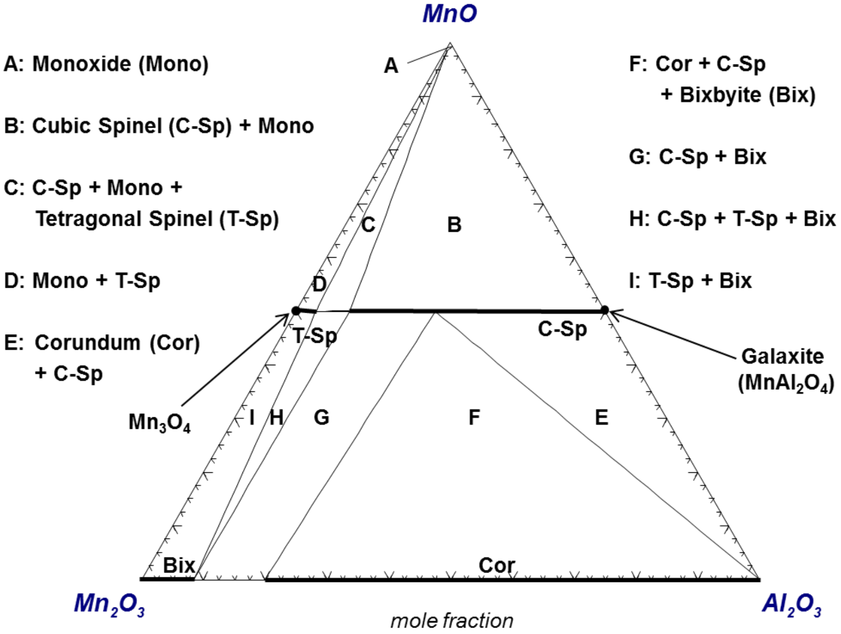

Figure 4.1: Calculated phase diagram of the MnO-Mn_2O_3-Al_2O_3 system at 1000°C and 1 bar total pressure.

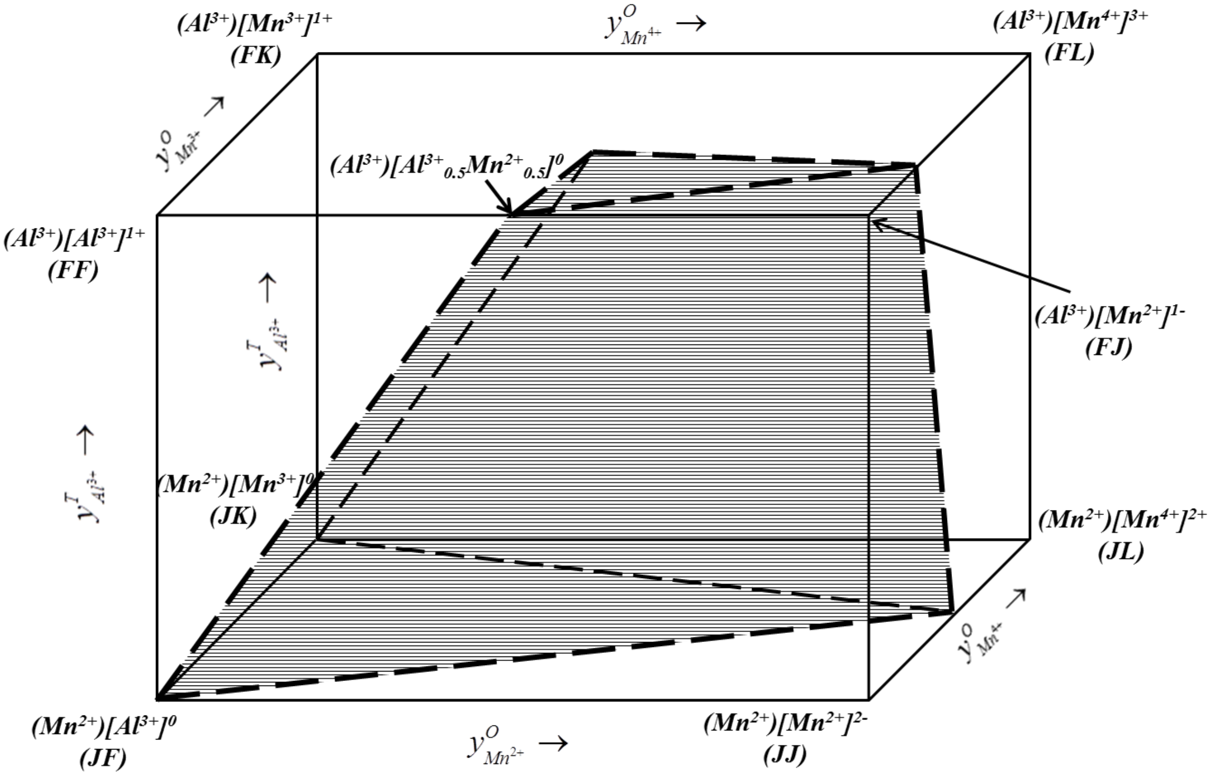

Figure 4.2: Gibbs energy diagram for the spinel Mn_3O_4-$MnAl_2O_4$ solution

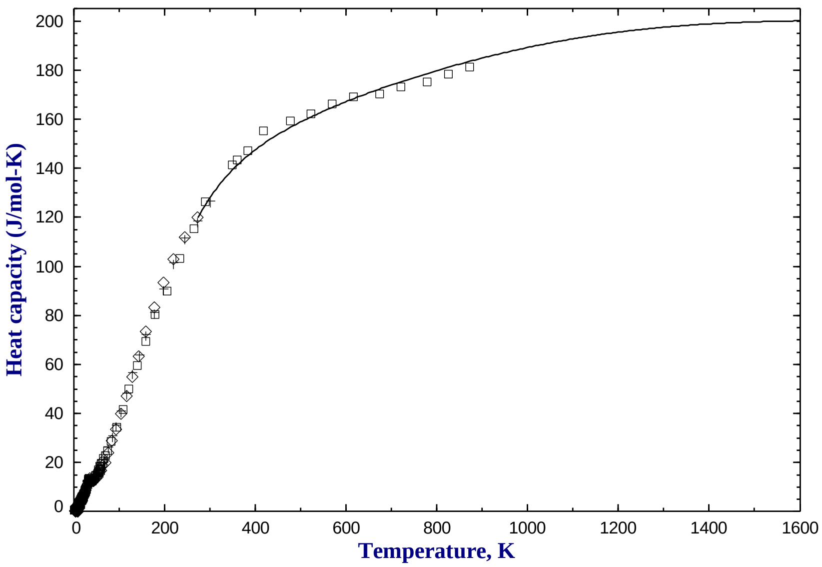

Figure 4.3: Heat capacity of $MnAl_2O_4$ calculated from the present spinel solution model along with experimental data by Navarro *et al.* [12].

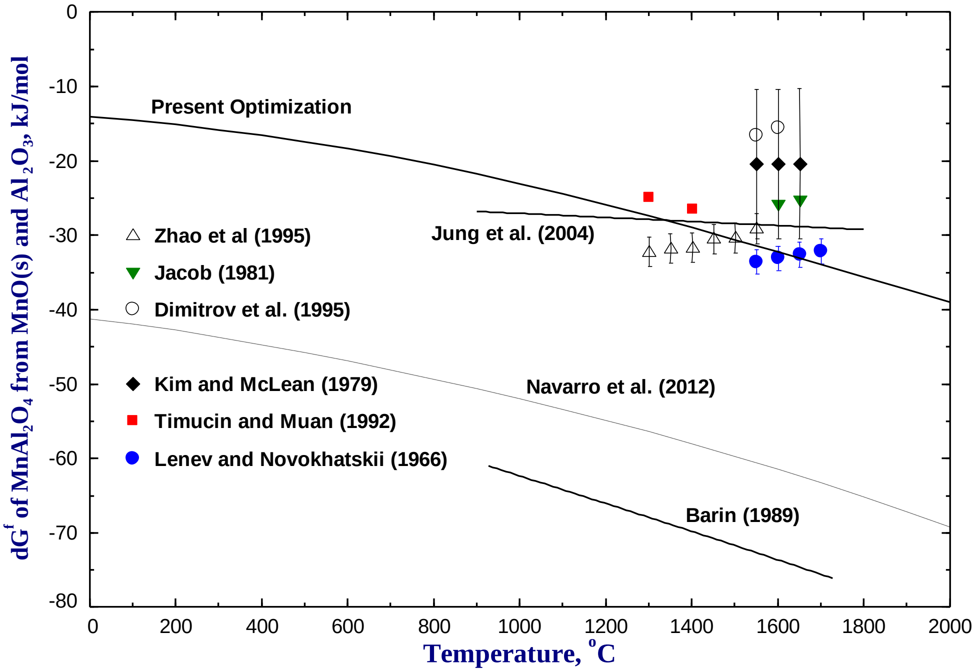

Figure 4.4: Optimized isothermal Gibbs energy of formation of $MnAl_2O_4$ from solid MnO and Al_2O_3 along with experimental data by Lenev and Novokhatskii [31], Kim and McLean [32], Jacob [7], Timucin and Muan [34], Dimitrov *et al.* [35] and Zhao *et al.* [33] and evaluated and calculated results obtained from previous studies by Barin [36], Jung *et al.* [10] and Navarro *et al.* [12]).

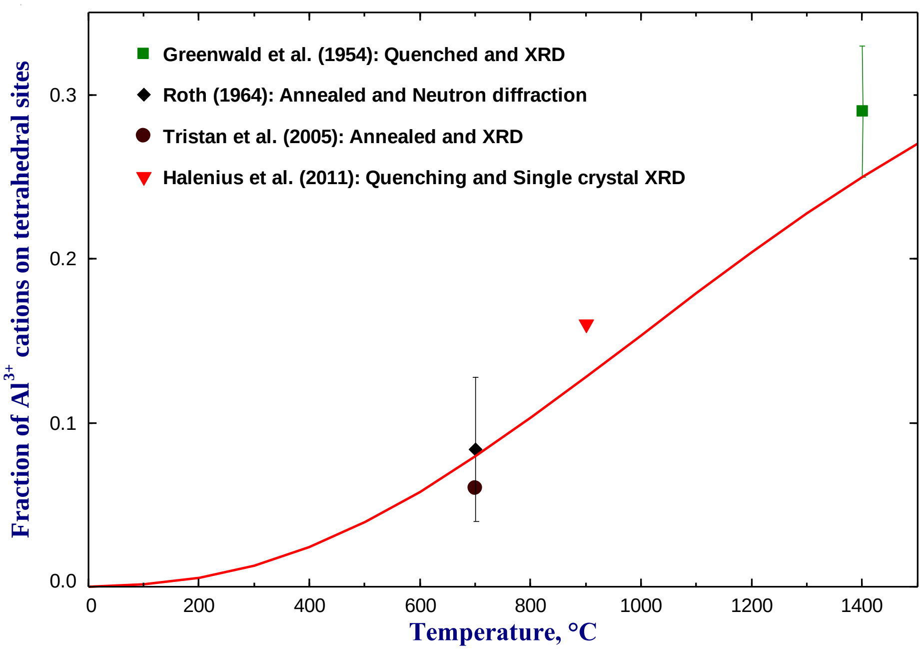

Figure 4.5: Calculated variation of cation distribution in $MnAl_2O_4$ as a function of temperature in °C along with experimental data of Greenwald et al. [37], Roth [38], Tristan *et al.* [42] and Halenius [44].

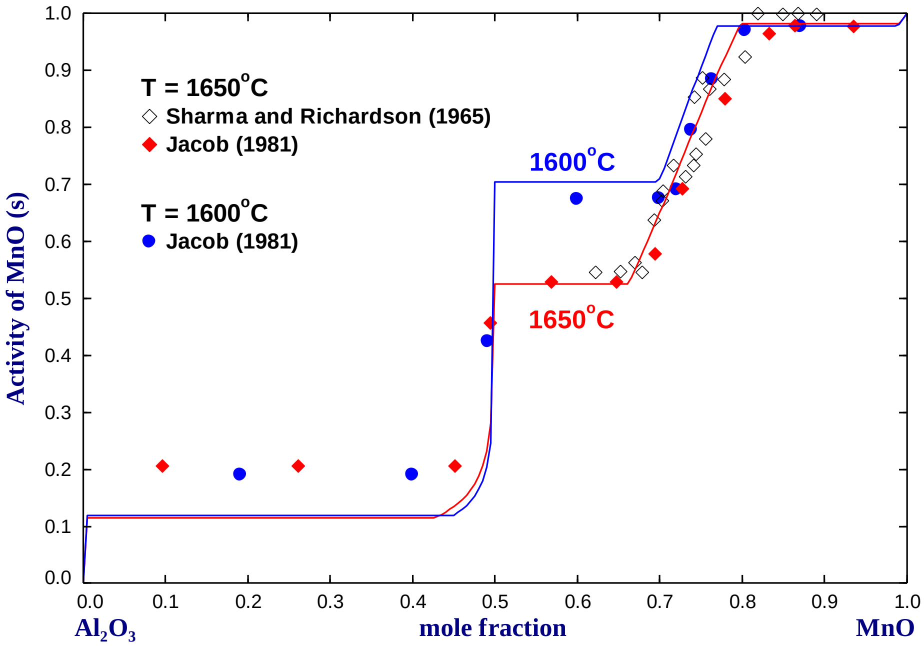

Figure 4.6: The activity of MnO in the $MnO\text{-}Al_2O_3$ system at 1600°C (blue line) and 1650°C (red line) under reducing atmosphere. Points are from Sharma and Richardson [45] and Jacob [7] and the lines are calculated from the present study.

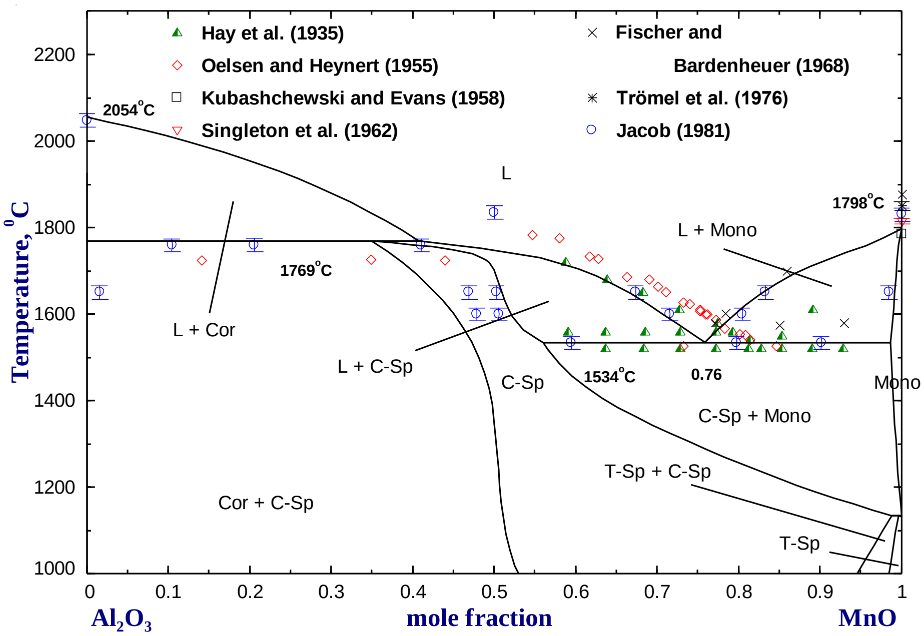

Figure 4.7 (a)[1]: Calculated phase diagram of the Mn-Al-O system under reducing condition (p_{O_2}= 10^{-5} atm) with experimental points by Hay *et al.* [1], Oelsen and Heynert [2], Kubaschchewski and Evans [50], Singleton *et al.* [48], Fischer and Bardenheuer [5], Trömel *et al.* [49] and Jacob [7].

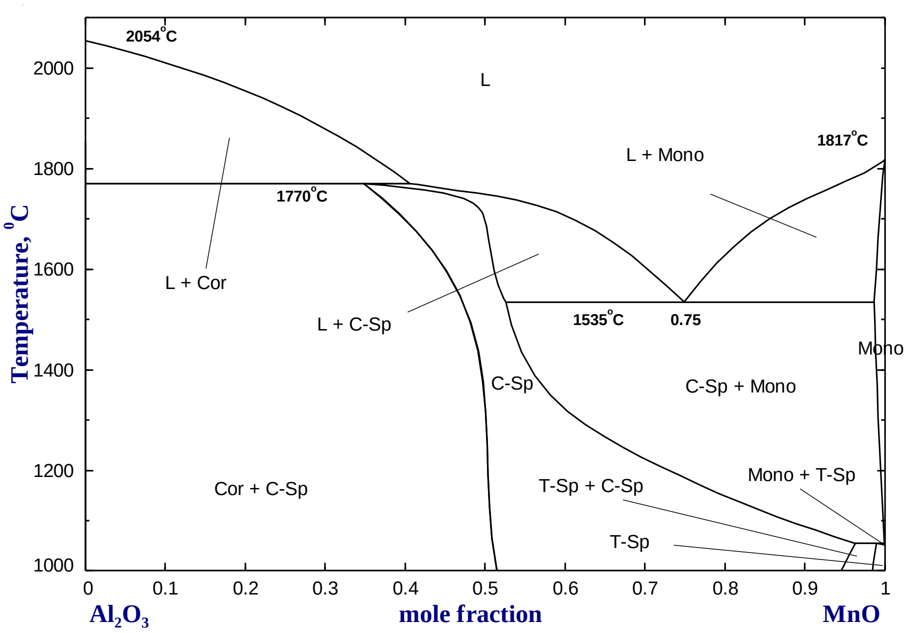

Figure 4.7 (b)[1]: Calculated phase diagram of the Mn-Al-O system under reducing condition (p_{O_2}= 10^{-6} atm).

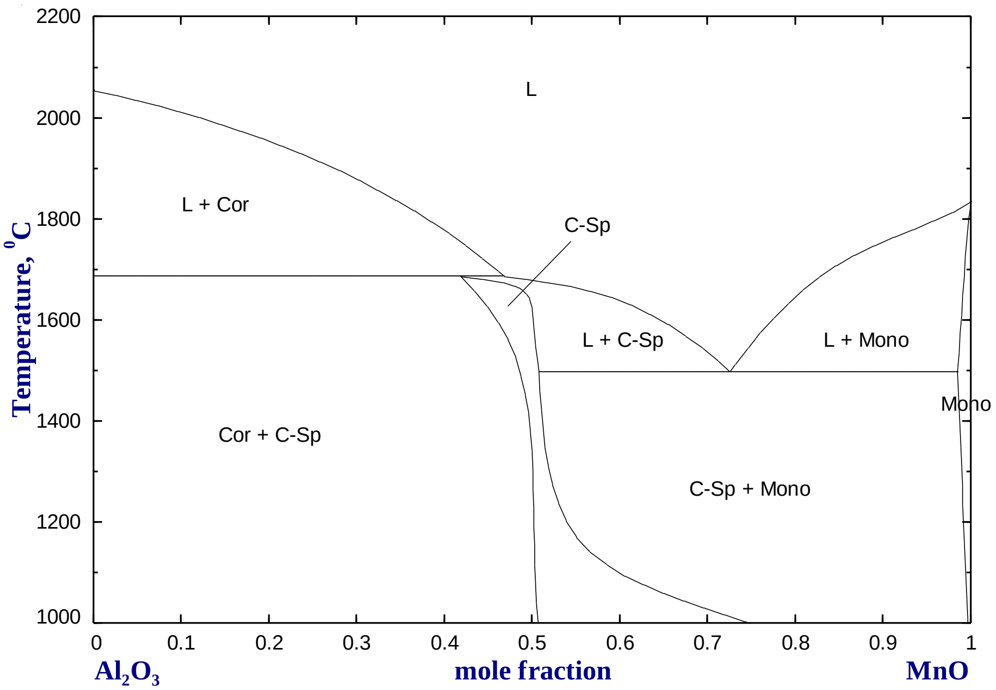

Figure 4.7 (c)[1]: Predicted phase diagram of the Mn-Al-O system under reducing condition (p_{O_2}= 10^{-8} atm).

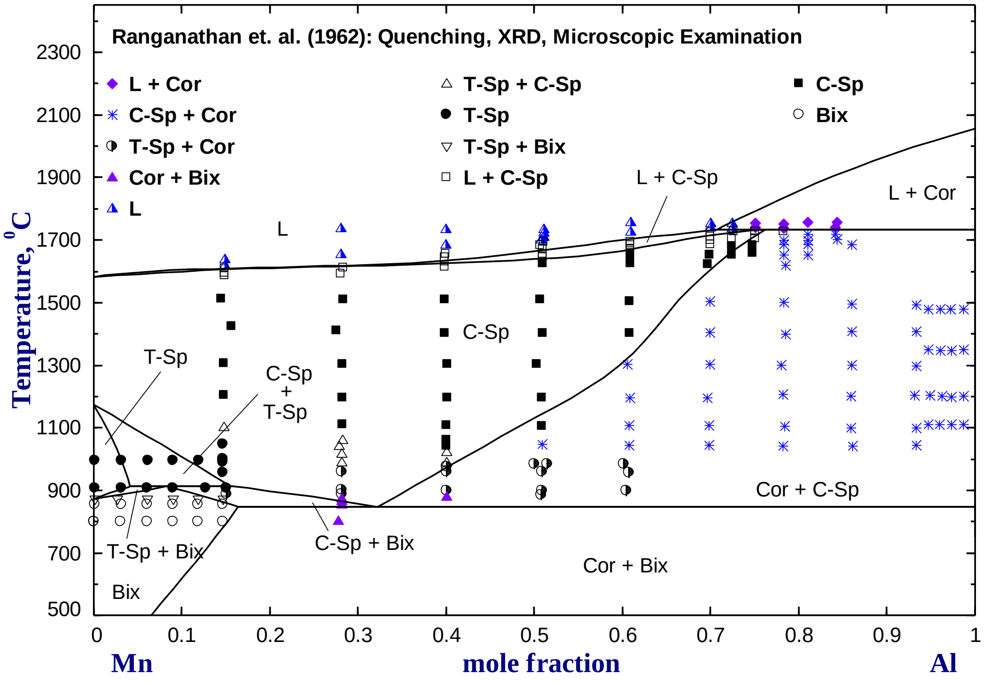

Figure 4.8 (a)[1]: Calculated phase diagrams of the Mn-Al-O system in air along with the experimental points by Ranganathan *et al.* [3].

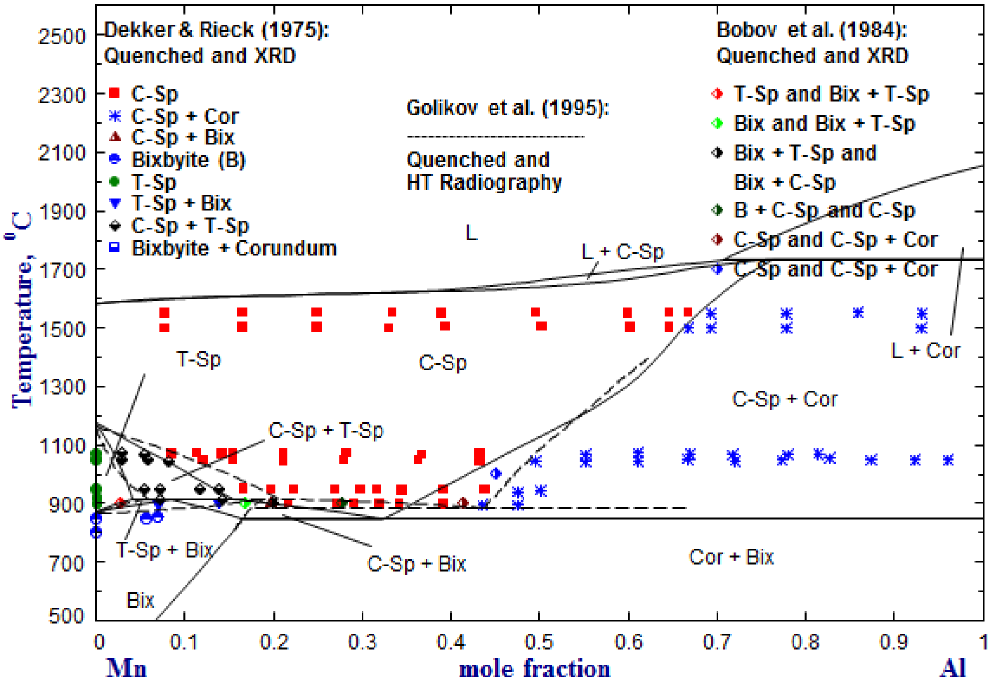

Figure 4.8 (b)[1]: Calculated phase diagrams of the Mn-Al-O system in air along with the experimental points by Dekker and Rieck [6], Bobov *et al.* [46] and Golikov *et al.* [8].

[1] Abbreviations: L: Slag, C-Sp: Cubic Spinel, T-Sp: Tetragonal Spinel, Mono: Monoxide, Cor : Corundum, Bix : Bixbyite.

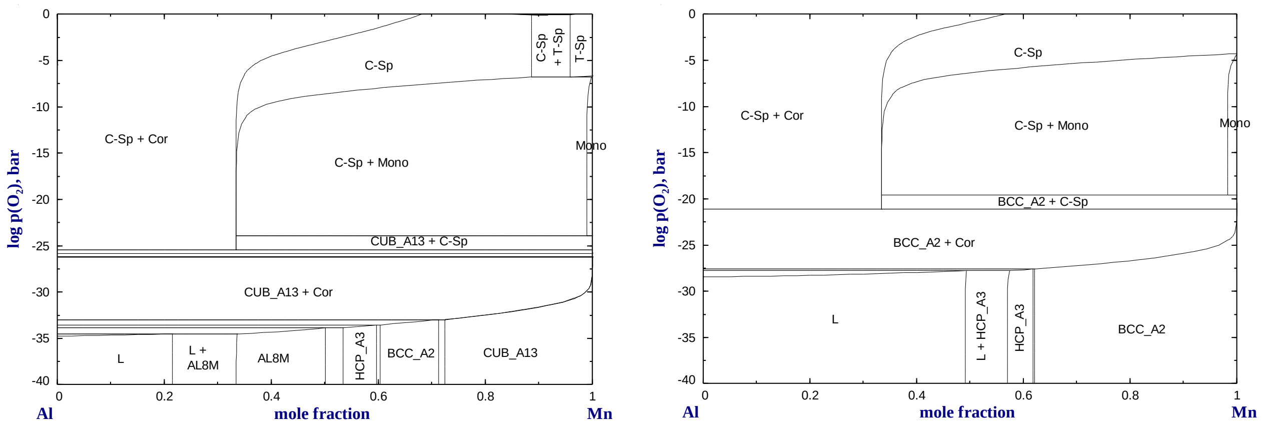

(a) (b)

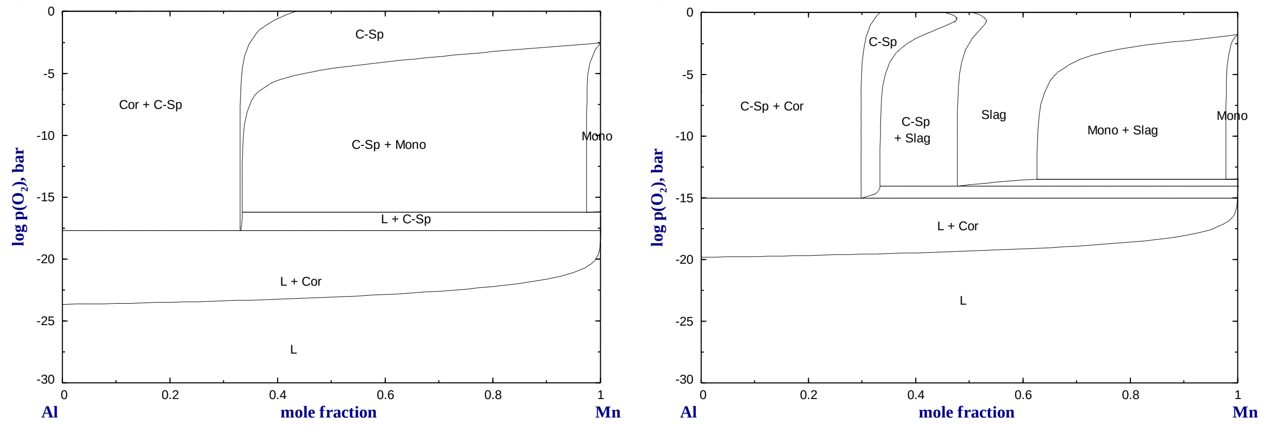

(c) (d)

Figure 4.9[2] : Calculated (predicted) Mn-Al-O phase diagrams at temperatures of : (a) 1000°C, (b) 1200°C, (c) 1400°C and (d) 1600°C. Molar metal ratio versus equilibrium oxygen partial pressure.

[2] Abbreviations: L: Liquid, C-Sp: Cubic Spinel, T-Sp: Tetragonal Spinel, Mono: Monoxide, Cor : Corundum, AL8M: AL8MN5D810.

Chapter 5

Thermodynamic modeling of the MnO-Mn_2O_3-Al_2O_3-SiO_2-CaO system

5.1 Introduction

The thermodynamic optimization of the MnO-Mn_2O_3-Al_2O_3-SiO_2-CaO system had been carried out earlier. However, the same work has to be repeated since the MnO-Mn_2O_3-Al_2O_3 (Chapter 4) system has been reoptimized considering $MnAl_2O_4$ as a spinel solid solution and considering Mn^{3+} species in the slag as described in Chapter 4. The optimized MnO-Mn_2O_3-Al_2O_3 (Chapter 4) system has been extended to the MnO-Mn_2O_3-Al_2O_3-SiO_2-CaO system in the present chapter by combining with the previously optimized model parameters for the system present in the FToxid database [1].

5.2 Phases and thermodynamic models

The schematic diagram of the Mn-Al-Si-Ca-O (MnO-Al_2O_3-SiO_2-CaO) system is shown in Fig. 5.1. The following solution phases are found in the Mn-Al-O system:

Spinel: $(Mn^{2+}, Al^{3+})^T (Al^{3+}, Mn^{2+}, Mn^{3+}, Mn^{4+}, Va)_2^O$O4
Mullite: $Al_6Si_2O_{13}$ having a little solubility of Al_2O_3.
Corundum: $(Al^{3+}, Mn^{2+})_2O_3$
Slag (molten oxide phase): MnO-Mn_2O_3-Al_2O_3-SiO_2-CaO
Monoxide: MnO-$AlO_{1.5}$-$MnO_{1.5}$-CaO-SiO_2
Rhodonite: $(Mn^{2+}, Ca^{2+})[Si^{4+}]O_3$
Olivine: $(Mn^{2+}, Ca^{2+})_2[Si^{4+}]O_4$

The ternary compounds observed in the system are as follows:
Spessartite ($Mn_3Al_2Si_3O_{12}$)
Mn-Cordierite ($Mn_2Al_4Si_5O_{18}$)

No change has been made to the parameters related to any of the solid solutions present in the MnO-Al_2O_3-SiO_2-CaO system; all the required parameters have been obtained from the FToxid database [1].

As there is no extension of the binary or ternary solid solution toward higher order system, no thermodynamic modeling is needed for the solid solutions. In the case of liquid slag, all slag components are mixed together. So, the ternary interactions of the components can be re-optimized to reproduce all available experimental data related to liquid phase. In particular, ternary interaction parameters of the MnO-Al_2O_3-SiO_2 system were needed to be re-optimized because of the change of the model parameters for the MnO-Al_2O_3 system. In addition, the Gibbs energies of ternary compounds were also changed slightly to accommodate the change of liquid phase to reproduce the phase diagram.

5.2.1 Slag

Only the ternary parameters of MnO-Al_2O_3-SiO_2 slag were changed in the present study. No other parameter related to the slag phases was changed.

The Gibbs energy of the ternary liquid surface was calculated with the help of the Modified Quasichemical model using the “asymmetric approximation (Toop-like interpolation technique)” given by Chartrand and Pelton [2], Pelton [3] along with the binary parameters of the subsystems and ternary parameters. In the present asymmetric approximation, SiO_2 was considered as the acidic component and MnO and Al_2O_3 as the basic components. Fig. 5.2 shows the geometric model used in the current interpolations.

The optimized parameters for the previously optimized binary subsystems were used alongwith two small ternary parameters to obtain the Gibbs energy of the ternary liquid surface. All these parameters are shown in Table 5.1

5.2.2 Ternary compounds

Snow [4] observed two ternary compounds, Spessartite ($Mn_3Al_2Si_3O_{12}$) and Mn-cordierite ($Mn_2Al_4Si_5O_{18}$) in the MnO–Al_2O_3–SiO_2 system. The heat capacity and entropy were taken from

Jung *et al.* [5]. The enthalpy of formation at 298 K, H_{298}^{o}, was optimized in the present study to reproduce the experimental phase diagram data. The optimized values are shown in Table 5.1.

5.3 Critical evaluation and optimization

5.3.1 MnO-Al_2O_3-Mn_2O_3-SiO_2 system

This MnO-Al_2O_3-SiO_2 system consists of the following binary subsystems:

a. Al-Si-O system: The thermodynamic optimization of this system has already been done by Eriksson and Pelton [6].
b. Mn-Si-O system: The thermodynamic optimization of this system has already been done by Eriksson *et al.* [7].
c. Mn-Al-O system: The thermodynamic optimization of this system has already been shown in chapter 4.

Fig. 5.3 and 5.4 show the calculated phase diagrams of the Al_2O_3-SiO_2 and MnO-SiO_2 binary systems from the optimized model parameters stored in FToxide database [1]. All experimental data related to phase diagrams, cation distribution and thermodynamic properties were considered in the modeling. All the previous model parameters were used in the present study without any modification.

Jung *et al.* [5] performed all the thermodynamic optimizations related to the MnO-Al_2O_3-SiO_2 system. However, $MnAl_2O_4$ was considered as a stoichiometric compound in their study rather than a spinel solution and no Mn^{3+} in the liquid was considered. In the present study, the thermodynamic calculations for the MnO-Al_2O_3-SiO_2 system were performed using the present revised Mn-Al-O system containing spinel solution and $MnO_{1.5}$ oxide in slag. In summary, the accuracy of the thermodynamic modeling of the present study is compatible with the previous study by Jung *et al.* [5]. The details of the present optimization are given below.

The maximum mole fraction of Mn_2O_3 in the MnO-Mn_2O_3-Al_2O_3-SiO_2 slag phase at 1600°C is as low as 0.0001 which is very low. The optimized liquidus surface of the MnO-Mn_2O_3-Al_2O_3-

SiO_2 system under reduced oxygen condition (Fe saturation) is shown in Fig. 5.5(b). It can be compared with the previously optimized liquidus projection which has been shown in Fig. 5.5 (a)). All the calculated primary phase regions of the MnO-Al_2O_3-SiO_2 system at Fe saturation, compared with the experimental points of Snow [4] and Roghani *et al.* [8], are depicted in Fig. 5.6. The primary phase boundary of mullite and corundum are slightly lower in SiO_2 content than the experimental data. Consequently, the primary phase field of corundum is slightly smaller than the experimental one.

The liquidus experimental data of the ternary MnO-Al_2O_3-SiO_2 system at reduced oxygen conditions are well reproduced between 1200 and 1600^oC, as it can be seen in Fig. 5.7. Sharma and Richardson [9] and Woo *et al.* [10] determined the activities of MnO in the MnO-Al_2O_3-SiO_2 system at 1650 and 1550^oC, respectively. The calculated iso-activity lines in Fig. 5.8 are in good agreement with experimental data. Several researchers also investigated the variation of activity of MnO and SiO_2 along the liquidus at 1550, 1600 and 1650^oC as presented in Fig. 5.9 and 5.10. The experimental data are well reproduced in the present calculations.

In the present work, small ternary interaction parameters for the slag have been used. Moreover, the enthalpies of the two ternary compounds have been changed in order to reproduce the experimental data. The results obtained from the present work are in very good agreement with the previously optimized results of Jung *et al.* [5].

The calculated ternary invariant points are listed in Table 5.2. A comparison of these calculated points with those obtained experimentally by Snow [4] shows good agreement within the experimental uncertainty.

Unfortunately, no experimental data were available for the Mn-Al-Si-O system at high oxygen potential. So, it is difficult to evaluate the ternary model parameters for the Mn_2O_3-Al_2O_3-SiO_2 system, and therefore the ternary parameters were set to be zero in the present study.

Calculations based on good thermodynamic databases can be used to obtain thermodynamic information for liquid steel and their inclusions which can be helpful in obtaining inclusions of specific compositions. All the calculations related to inclusion chemistry in the Mn_2O_3-Al_2O_3-SiO_2 system done by Jung *et al.* [5] have been repeated here with the updated database. The change in inclusion compositions obtained with the present study is almost identical to the previous results of Jung *et al.* [5] as shown in Fig. 5.11 and 5.12.

5.3.2 CaO-MnO-Mn_2O_3-Al_2O_3 system

The CaO-MnO-Al_2O_3 ternary system consists of three binary subsystems:

a. Ca-Mn-O system: The thermodynamic optimization of this system has already been done by Wu *et al.* [11].
b. Ca-Al-O system: The thermodynamic optimization of this system has already been done by Eriksson and Pelton [6].
c. Mn-Al-O system: The thermodynamic optimization of this system has already been shown in chapter 4.

Fig. 5.13 and 5.14 show the calculated phase diagrams of the CaO-MnO and CaO-Al_2O_3 binary systems from the optimized model parameters stored in FToxide database [1]. All experimental data related to phase diagrams and thermodynamic properties were considered in the modeling. All the previous model parameters of the subsystems were used in the present study without any modification.

The maximum mole fraction of Mn_2O_3 in the CaO-MnO-Mn_2O_3-Al_2O_3 slag phase at 1600°C is as low as 0.0001 which is very low. The optimized liquidus surface of the CaO-MnO-Al_2O_3 system under reduced oxygen condition (Fe saturation) is shown in Fig. 5.15(b). It can be compared with the previously optimized liquidus projection as shown in Fig. 5.15 (a).

Any phase diagram study of the CaO-MnO-Al_2O_3 system is yet to be reported in literature.

The Gibbs energy of the ternary liquid surface was calculated with the help of the Modified Quasichemical model using the “asymmetric approximation (Toop-like interpolation technique)” given by Chartrand and Pelton [2], Pelton [3] along with the parameters of the binary subsystems. In the present asymmetric approximation, Al_2O_3 was considered as the asymmetric component and CaO and MnO as the symmetric components. No additional ternary parameters were considered.

The calculated activities for MnO in the ternary slags have been compared with the available experimental data and the results are depicted in fig. 5.16.

5.3.3 CaO-MnO-Mn_2O_3-Al_2O_3-SiO_2 system

The CaO-MnO-Al_2O_3-SiO_2 ternary system consists of three ternary subsystems:

a. Ca-Al-Si-O system: The thermodynamic optimization of this system has already been done by Eriksson and Pelton [6].
b. Mn-Al-Si-O system: The thermodynamic optimization of this system has already been shown in section **5.3.1** above.
c. Ca-Mn-Si-O system: The thermodynamic optimization of this system has already been done by Kang *et al.* [12].
d. Ca-Mn-Al-O system: The thermodynamic optimization of this system has already been discussed in section **5.3.2** above.

The optimized parameters of the ternary sub-systems are used to predict the thermodynamic properties of the of the phases present in the 4-component system using the recently developed approximation methods by Chartrand and Pelton [2], Pelton [3]. There was no need to use any additional model parameters.

The maximum mole fraction of Mn_2O_3 in the CaO-MnO-Al_2O_3-SiO_2 slag phase at 1600°C is as low as 0.00007 which is very low.

Fig. 5.17 shows the comparison between the activities of MnO (solid standard state) calculated from the present study along with the experimental data. The calculated data are in agreement with the experimental data except for the slag with composition ‘K’. The point to be noted here is that the compositions of the slags with compositions ‘C’ and ‘K’ are similar and the agreement of the calculated values for ‘C’ with corresponding experimental values is good.

The first attempt to determine the liquidus of the CaO-MnO-Al_2O_3-SiO_2 system was made by Rait and Olsen [13] by determining the composition of slags with Al_2O_3/SiO_2 weight ratios of 0.25 and 0.5. Preparation of the master slags was done from pure oxides. Melting of the slags was carried out in graphite crucibles under Argon atmosphere in a Balzer induction furnace. The samples were heated at 1450°C, 1500°C and 1550°C for 1.5 hours followed by quenching in water baths. The compositions of the liquid slag in the quenched samples were determined by EPMA.

Recently, Roghani *et al.* [14] and Kang *et al.* [15] carried out similar experiments with slags of Al_2O_3/SiO_2 weight ratios of approximately 0.41 at various temperatures. The Fig. 5.18 (a) and (b) show the predicted liquidus surface of the monoxide phase at 1450°C, 1500°C and 1550°C with Al_2O_3/SiO_2 weight ratios of 0.25 and 0.5 respectively. The experimental data are in good agreement with the calculated liquidus lines.

The Fig. 5.19 shows the calculated liquidus surface at an Al_2O_3/SiO_2 weight ratio of 0.41 at 1200°C and 1300°C. The experimental points from Roghani *et al.* [14] and Kang *et al.* [15] were also plotted although the Al_2O_3/SiO_2 weight ratio varied from 0.39-0.46 and 0.34-0.46 respectively. The Fig. shows that the calculations are in good agreement with the experimental points of Kang *et al.* [15]. However, they are only in agreement with the experimental points of Roghani *et al.* [14] only for the monoxide liquidus. The reported compositions of Gehlenite in equilibrium with liquid by Roghani *et al.* [14] deviated significantly from the stoichiometric composition, whereas those reported by Kang *et al.* [15] were in very good agreement with stoichiometric $Ca_2SiAl_2O_7$. Moreover, the Gehlenite grains obtained in the study of Roghani *et al.* [14] were much smaller than that obtained in the study of Kang *et al.* [15]. These results seem to suggest that probably full equilibrium conditions were not achieved by Roghani *et al.* [14] and as a result the experimental points showing the Gehlenite liquidus is not in agreement with the calculated Gehlenite liquidus. However, the same explanation doesn't hold for the case of Anorthite liquidus since the solid Anorthite compositions reported by Roghani *et al.* [14] were close to the stoichiometric composition. Hence, this discrepancy remains unsolved.

5.3.4 Other systems at oxidizing atmosphere

There is no experimental data available for any other subsystem in oxidizing condition. Hence, Factsage [1] can be used along with proper database to predict phase relationships in any system at any condition.

5.4 Summary

The previous work in the Mn-Al-O system has been extended to the $MnO-Al_2O_3-SiO_2-CaO$ system. Except few changes in the ternary parameters for the $MnO-Al_2O_3-SiO_2$ system, no other change in the model parameters has been done. All the calculations in the $MnO-Al_2O_3-SiO_2-CaO$ system which were previously done have been performed again with the newly obtained database. All the present results have been compared with the previously optimized results and they are found to show good agreement with each other and the experimental data.

References

[1] FactSage 6.3, www.factsage.com, Montreal, Canada, 2012.

[2] Patrice Chartrand and Arthur D. Pelton, “On the Choice of “Geometric” Thermodynamic Models,” *Journal of Phase Equilibria*, **21**, 141-147 (2000).

[3] Arthur D. Pelton, “A General “Geometric” Thermodynamic Model for Multicomponent Solutions,” *CALPHAD: Computer Coupling of Phase Diagrams and Thermochemistry*, **25 [2]**, 319-328 (2001).

[4] R.B. Snow, “Equilibrium relationships on the liquidus surface in part of $MnO-Al_2O_3-SiO_2$ system,” *J. Am. Ceram. Soc.*, **26**, 11-20 (1943).

[5] I-H Jung, Y-B Kang, S.A. Decterov, and A.D. Pelton “Thermodynamic evaluation and optimization of the $MnO-Al_2O_3$ and $MnO-Al_2O_3-SiO_2$ systems and applications to inclusion engineering,” *Metall. Mater. Trans. B*, **35B**, 259-268 (2004).

[6] G. Eriksson and A.D. Pelton, “Critical evaluation and optimization of the thermodynamic properties and phase diagrams of the $CaO-Al_2O_3$, $Al_2O_3-SiO_2$, and CaO- $Al_2O_3-SiO_2$ systems,” *Metall. Mater. Trans. B*, **24B**, 807-816 (1993).

[7] G. Eriksson, P. Wu, M. Blander, and A.D. Pelton, “Critical evaluation and optimization of the thermodynamic properties and phase diagrams of the $MnO-SiO_2$ and $CaO-SiO_2$ systems,” *Can. Metall. Q.*, 33, 13-22 (1994)

[8] G. Roghani, E. Jak, and P. Hayes, “Phase Equilibrium Studies in the “MnO”-$Al_2O_3-SiO_2$ System,” *Metall. Mater. Trans. B*, **33[6]**, 827-838 (2002).

[9] R. A. Sharma and F. D. Richardson, “Activities of manganese oxide, sulfide capacities and activity coefficients in aluminate and silicate melts,” *Trans. Metall. Soc. A.I.M.E.*, **233**, 1586-1592 (1965).

[10] D.-H. Woo, Y.-B. Kang, and H.-G. Lee, “Thermodynamic study of $MnO-SiO_2-Al_2O_3$ slag system: liquidus lines and activities of MnO at 1823K,”*Metall. Mater. Trans. B*, **33B**, 915-920 (2002).

[11] P. Wu, G. Eriksson and A.D. Pelton, “Critical evaluation and optimization of the thermodynamic properties and phase diagrams of the CaO-FeO, CaO-MgO, CaO-MnO, FeO-MgO, FeO-MnO, and MgO-MnO systems,” *J. Am. Ceram. Soc.*, **76[8]**, 2065-2075 (1993).

[12] Y.-B. Kang, I.-H. Jung, S. A. Decterov, A. D. Pelton and Hae-Geon Lee, "Critical Thermodynamic Evaluation and Optimization of the CaO-MnO-SiO_2 and CaO-MnO-Al_2O_3 systems," *ISIJ International*, **44[6]**, 965-974 (2004)

[13] R. Rait and S. E. Olsen, "Liquidus relations of ferromanganese slags," *Scand. J. Metall.*, **28**, 53-58 (1999).

[14] G. Roghani, E. Jak, and P. Hayes, "Phase equilibrium data and liquidus for the system "MnO"-CaO-(Al_2O_3+SiO_2) at $Al_2O_3/SiO_2 = 0.41$," *Metall. Mater. Trans. B*, **33[6]**, 839-849, (2002).

[15] Y.-B. Kang, I-H Jung, S. A. Decterov, A. D. Pelton and H.-G. Lee, "Phase equilibria and thermodynamic properties of the CaO-MnO-Al_2O_3-SiO_2 system by critical evaluation, modeling and experiment," *ISIJ International*, **44[6]**, 975-983 (2004).

[16] Y.-B. Kang, I.-H. Jung and H.-G. Lee, "Thermodynamic modeling of the Mn-O system," personal communication.

[17] Sakao, *Tetsu-to-Hagané*, **56**, S621-S624 (1970).

[18] T. Fujisawa and H. Sakao, "Equilibrium between MnO-Al_2O_3-SiO_2-FeO slags and liquid steel," *Tetsu-to-Hagané*, **63**, 1504-1511 (1977).

[19] H. Ohta and H. Suito, "Activities in MnO-SiO_2-Al_2O_3 slags and deoxidation equilibria of Mn and Si," *Metall. Mater. Trans. B*, **27B**, 263-70 (1996).

[20] Y.-B. Kang and H.-G. Lee, "Inclusion chemistry for Mn/Si deoxidized steels: thermodynamic predictions and experimental confirmations," *ISIJ International*, **44[6]**, 1006-1015 (2004).

[21] K. T. Jacob, "Revision of thermodynamic data on MnO-Al_2O_3 melts," *Can. Metall. Quater.*, **20[1]**, 89-92 (1981).

[22] K. Morita, M. Miwa and M. Ohta, *Proc. of 2nd Int. Cong. On the Sci. and Tech. of Steelmaking, Institute of Metals, London*, 593, (2001).

[23] K. P. Abraham, M. W. Davies and F. D. Richardson, "Activities of manganese oxide in silicate melts," *J. Iron Steel Inst.*, **196**, 82-89 (1960).

[24] A. Di Donato and P. Granati, *Proc. of 6th Int. Conf. Molten Slags, Fluxes and Salts, KTH, Stockholm*, CD-ROM No.037, (2000).

[25] 65Meh: S.R. Mehta and F. D. Richardson, “Activities of manganese oxide and mixing relationships in aluminate and silicate melts,” *J. Iron Steel Inst.*, **203**, 524-528 (1965).

Table 5.1: Optimized model parameters of the liquid oxide present in the MnO-$MnO_{1.5}$-$AlO_{1.5}$-SiO_2 system (J/mol and J/mol K).

Liquid Oxide: MnO-$MnO_{1.5}$-$AlO_{1.5}$-SiO_2

$$G(\mathrm{MnO}) = G^{O}(\mathrm{MnO,liquid})$$

$$G(\mathrm{MnO_{1.5}}) = 1.25G^{O}(\mathrm{MnO,liquid}) + 25,731.6^{a}$$

$$G(\mathrm{AlO_{1.5}}) = 1/2G^{O}(\mathrm{Al_2O_3,liquid})$$

$$q^{00}_{\mathrm{MnO,AlO_{1.5}}} = -6,694.4^{b}$$

$$q^{20}_{\mathrm{MnO,AlO_{1.5}}} = 5,439.2^{b}$$

$$q^{01}_{\mathrm{MnO,AlO_{1.5}}} = -39,329.6^{b}$$

$$q^{00}_{\mathrm{MnO_{1.5},AlO_{1.5}}} = -25,104^{b}$$

$$q^{00}_{\mathrm{MnO,SiO_2}} = -79,955.3 + 20.91977T^{c}$$

$$q^{07}_{\mathrm{MnO,SiO_2}} = 228,817.9 - 62.7598T^{c}$$

$$q^{05}_{\mathrm{MnO_{1.5},SiO_2}} = 41,840^{c}$$

$$q^{00}_{\mathrm{AlO_{1.5},SiO_2}} = 4,799.866^{d}$$

$$q^{30}_{\mathrm{AlO_{1.5},SiO_2}} = 100,783.9^{d}$$

$$q^{50}_{\mathrm{AlO_{1.5},SiO_2}} = 142,067^{d}$$

$$q^{70}_{\mathrm{AlO_{1.5},SiO_2}} = 78,571.06^{d}$$

$$q^{002}_{\mathrm{MnO,SiO_2(AlO_{1.5})}} = -41,840^{e}$$

$$q^{001}_{\mathrm{AlO_{1.5},SiO_2(MnO)}} = -41,840$$

Note: there is no ternary parameter for the Mn_2O_3-Al_2O_3-SiO_2, Mn_2O_3-MnO-SiO_2 and Mn_2O_3-MnO-Al_2O_3 systems.

Stoichiometric compounds				
Phase	Temperature Range (K)	$H^o_{298.15}$	$S^o_{298.15}$	C_p
Spessartite ($Mn_3Al_2Si_3O_{12}$)	298 to 1475	-5,662,394.485	$S^O_{298.15} = 3S^O_{298.15}(\mathrm{MnO(s)}) + S^O_{298.15}(\mathrm{Al_2O_3(s)}) + 3S^O_{298.15}(\mathrm{SiO_2(tr)})$	$C_p = 3C_p(\mathrm{MnO(s)}) + C_p(\mathrm{Al_2O_3(s)}) + 3C_p(\mathrm{SiO_2(tr)})$
Mn-Cordierite ($Mn_2Al_4Si_5O_{18}$)	298 to 1453	-8,747,113.142	$S^O_{298.15} = 2S^O_{298.15}(\mathrm{MnO(s)}) + 2S^O_{298.15}(\mathrm{Al_2O_3(s)}) + 5S^O_{298.15}(\mathrm{SiO_2(tr)})$	$C_p = 2C_p(\mathrm{MnO(s)}) + 2C_p(\mathrm{Al_2O_3(s)}) + 5C_p(\mathrm{SiO_2(tr)})$

[a] The model parameters for the Mn-O system were optimized previously by Kang *et al.* [16].

[b] The model parameters for the Mn-Al-O system have been obtained from Chapter 4.

[c] The model parameters for the Mn-Si-O system were optimized previously by Eriksson *et al.* [7].

[d] The model parameters for the Al-Si-O were optimized previously by Eriksson and Pelton [6].

[e] The model parameters for the Mn-Al-Si-O system were optimized previously by Jung *et al.* [5].

Table 5.2: Comparison of calculated ternary invariant points (not in parentheses) with reported values of Snow [4] (in parentheses).

Invariant reaction[1]	Composition (wt. %)			Temperature (°C)
	MnO	Al_2O_3	SiO_2	

L → Sp + Tr + Mn-Crd	33.123(30)	17.34(19)	49.537(51)	1141.53(1140±10)
L + Tr + Mu → Mn-Crd	28.48(24)	20.122(23)	51.399(53)	1188.45(1200±10)
(L + Ga → Sps + Crd)	39.669(40)	23.623(24)	36.708(36)	1195.40(1190±5)
L → Rh + Tr + Sp	41.617(38)	11.155(13)	47.228(49)	1115.49(1140±10)
L → Rh + Sps + Te	51.22(50)	9.43(11)	39.35(39)	1131.4(1160±10)
L → Te + Sps + Ga	53.638	14.748	31.614	1152.11
L + MnO→ Te + Ga	63.06	12.417	24.523	1231.03
L + Mu→ Sps + Mn-Crd	34.773	21.073	44.154	1170.31
L + Crd → Sps + Mu	38.897	23.555	37.548	1193.57
(L + Crd → Sps + Mn-Crd)	(33)	(24)	(43)	(1162±5)
(L + Mu → Crd + Mn-Crd)	(32)	(25)	(43)	(1168±5)

[1] Abbreviations: Crd: Cordierite, Ga: Galaxite, Mu: Mullite, Rh: Rhodonite, Sps: Spessartite, Te: tephorite, Tr: tridymite.

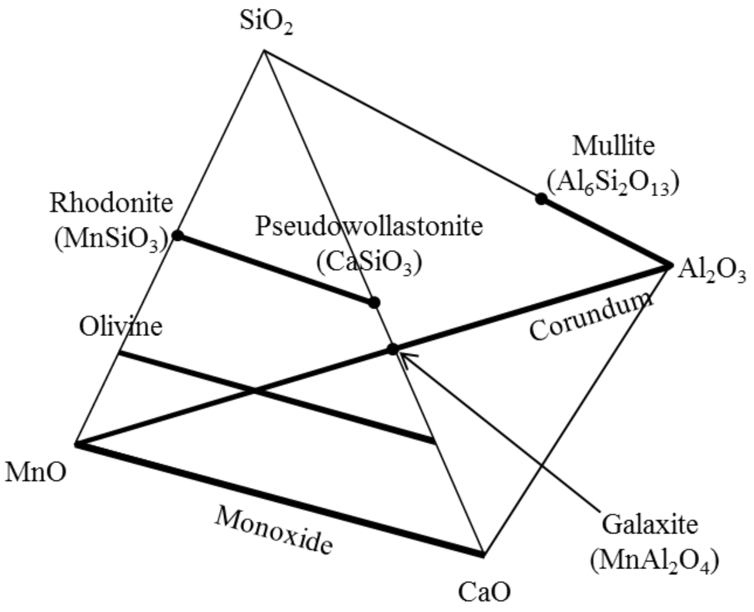

Figure 5.1: Schematic representation of phases in the MnO-Al_2O_3-SiO_2-CaO system under reducing condition.

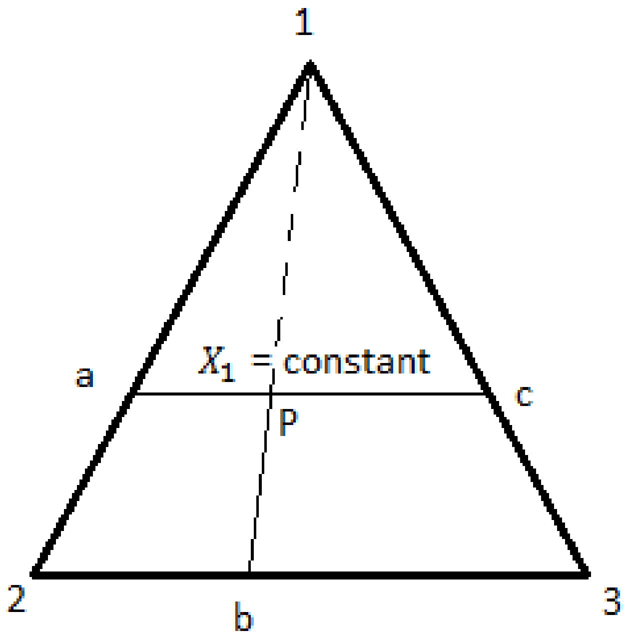

Figure 5.2: Geometric representation of asymmetric Kohler/Toop model (Toop-like model) given by Chartrand and Pelton [2].

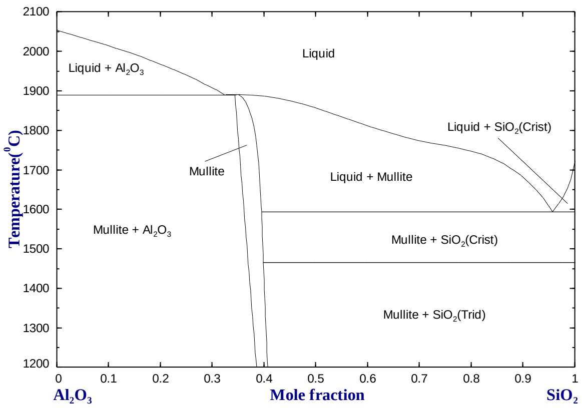

Figure 5.3: Phase Diagram for the Al_2O_3-SiO_2 system [6].

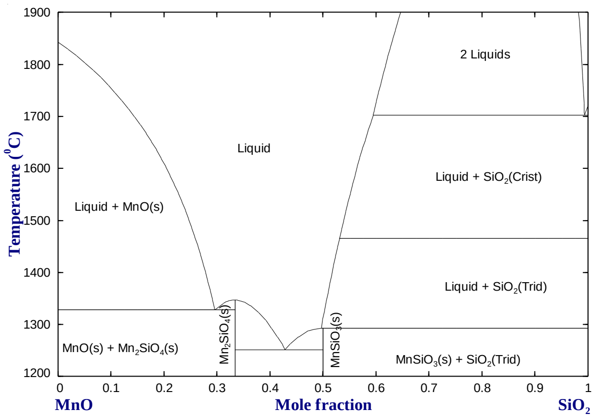

Figure 5.4: Phase Diagram for the MnO-SiO_2 system [7].

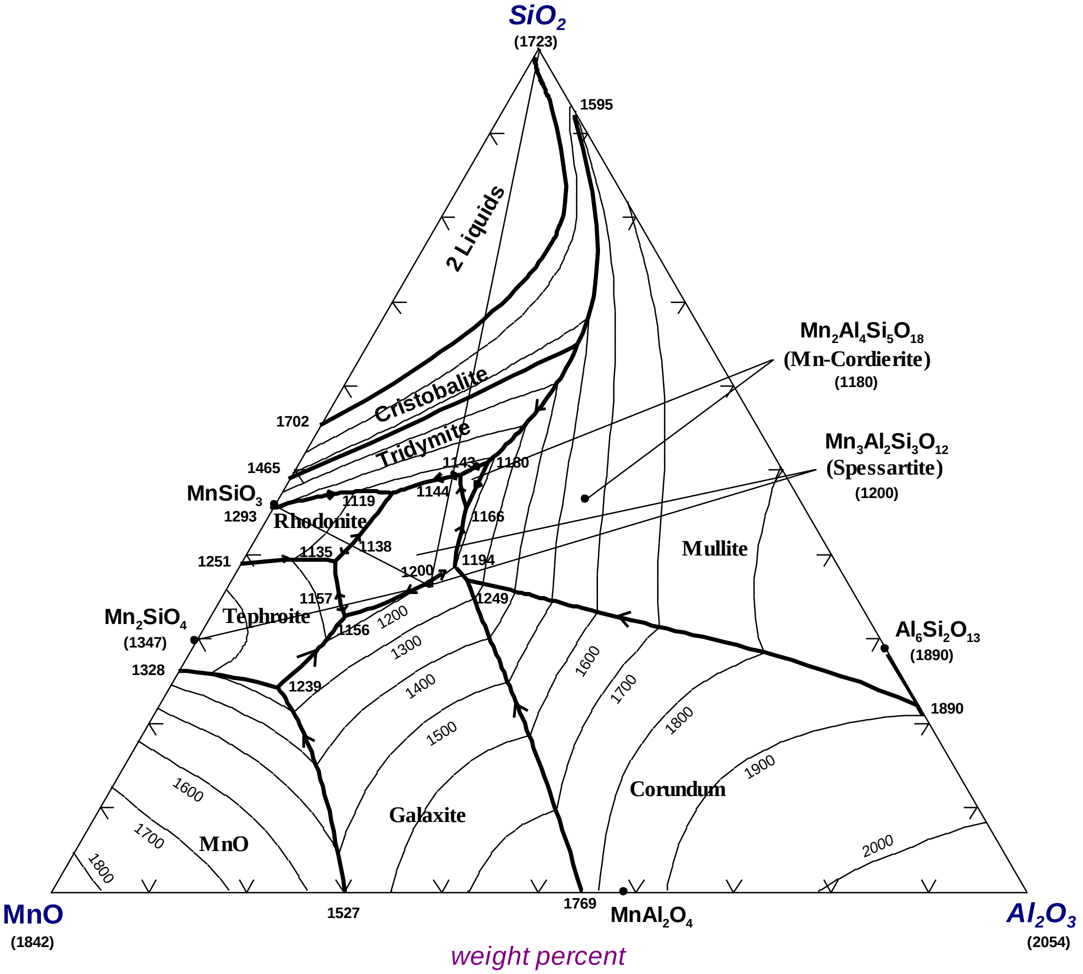

(a)

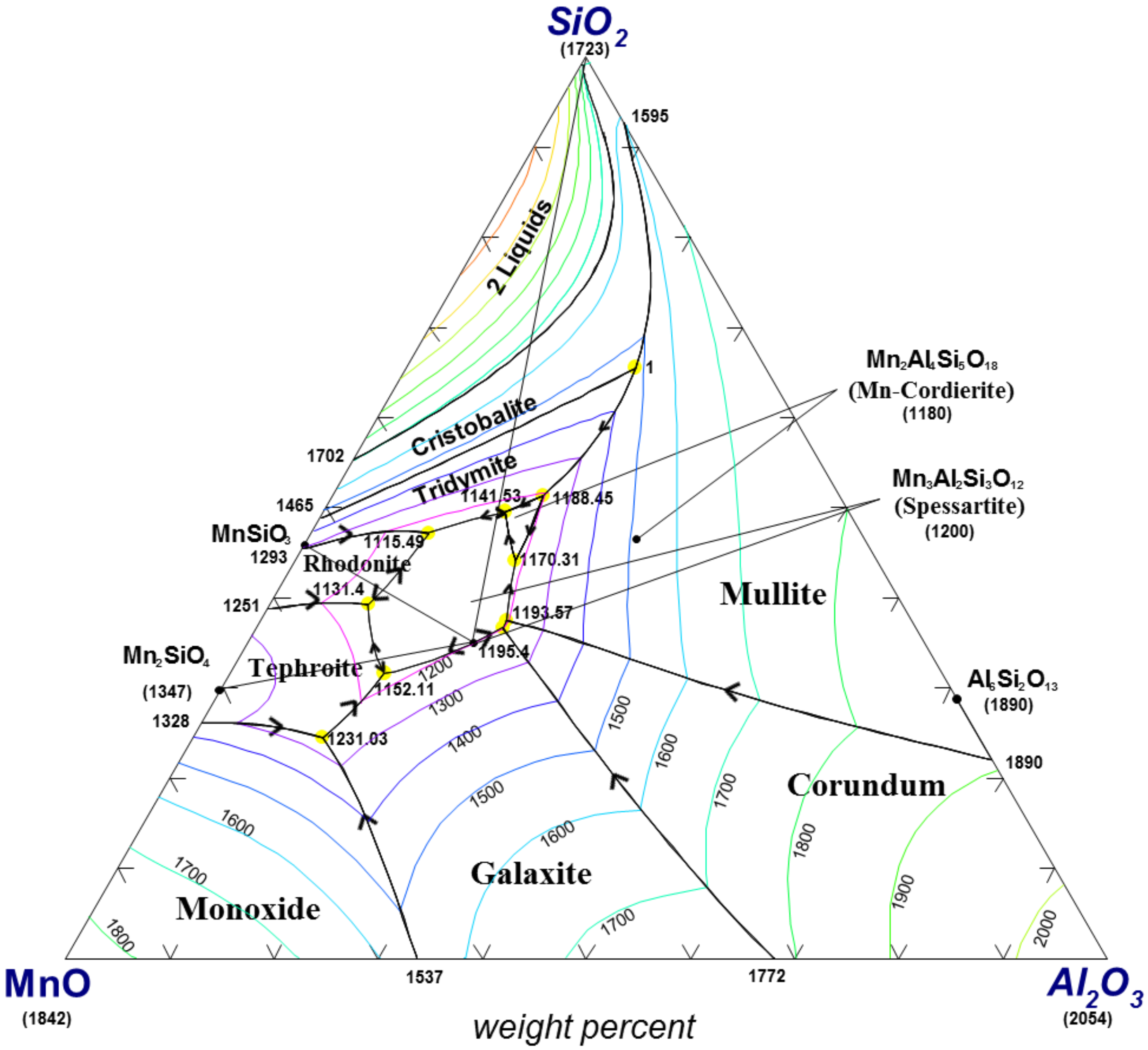

(b)

Figure 5.5: Optimized liquidus surface of the $MnO-Al_2O_3-SiO_2$ system at Fe saturation (Temperatures in ^oC): (a) From Jung *et al.* [5] and (b) Present work

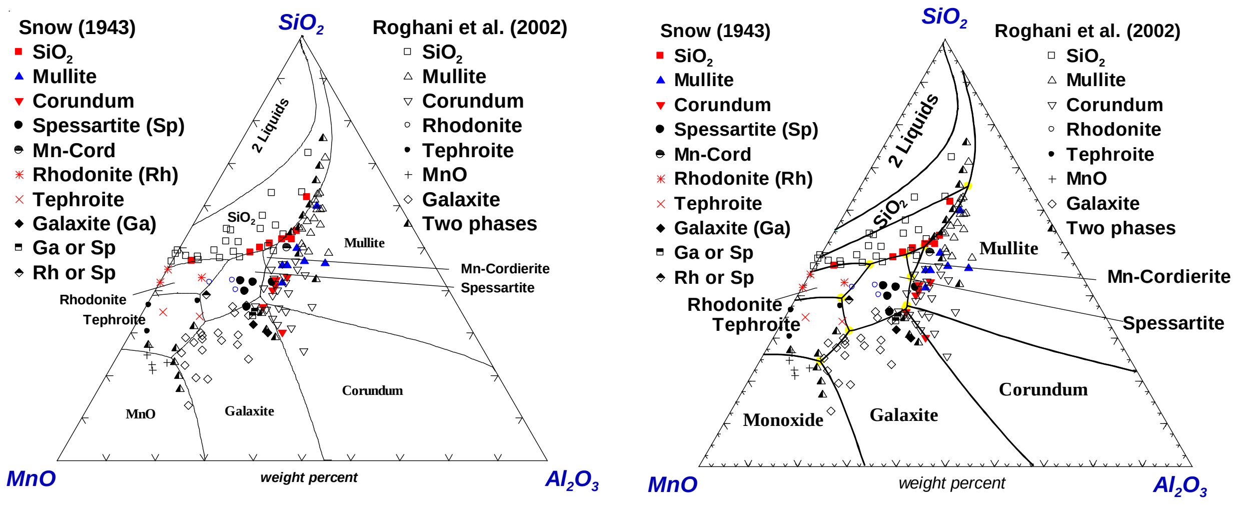

(a) (b)

Figure 5.6: Optimized primary phase fields of the MnO-Al$_2$O$_3$-SiO$_2$ system at Fe saturation along with the experimental points by Snow [4] and Roghani *et al.* [8]: (a) From Jung *et al.* [5] and (b) Present work.

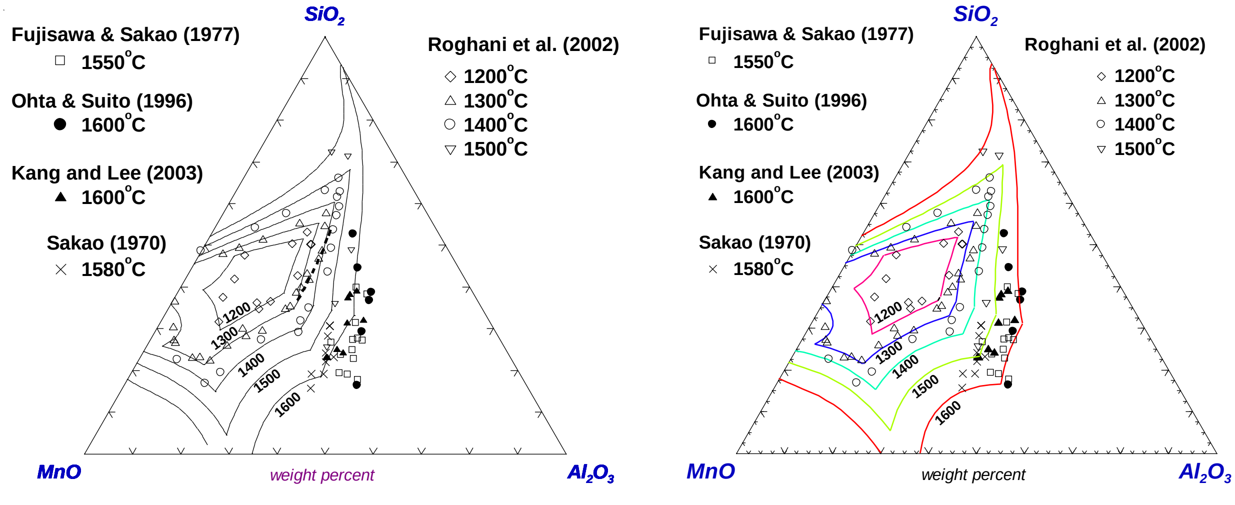

(a) (b)

Figure 5.7: Calculated liquidus surface of the MnO-Al$_2$O$_3$-SiO$_2$ system at temperatures between 1200 and 1600^{o}C compared with experimental data by Sakao [17], Fujisawa and Sakao [18], Ohta and Suito [19], Roghani *et al.* [8] and Kang and Lee [20]: (a) From Jung *et al.* [5] and (b) Present work.

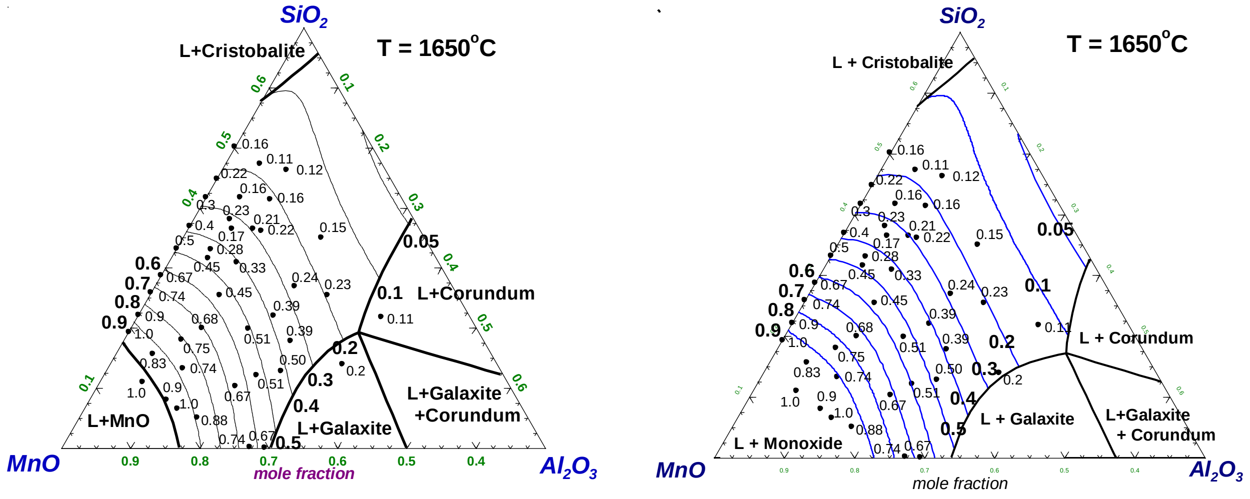

(a) (b)

(i) at 1650°C with experimental data from Sharma and Richardson [9].

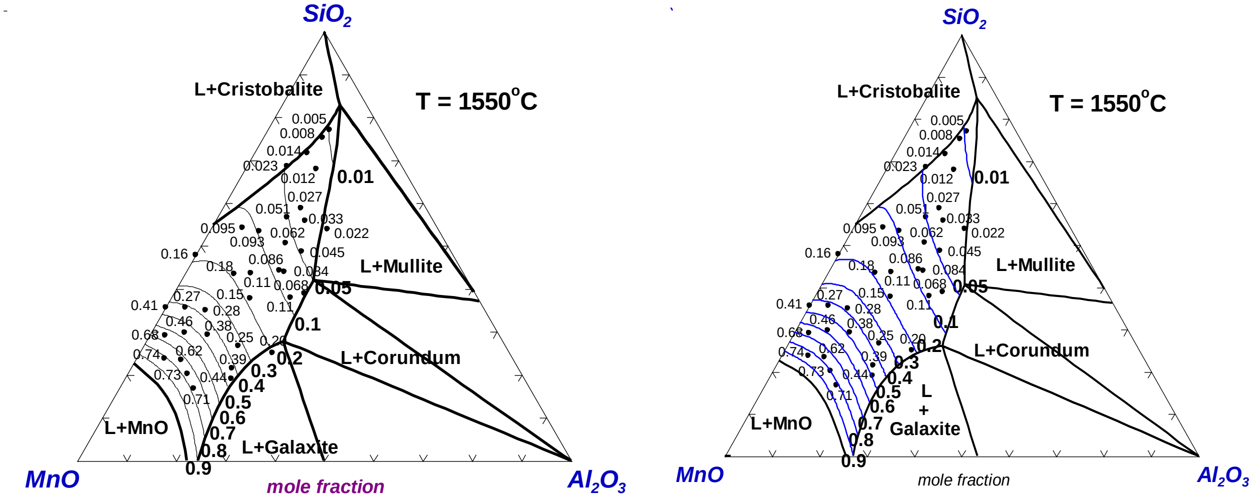

(a) (b)

(ii) at 1550°C with experimental data from Woo *et al.* [10].

Figure 5.8 (i) and (ii): Calculated activities of MnO (solid standard state) in MnO-Al_2O_3-SiO_2 slag: (a) From Jung *et al.* [5] and (b) Present work.

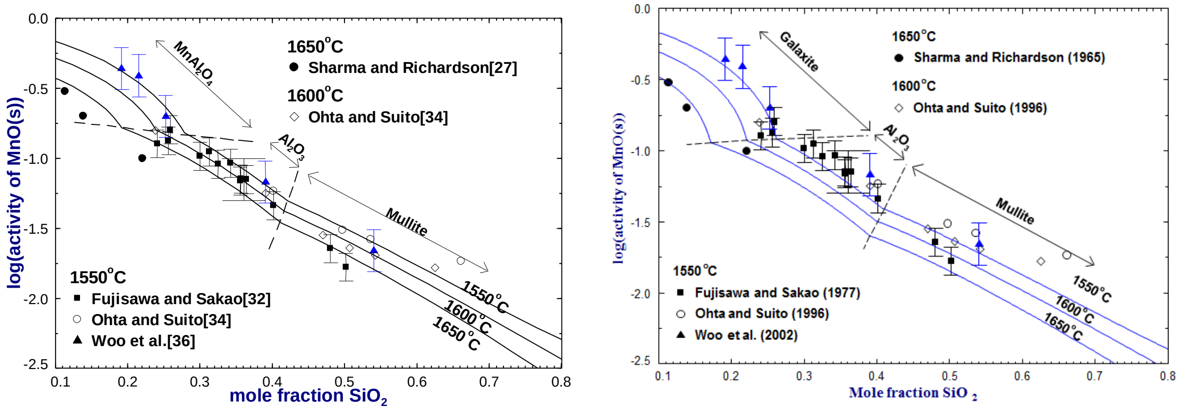

(a) (b)

Figure 5.9: Calculated activities of MnO (solid standard state) in MnO-Al_2O_3-SiO_2 liquids at 1550, 1600 and 1650°C at saturation with solid $MnAl_2O_4$, Al_2O_3 or mullite along with the experimental points by Sharma and Richardson [9], Fujisawa and Sakao [18], Ohta and Suito [19] and Woo *et al.* [10]: (a) From Jung *et al.* [5] and (b) Present work.

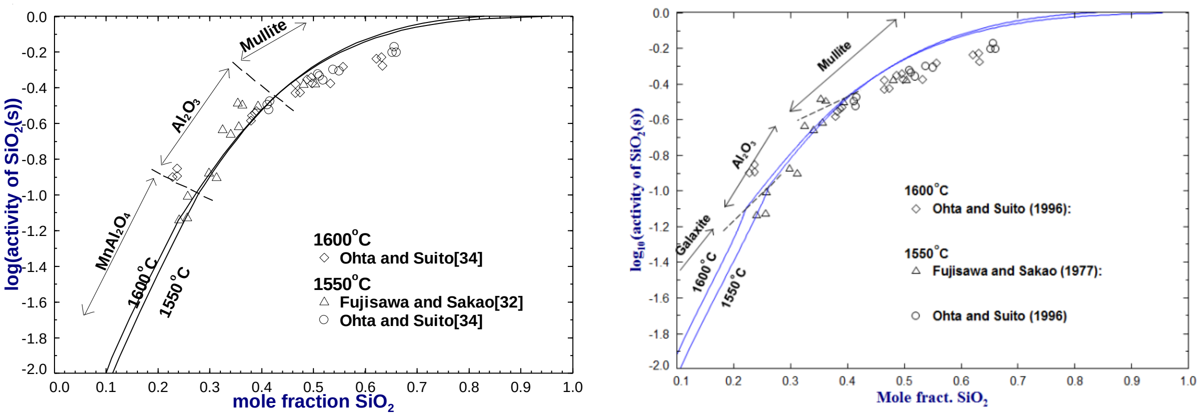

(a) (b)

Figure 5.10: Calculated activities of SiO_2 (solid cristobalite standard state) in MnO-Al_2O_3-SiO_2 slags at 1550 and 1600°C at saturation with solid $MnAl_2O_4$, Al_2O_3 or mullite along with the experimental points by Fujisawa and Sakao [18] and Ohta and Suito [19]: (a) From Jung *et al.* [5] and (b) Present work.

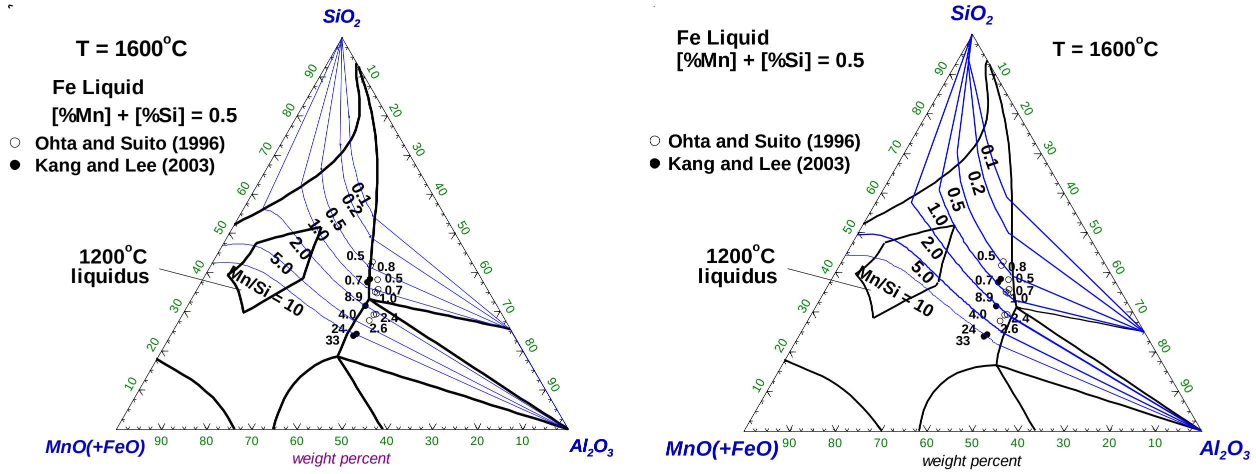

(a) (b)

(i) total dissolved (Mn + Si) contents of 0.5

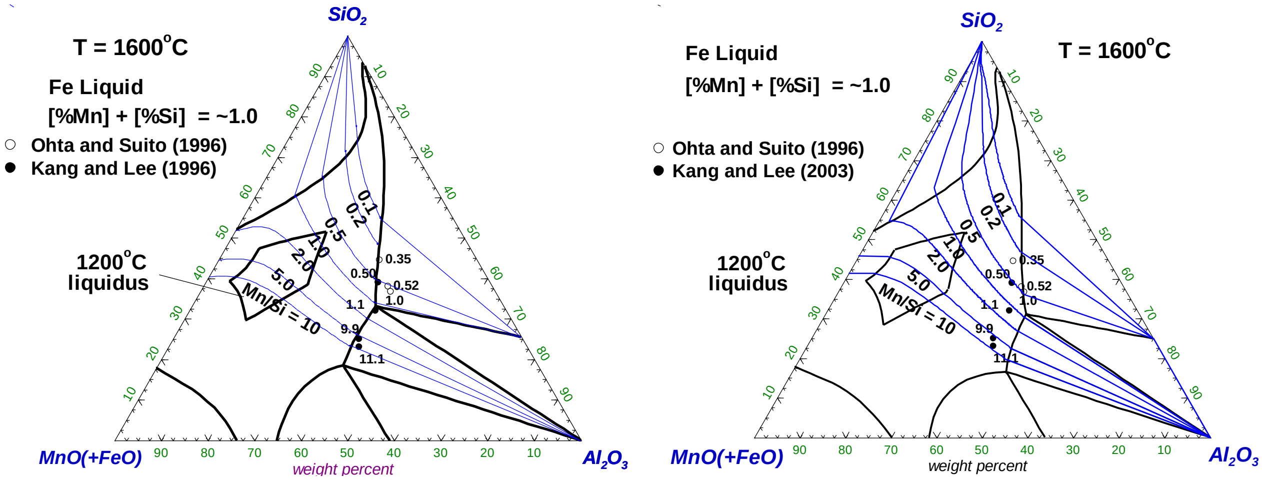

(a) (b)

(ii) total dissolved (Mn + Si) contents of 1.0

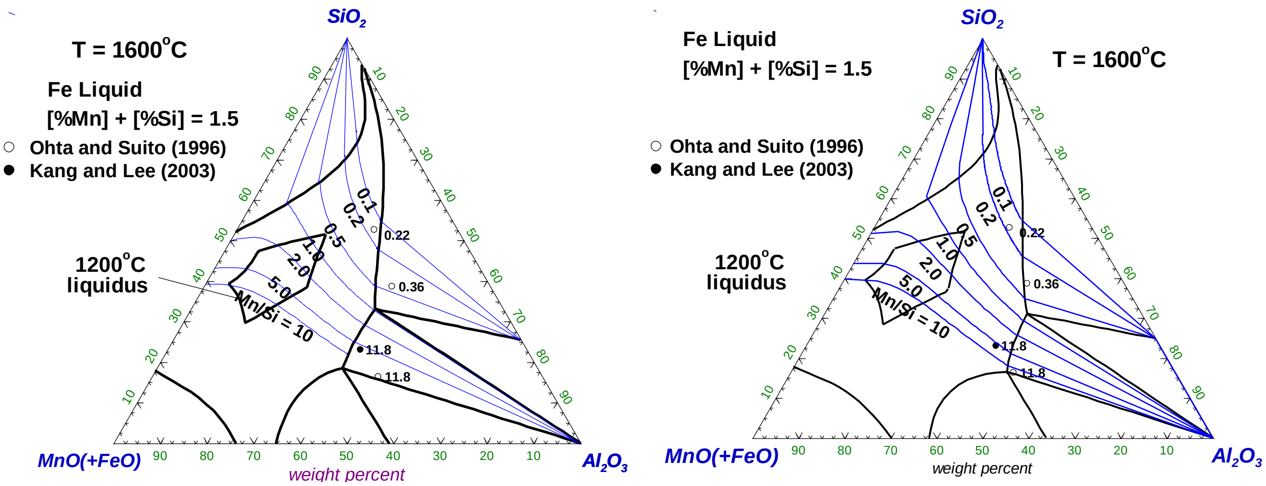

(a) (b)

(iii) total dissolved (Mn + Si) contents of 1.5

Figure 5.11 (i), (ii) and (iii): Calculated compositional trajectories of MnO-Al$_2$O$_3$-SiO$_2$ inclusions in equilibrium with liquid Fe containing various Mn/Si weight ratios at 1600°C. Experimental Mn/Si ratios at Al$_2$O$_3$ or mullite saturation are shown beside all experimental points which are obtained from Ohta and Suito [19] and Kang and Lee [20]. The calculated liquidus curves at 1600 and 1200°C are also shown. All calculations are: (a) From Jung *et al.* [5] and (b) Present work.

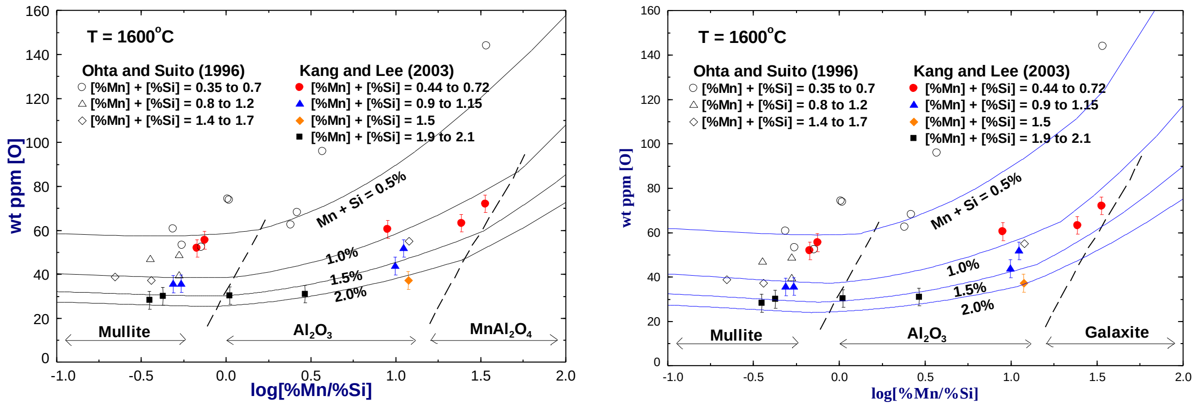

(a) (b)

(i) at 1600°C

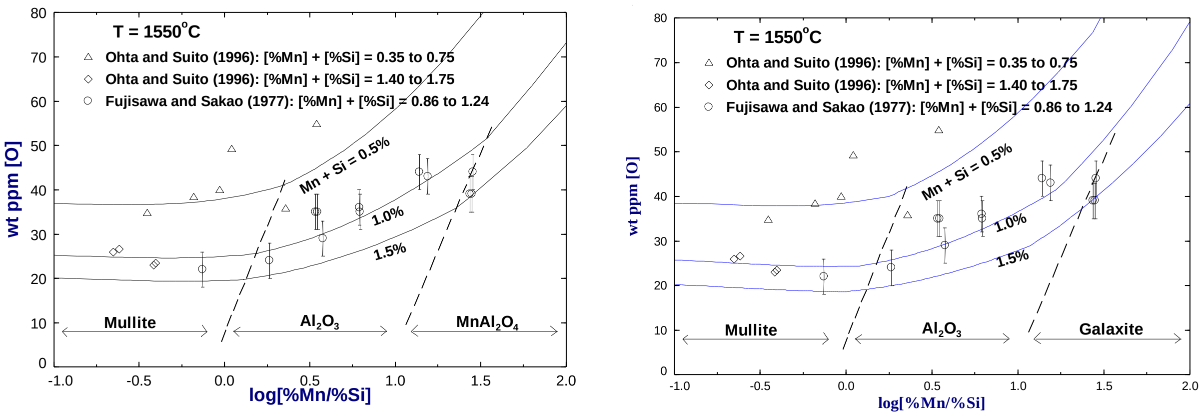

(a)

(b)

(ii) at 1550°C

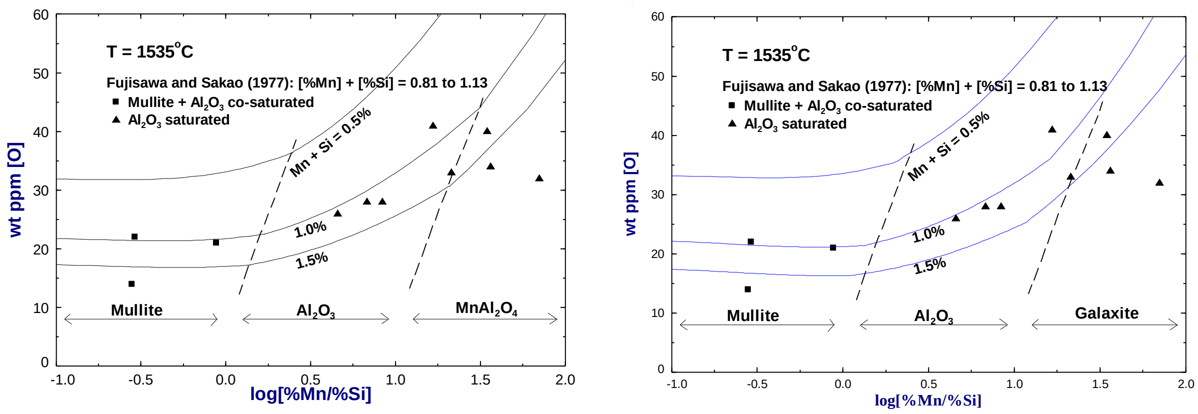

(a)

(b)

(iii) at 1535°C

Figure 5.12 (i), (ii) and (iii): Calculated oxygen content versus dissolved Mn/Si weight ratio at various total dissolved (Mn + Si) contents in liquid Fe in equilibrium with liquid $MnO-Al_2O_3-SiO_2$ inclusions saturated with $MnAl_2O_4$, Al_2O_3 or mullite at different temperatures. Experimental points are obtained from Fujisawa and Sakao [18], Ohta and Suito [19] and Kang and Lee [20]. All calculations are: (a) From Jung *et al.* [5] and (b) Present work.

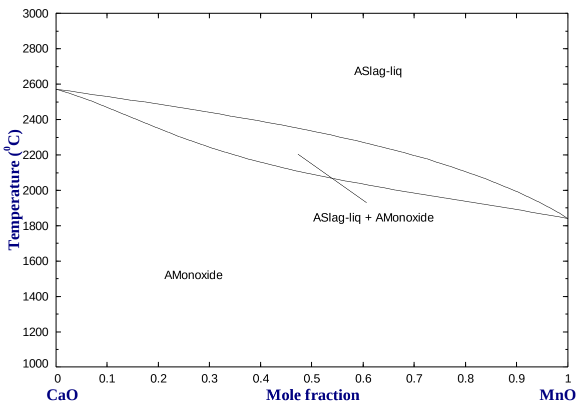

Figure 5.13: Phase Diagram for the CaO-MnO system [11].

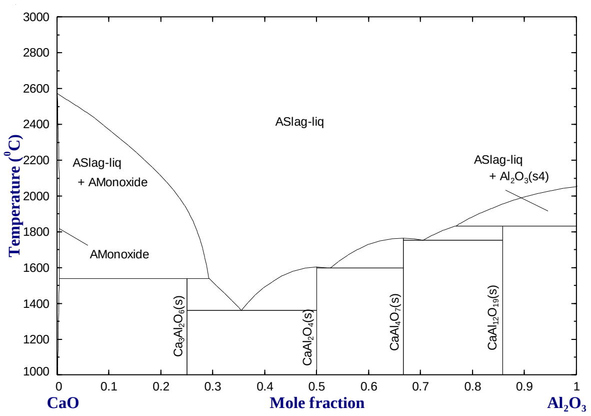

Figure 5.14: Phase Diagram for the CaO-Al_2O_3 system [6].

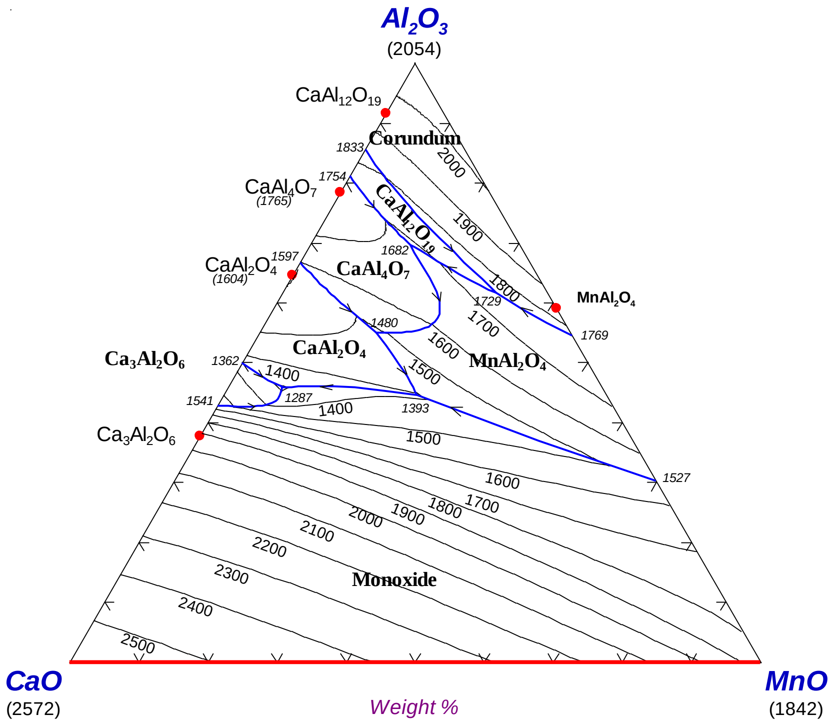

(a)

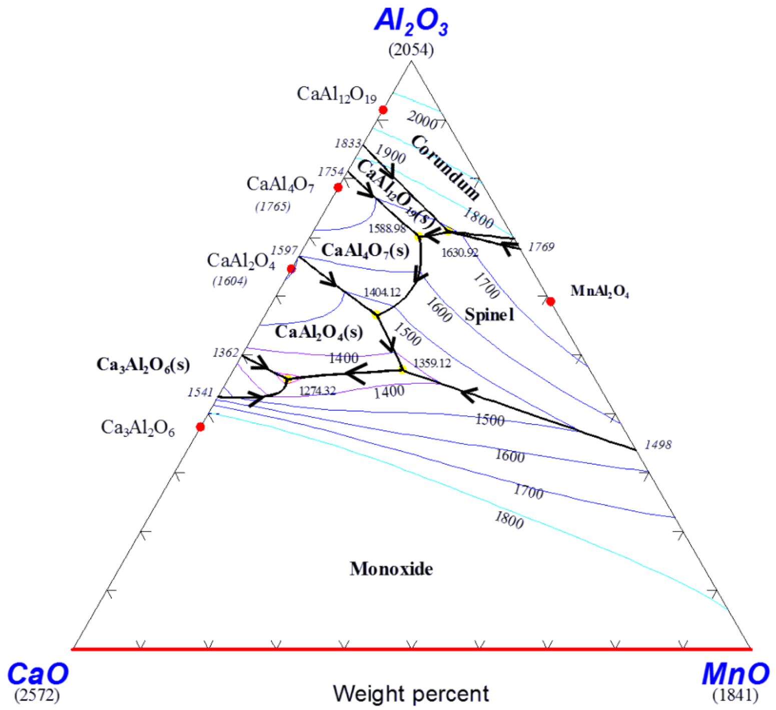

(b)

Figure 5.15: Calculated liquidus projection of the CaO-MnO-Al_2O_3 system: (a) From Kang *et al.* [12] and (b) Present work.

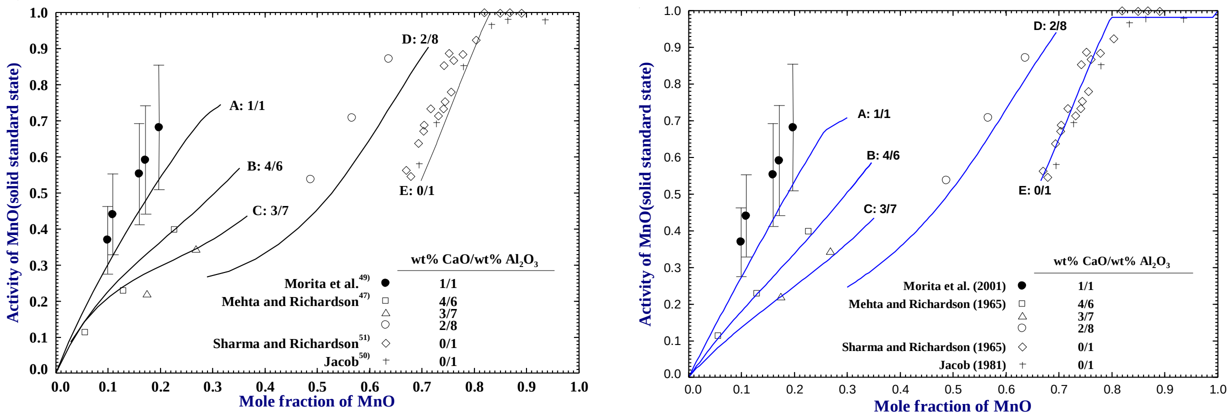

(a) (b)

Figure 5.16: Calculated activities of MnO (solid standard state) in CaO-MnO-Al_2O_3 liquid solutions for different ratios of wt.% CaO / wt.%Al_2O_3. Calculated line A and data from Morita *et al.* represent the activity of MnO at 1600°C while others are at 1650°C. The experimental points are from Mehta and Richardson [25], Sharma and Richardson [9], Jacob [21] and Morita *et al.* [22]. All calculations are: (a) From Kang *et al.* [12] and (b) Present work.

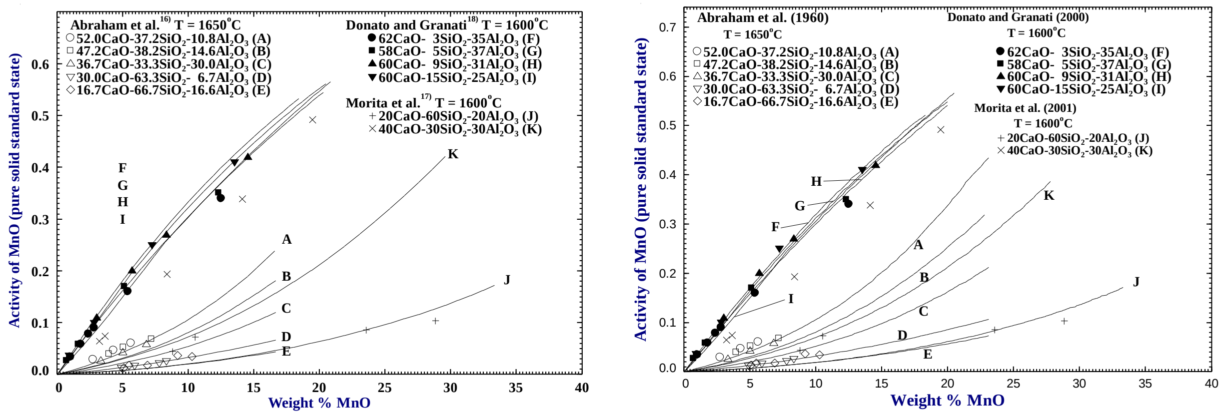

(a)

(b)

Figure 5.17: Calculated activities of MnO (with respect to the pure solid standard state) in CaO-MnO-SiO_2-Al_2O_3 liquid slags along with experimental points from Abraham *et al.* [23], Donato and Granati [24] and Morita *et al.* [22]: (a) From Kang *et al.* [12] and (b) Present work.

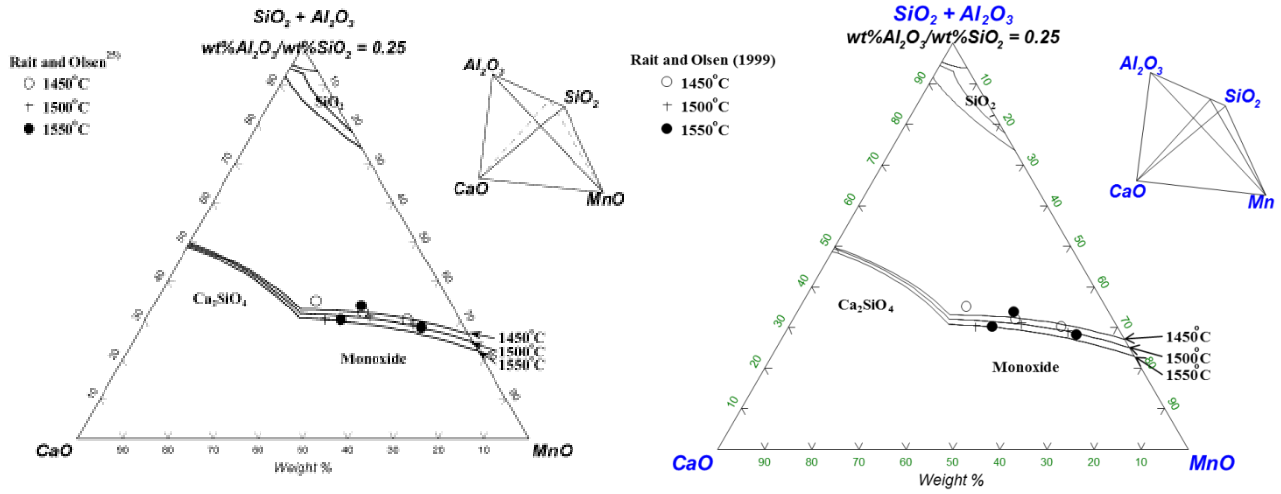

(a)

(b)

(i) at Al_2O_3/SiO_2 weight ratios of (a) 0.25

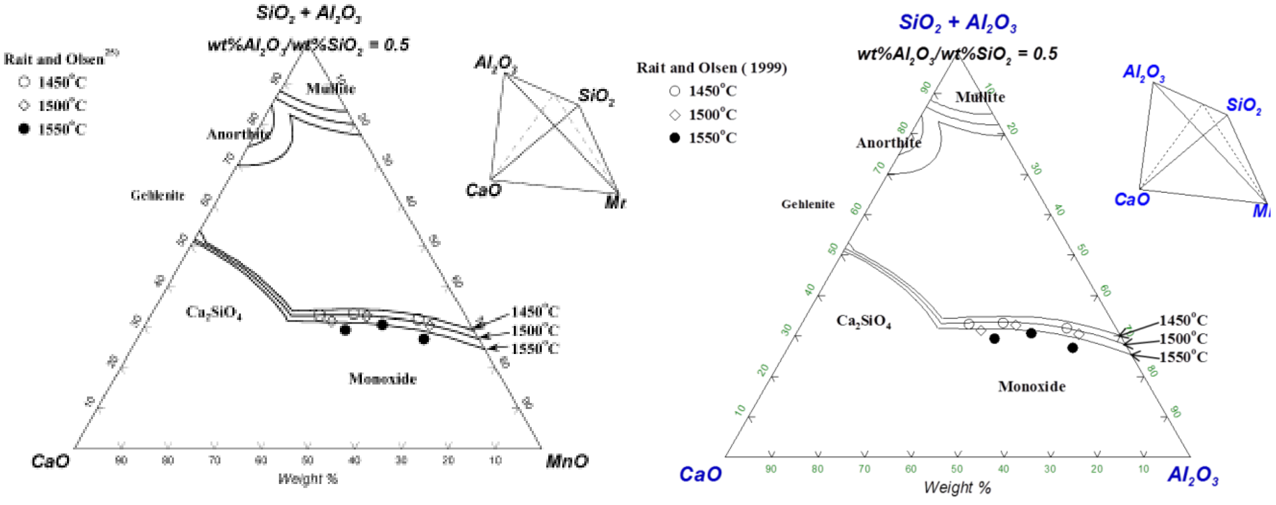

(a) (b)

(ii) at Al_2O_3/SiO_2 weight ratios of (a) 0. 5

Figure 5.18 (i) and (ii): Calculated liquidus surfaces of the CaO-MnO-SiO_2-Al_2O_3 system at 1450°C, 1500°C and 1550°C along with experimental points from Rait and Olsen [13]: (a) From Kang *et al.* [12] and (b) Present work.

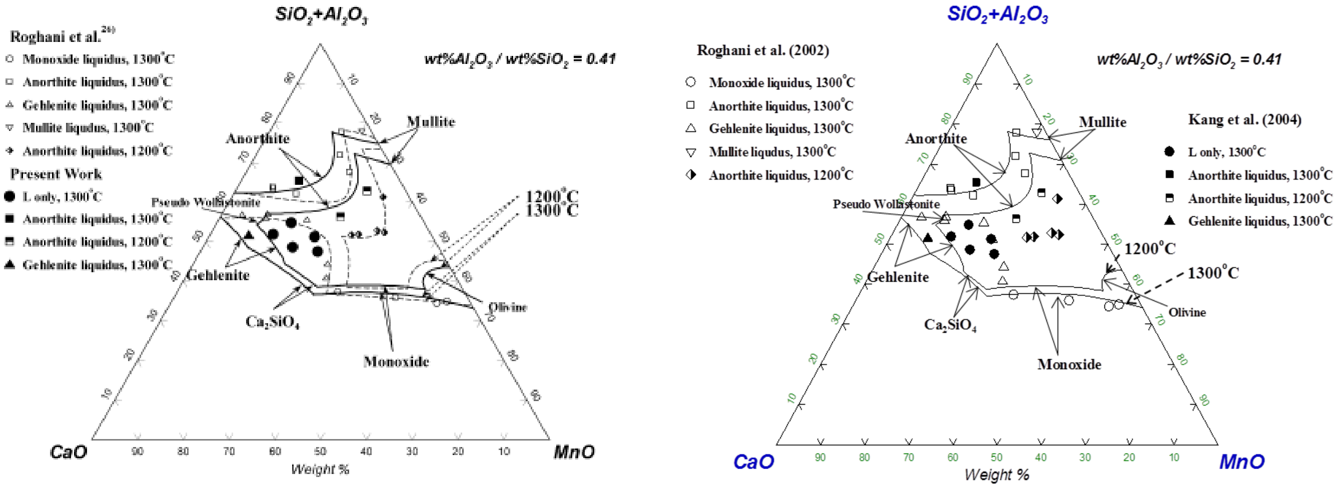

(a) (b)

Figure 5.19: Calculated liquidus surfaces of the CaO-MnO-SiO_2-Al_2O_3 system at an Al_2O_3/SiO_2 weight ratio of 0.41 at 1200°C and 1300°C along with experimental points from Roghani *et al.* [14] and Kang *et al.* [15]: (a) From Kang *et al.* [12] and (b) Present work.

Chapter 6

Thermodynamic modeling of the MnO-Mn_2O_3-Al_2O_3-FeO-MgO system

6.1 Introduction

The amount of experimental data available in the present system is quite high. Since, MnO-Al_2O_3 binary system has been optimized properly now (as can be seen in chapter 4), the accuracy of the predictions for the higher order systems can be judged by comparing them with the available experimental data. The results for the MnO-Mn_2O_3-Al_2O_3-CaO-SiO_2 system have been compared with experimental data in chapter 5 and it was observed that the predictions are in good agreement with the experimental data. Similar to the previous system (chapter 5), we have not used any interaction parameter in the present system while performing our calculations.

6.2 Critical evaluation and optimization

6.2.1 FeO-MnO-Mn_2O_3-Al_2O_3

The FeO-MnO-Al_2O_3 ternary system consists of three binary subsystems:

a. Fe-Mn-O system: The thermodynamic optimization of this system has already been done by Wu *et al.* [1].
b. Fe-Al-O system: The thermodynamic optimization of this system has already been done by Eriksson *et al.* [2].
c. Mn-Al-O system: The thermodynamic optimization of this system has already been shown in chapter 4.

Fig. 6.1 and 6.2 show the calculated phase diagrams of the FeO-MnO and FeO-Al_2O_3 binary systems from the optimized model parameters stored in FToxide database [3]. All experimental data related to phase diagrams, cation distribution and thermodynamic properties were considered in the modeling. All the previous model parameters were used in the present study without any modification.

The maximum mole fraction of Mn_2O_3 in the FeO-MnO-Mn_2O_3-Al_2O_3 slag phase at 1600°C is as low as 0.0015 which is quite low.

The schematic diagram of the Fe-Mn-Al-O (FeO-MnO-Mn_2O_3-Al_2O_3) system under reducing condition is shown in Fig. 6.3. The following solution phases are found in the Fe-Mn-Al-O system:

Spinel: $(Mn^{2+}, Fe^{2+}, Al^{3+})^{T}(Al^{3+}, Mn^{2+}, Fe^{2+}, Mn^{3+}, Mn^{4+}, Va)^{O}_{2}O_4$
Bixbyite: $(Mn^{2+}, Al^{3+}, Fe^{3+})_2O_3$
Corundum: $(Al^{3+}, Mn^{2+}, Fe^{3+})_2O_3$
Slag (molten oxide phase): FeO-MnO-$MnO_{1.5}$-$AlO_{1.5}$
Monoxide: FeO-MnO-$MnO_{1.5}$-$AlO_{1.5}$

No change has been made to the parameters related to any of the solid solutions present in the FeO-MnO-Mn_2O_3-Al_2O_3 system; all the required parameters have been obtained from the FToxid database of FactSage 6.3 software [3].

Fig. 6.4 shows the optimized liquidus surface of the FeO-MnO-Al_2O_3 system under reduced oxygen condition (Fe saturation). The Gibbs energy of the ternary liquid surface was calculated with the help of the Modified Quasichemical model using the “asymmetric approximation (Toop-like interpolation technique)” by Chartrand and Pelton [4], Pelton [5] along with the parameters of the binary subsystems. In the present asymmetric approximation, Al_2O_3 was considered as the asymmetric component and FeO and MnO as the symmetric components. No additional ternary parameters were considered.

Hay *et al.* [6] were the first to carry out experiments to determine the phase relations in the FeO-MnO-Al_2O_3 system. They constructed the thermal diagram for the FeO-MnO-Al_2O_3 ternary system using the data from the heating, cooling curves and microscopical evidences. The partial pressure of oxygen was strictly reducing allowing no oxidation of samples. No measurement was done for mixtures exceeding 40% Al_2O_3 because of the very high temperatures required. They also constructed a diagram showing the projection of the liquidus surface. Oelsen and Heynert [7] prepared oxide samples saturated with metal and carried out equilibration experiments by placing them in Al_2O_3 crucibles. All the experiments were done by heating the samples to either 1550, 1600 or 1650°C. Analyses were done of all the samples after quenching and this allowed them to obtain liquidus measurements in the FeO-MnO-Al_2O_3 system. Fischer and Bardenheuer [8] carried out similar experiments by equilibrating FeO-MnO-Al_2O_3 slags on FeO-MnO solid solution in sintered MnO crucibles. They carried out all their experiments in the temperature range of 1530-1700°C. The amounts of dissolved Oxygen and Manganese contents in liquid Iron along with amounts of FeO, MnO, etc. in slag were analyzed. Later, Maruhashi [9] and Ivanchev and Erinin [10] also carried out similar slag-metal equilibration experiments.

The experimental points in the Mn-O plot (Fig. 6.5) seem to follow a specific trend. The amount of dissolved O decreases slowly with increasing amounts of dissolved Mn till a certain point, after which the amount of O starts to decrease rapidly. The calculated results follow the trend and seem to trace the exact path of the experimental points.

Fig. 6.6 and 6.7 show the variation of dissolved O amount along with the variation of MnO and FeO levels in slag. The calculated amount of dissolved O at low MnO and high FeO levels in slag doesn’t seem to be as high as the experimental data. Those few experimental results could not be reproduced along with the set of data shown in Fig. 6.5. However, the trend observed in our calculations is similar to those of the experimental data. The agreement between the calculated and the experimental data improves at high MnO and low FeO levels in the slag.

Fig. 6.8 shows the effect of Mn present in molten iron on the amount of MnO in the slag. The amount of MnO in the slag increases very rapidly and reaches a plateau with initial rise in the amount of Mn in the molten iron. Its amount no more increases after a certain amount even when the Mn levels are kept n increasing. Our calculated results are in excellent agreement with the observed trend of the experimental results as shown in the Fig. 6.8.

Fischer and Bardenheuer [8] carried out their experiments under FeO-MnO solid solution saturation and the variations of dissolved O and Mn along with amount of FeO in slag have been depicted in Fig. 6.9 and 6.10. Our calculated results are in excellent agreement with the findings of Fischer and Bardenheuer [8].

Fischer and Bardenheuer [8], Maruhashi [9] and Ivanchev and Erinin [10] also calculated the activities of the components of the slag (like FeO, MnO) from the measured amounts of dissolved oxygen and manganese in the liquid iron.

Fig. 6.11 to 6.13 show that the calculated activities of FeO in slag are close enough to the experimentally determined activities.

Kim and McLean [11] carried out experiments in which they equilibrated iron containing different amounts of oxygen, manganese, etc. with Al_2O_3. This resulted in the formation of aluminate solid solutions. They could obtain the activities of the components in the spinel solution from dissolved amounts of O and Mn in liquid iron (found out by chemical analyses) and composition of the deoxidation product (obtained by EPMA and Neutron analyses). Pandit and Jacob [12] also carried out equilibration experiments similar to Kim and McLean [11] and obtained similar results.

Fig. 6.14 and 6.15 show the variation of dissolved O and $MnAl_2O_4$ content of spinel solution along with increase of dissolved Mn content of the alloy respectively. Calculations were done with different amounts of Alumina since the exact amount of Alumina that was reacting was difficult to understand. It can be observed that the amount of dissolved O in the alloy decreases with increasing amounts of Alumina. This is because the amount of spinel formed starts to increase with increasing amounts of Alumina. So, O can no more get dissolved in the alloy as it is used up in formation of spinel. Moreover, the results in Fig. 6.15 show that amount of galaxite component in the spinel solution increases with increasing amounts of Alumina suggesting that Alumina is used up in formation of more and more of galaxite and not hercynite.

The calculated activities of the components of the spinel solid solution are in excellent agreement with the experimental results as shown in Fig. 6.16.

Fig. 6.17 shows the predicted cation distribution in the Galaxite-Hercynite spinel solid solution at 900°C. This is an example of how the optimized parameters can be used along with the software Factsage [3] to predict the phase relationships or thermodynamic property of a system at any given condition. These types of thermodynamically correct predictions are of immense help at times when there is no experimental data available.

6.2.2 MgO-MnO-Mn_2O_3-Al_2O_3

The MgO-MnO-Al_2O_3 ternary system consists of three binary subsystems:

a. Mg-Mn-O system: The thermodynamic optimization of this system has already been done by Wu *et al.* [1].
b. Mg-Al-O system: The thermodynamic optimization of this system has already been done by Jung *et al.* [13].
c. Mn-Al-O system: The thermodynamic optimization of this system has already been discussed in chapter 4.

Fig. 6.18 and 6.19 show the calculated phase diagrams of the MgO-MnO and MgO-Al_2O_3 binary systems from the optimized model parameters stored in FToxide database. All experimental data related to phase diagrams and thermodynamic properties were considered in the modeling. All the previous model parameters were used in the present study without any modification.

The maximum mole fraction of Mn_2O_3 in the MgO-MnO-Mn_2O_3-Al_2O_3 slag phase at 1600°C is as around 0.001 which is very low.

The schematic diagram of the Mg-Mn-Al-O (MgO-MnO-Mn_2O_3-Al_2O_3) system under reducing condition is shown in Fig. 6.20. The following solution phases are found in the Mg-Mn-Al-O system:

Spinel: $(Mn^{2+}, Mg^{2+}, Al^{3+})^{T}(Al^{3+}, Mg^{2+}, Mn^{2+}, Mn^{3+}, Mn^{4+}, Va)_2^{O}O_4$
Bixbyite: $(Mn^{2+}, Al^{3+}, Mg^{2+},)_2O_3$
Corundum: $(Al^{3+}, Mn^{2+}, Mg^{2+})_2O_3$
Slag (molten oxide phase): $MgO\text{-}MnO\text{-}MnO_{1.5}\text{-}AlO_{1.5}$
Monoxide: $MgO\text{-}MnO\text{-}MnO_{1.5}\text{-}AlO_{1.5}$

No change has been made to the parameters related to any of the solid solutions present in the $MgO\text{-}MnO\text{-}Al_2O_3$ system; all the required parameters have been obtained from the FToxid database of FactSage 6.3 software [3].

The Gibbs energy of the ternary liquid surface was calculated with the help of the Modified Quasichemical model using the “asymmetric approximation (Toop-like interpolation technique)” by Chartrand and Pelton [4], Pelton [5] along with the parameters of the binary subsystems. In the present asymmetric approximation, Al_2O_3 was considered as the asymmetric component and MgO and MnO as the symmetric components. No additional ternary parameters were considered.

The experimental data in the system have been mainly obtained by the equilibration of the slag and spinel solution with liquid iron. Balakirev *et al.* [14] carried out experiments to expose the presence of spinel phases of the system in the temperature ranging between 900 and 1200°C in air. They used Mn_2O_3, MgO, $Al(OH)_3$ as the staring materials for their experiments. The prepared cylindrical samples were annealed at 900, 1000, 1100 and 1200°C followed by quenching in water. Annealing was done for 100-300 hours to ensure equilibration, i.e., achievement of phase equilibrium and equilibrium cation distribution. However, X-ray data showed that equilibrium was reached within 30-50 hours of heat treatment.

They carried out XRD studies on all the samples to obtain the c/a ratios, from where they could predict the phase/phases present in that specific sample. They used all the c/a ratio measurements in order to construct phase stability regions since the initial composition of the samples were known. Their predicted phase diagrams focussed mainly on the spinel part of the Mg-Mn-Al-O system after quenching. Hence, one may acquire the knowledge of the stability of the phases present at temperatures between 900 and 1200°C from this study. However, the phase diagram data from this work was mainly restricted to the spinel phases and according to our evaluation it was not possible to perform any calculations related to phase diagram based on this scarce data.

The Fig. 6.21 shows the calculated activities of the components of the $MnAl_2O_4$- $MgAl_2O_4$ spinel solid solution along with the experimental data. Zhao *et al.* [15] equilibrated mixtures of $MnAl_2O_4$ and Al_2O_3 using molten Ag-Mn solutions. They obtained the Gibbs energy of formation of $MnAl_2O_4$ by making use of some data from previous literature in a manner already discussed in section **4.3.1.2**. Then, the activity of $MnAl_2O_4$ in a solid solution of $MnAl_2O_4$-$MgAl_2O_4$ was calculated by Zhao *et al.* [15] from knowledge of Gibbs energy, temperature, activity coefficient and mole fraction of Mn in solid solution and partial pressure of O_2. The activity of $MgAl_2O_4$ could, then, be calculated using the Gibbs-Duhem equation. Zhao *et al.* [15] carried out many equilibration experiments to determine the activity-composition relations in the MnO-MgO-Al_2O_3 solid solutions at 1550 and 1600°C. However, we have used the newly evaluated data related to Gibbs energy of formation of $MnAl_2O_4$ in order to increase the accuracy of thermodynamic modeling. The comparison of the experimental data with the calculated data shows that the two sets of data follow the same trend.

The Fig. 6.22 shows the calculated distribution of cations in the tetrahedral and octahedral sites of the spinel solution as a function of the composition of components of the $MnAl_2O_4$-$MgAl_2O_4$ spinel solid solution along with the experimental data.

Halenius [16] prepared single crystals of the type $(Mg_{1-x}Mn_x)Al_2O_4$ in a flux-growth method. The partial pressure of Oxygen was maintained in the range of 10^{-12} to 10^{-17} bars during the preparation of the samples. The samples were heated at first to 1200°C where they were kept for 24 hours for complete homogenization. Then, they were cooled to 900°C at the rate of 4°C/min, followed by fast cooling to room temperature. EPMA of the products gave their composition. Then, single crystal structural refinements were performed in which cation distribution in the products was calculated from an optimization program applying a minimization function in which both structural and chemical data of the products were taken into account.

The calculated results show the same trend as shown by the experimental results.

6.2.3 Other systems at oxidizing condition

There is no experimental data available for any other subsystem in oxidizing condition. Hence, Factsage [3] can be used along with proper database to predict phase relationships in any system at any condition.

6.3 Summary

The previous work in the Mn-Al-O system has been extended to the MnO-Al_2O_3-FeO-MgO system. No change in the model parameters of the ternary systems has been done. All the calculations in the MnO-Al_2O_3-FeO-MgO system have been performed with the newly obtained database. The present results show good agreement with the experimental data. This proves that the optimized model parameters for the binary MnO-Al_2O_3 system are reasonable and they can be extended to even higher order systems.

References

[1] P. Wu, G. Eriksson and A.D. Pelton, “Critical evaluation and optimization of the thermodynamic properties and phase diagrams of the CaO-FeO, CaO-MgO, CaO-MnO, FeO-MgO, FeO-MnO, and MgO-MnO systems,” *J. Am. Ceram. Soc.*, **76[8]**, 2065-2075 (1993).

[2] G. Eriksson, P. Wu and A.D. Pelton, “Critical evaluation and optimization of the thermodynamic properties and phase diagrams of the MgO-Al_2O_3, MnO-Al_2O_3, FeO-Al_2O_3, Na_2O-Al_2O_3, and K_2O-Al_2O_3 systems,” *CALPHAD: Computer Coupling of Phase Diagrams and Thermochemistry*, **17[2]**, 189-205 (1993).

[3] FactSage 6.3, www.factsage.com, Montreal, Canada, 2012.

[4] Patrice Chartrand and Arthur D. Pelton, “On the Choice of “Geometric” Thermodynamic Models,” *Journal of Phase Equilibria*, **21**, 141-147 (2000).

[5] Arthur D. Pelton, “A General “Geometric” Thermodynamic Model for Multicomponent Solutions,” *CALPHAD: Computer Coupling of Phase Diagrams and Thermochemistry*, **25 [2]**, 319-328 (2001).

[6] R. Hay, A. B. MacIntosh, J.R. Rait and J. White, “Slag systems,” *J. West Scot. Iron and Steel Inst.*, **44**, 85-92 (1936).

[7] W. Oelsen and G. Heynert, “The reactions between iron-manganese melts and the melts of their aluminates,” *Arch. Eisenhuttenwes.*, **26**, 567-575 (1955).

[8] W.A. Fischer and P.W. Bardenheuer, “Equilibria between manganese, aluminium and oxygen-containing iron melts and their slags in a manganese oxide crucible at 1530 to 1700°C,” *Arch. Eisenhuttenwes.*, **39[9]**, 637-643 (1968).

[9] S. Maruhashi, “Equilibrium between FeO-MnO-Al_2O_3 slags and molten iron,” *Tetsu-to-Hagané*, **57(6)**, 891-902 (1971).

[10] I. Ivanchev and K. Erinin, “Distribution of manganese and oxygen between slags containing iron (II) oxide, manganese (II) oxide and aluminium oxide and liquid iron at a temperature of 1550°C,” *Metalurgiya (Sofia)*, **30[3]**, 1-4 (1975).

[11] C. K. Kim and A. McLean, “Thermodynamics of iron-manganese aluminate spinel inclusions in steel,” *Metall. Trans. B*, **10B**, 575-584 (1979).

[12] S. S. Pandit and K. T. Jacob, "Spinel deoxidation equilibria in the Fe-Mn-Al-O system - experiment and computation," Steel Research, 58(3), 105-110 (1987).

[13] I-H Jung, S.A. Decterov, and A.D. Pelton "Critical thermodynamic evaluation and optimization of the MgO-Al_2O_3, CaO-MgO-Al_2O_3 and MgO-Al_2O_3-SiO_2," *Journal of Phase Equilibria and Diffusion*, **25[4]**, 329-345 (2004).

[14] V. F. Balakirev, E. G. Kostitsin, V. P. Barkhatov, N. A. Vatolin, "Phase equilibriums of spinels in the magnesium-manganese-aluminium-oxygen system in temperature range 900 to 1200°C," *Materials Science Monographs*, **16[Issue Ceramic Powders]**, 611-620 (1983).

[15] Y. Zhao, K. Morita, and N. Sano, "Thermodynamic Properties of the $MgAl_2O_4$-$MnAl_2O_4$ Spinel Solid Solution," *Metall. Mater. Trans. B*, **26B**, 1013-17 (1995).

[16] U. Halenius, F. Bosi, and H. Skogby, "A first record of strong structural relaxation of TO_4 tetrahedra in a spinel solid solution," *Am. Mineral.*, **96**, 617-622 (2011).

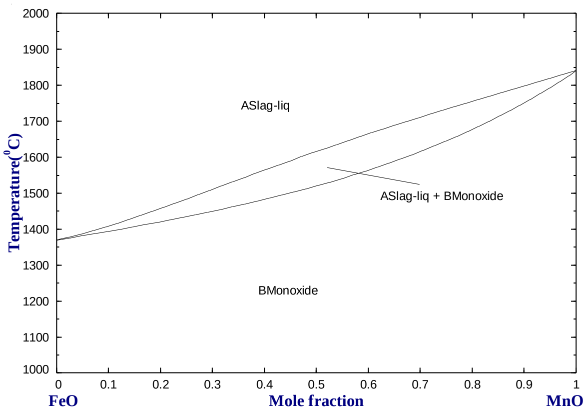

Figure 6.1: Phase Diagram for the FeO-MnO system under reducing condition by Wu *et al.* [1].

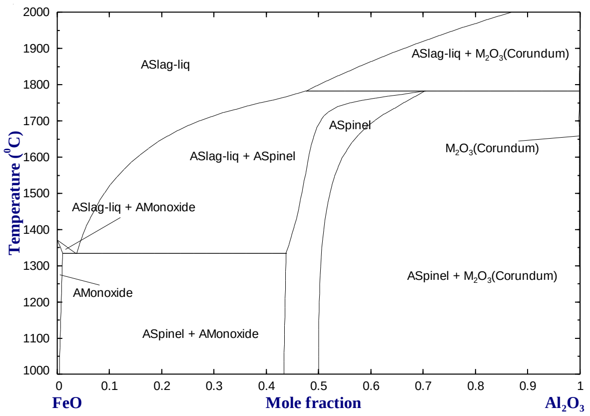

Figure 6.2: Phase Diagram for the FeO-Al_2O_3 system under reducing condition by Eriksson *et al.* [2].

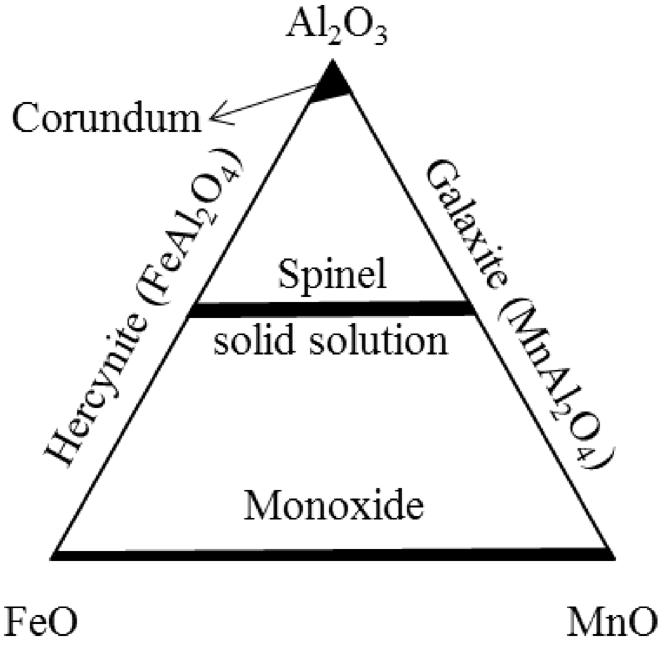

Figure 6.3: Schematic representation of phases in the FeO-MnO-Al_2O_3 system under reducing condition.

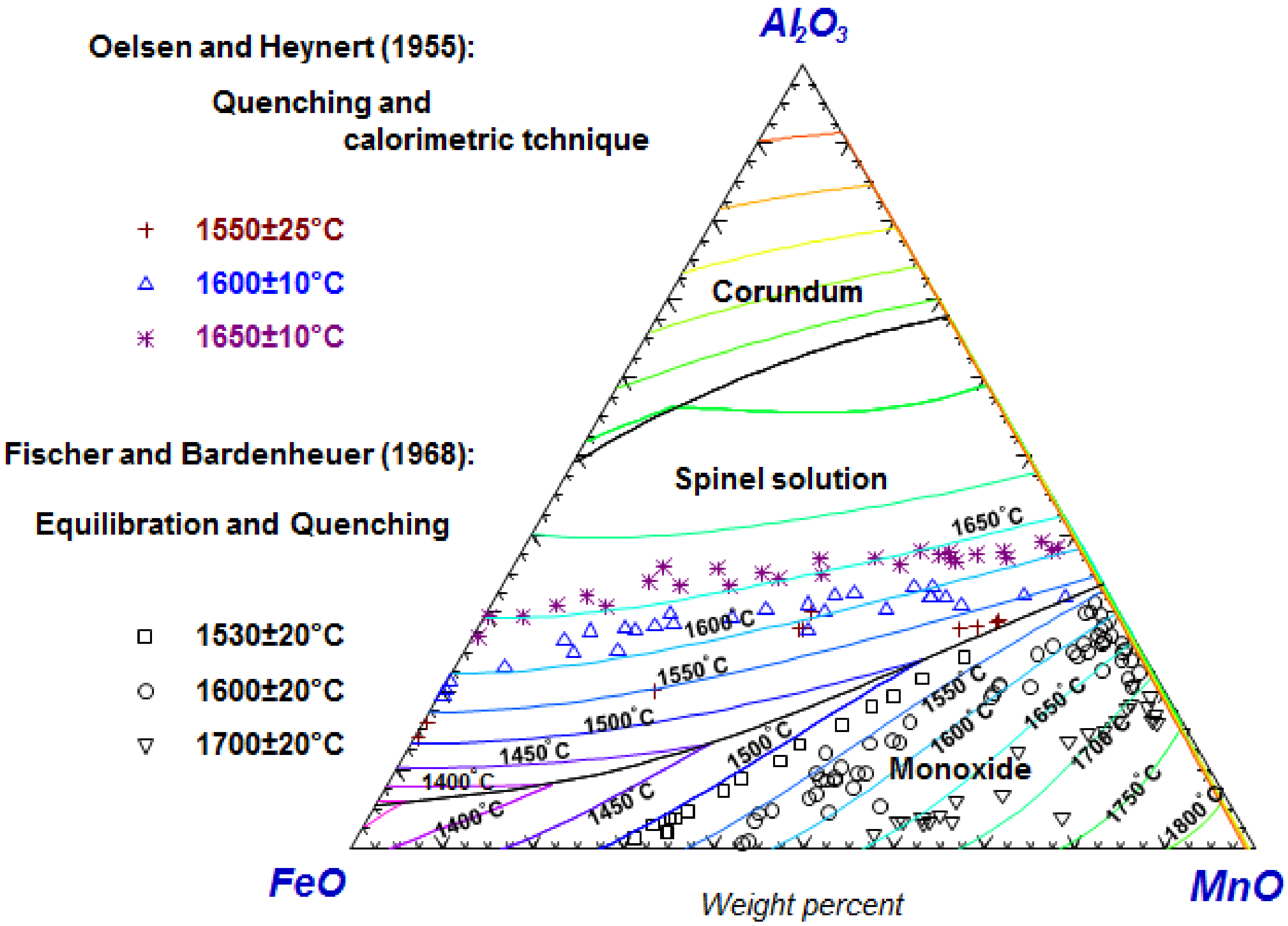

Figure 6.4: Calculated phase diagram for the FeO-MnO-Al_2O_3 system under reducing condition. The experimental points of Oelsen and Heynert [7] and Fischer and Bardenheuer [8] are also shown for comparison with calculated results.

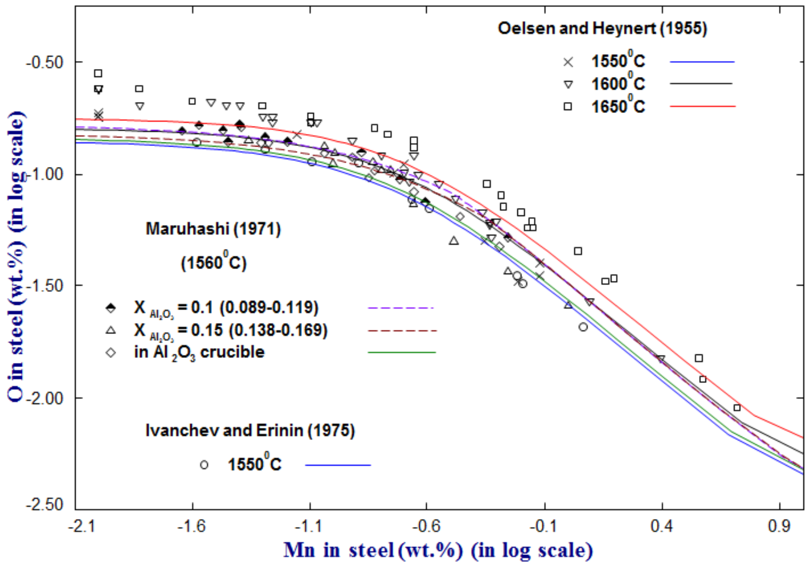

Figure 6.5: Calculated Mn-O equilibrium in liquid iron under FeO-MnO-Al_2O_3 slags at different conditions along with the experimental data by Oelsen and Heynert [7], Maruhashi [9] and Ivanchev and Erinin [10].

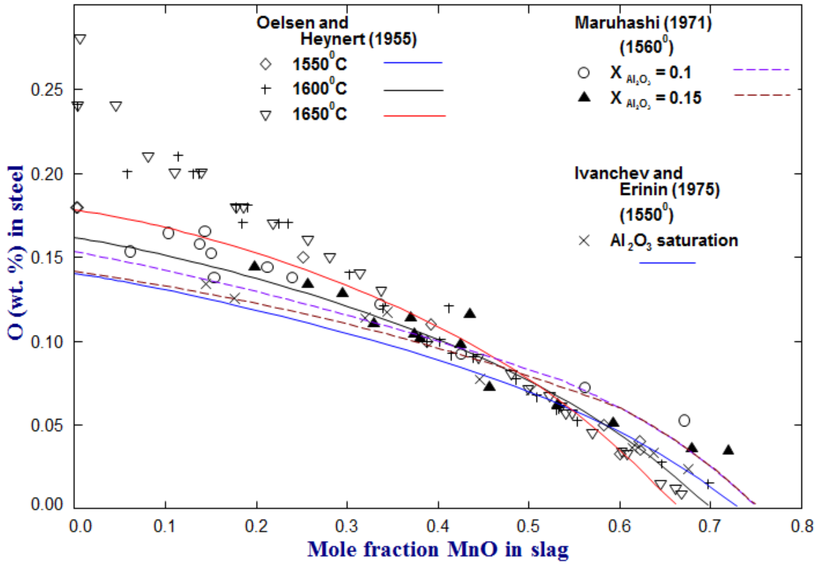

Figure 6.6: Calculated solubility of oxygen in molten iron as a function of mole fraction of MnO in FeO-MnO-Al_2O_3 slags at different conditions along with the experimental data by Oelsen and Heynert [7], Maruhashi [9] and Ivanchev and Erinin [10].

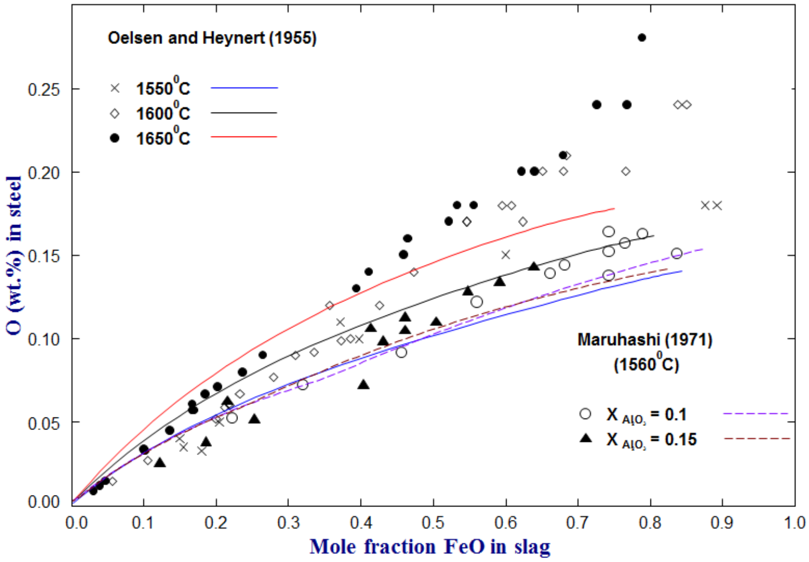

Figure 6.7: Calculated solubility of oxygen in molten iron as a function of mole fraction of FeO in FeO-MnO-Al_2O_3 slags at different conditions along with the experimental data by Oelsen and Heynert [7], Maruhashi [9] and Ivanchev and Erinin [10].

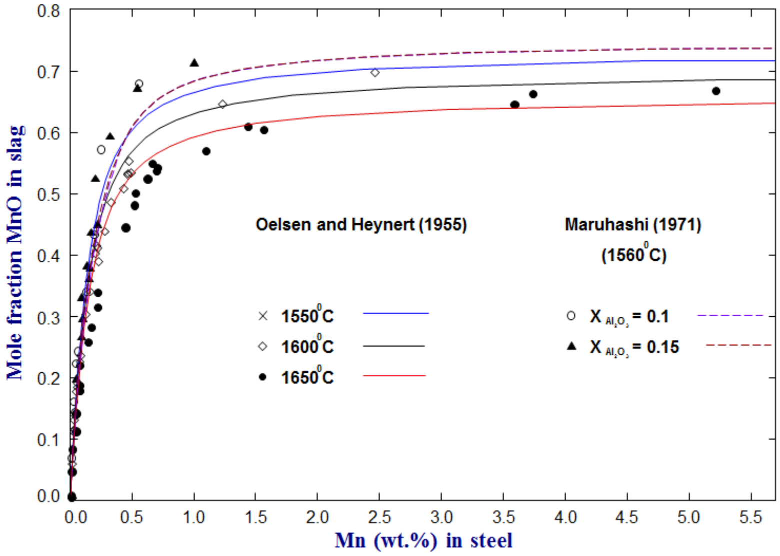

Figure 6.8: Calculated effect of manganese in molten iron as a function of mole fraction of MnO in FeO-MnO-Al_2O_3 slags at different conditions along with the experimental data by Oelsen and Heynert [7] and Maruhashi [9].

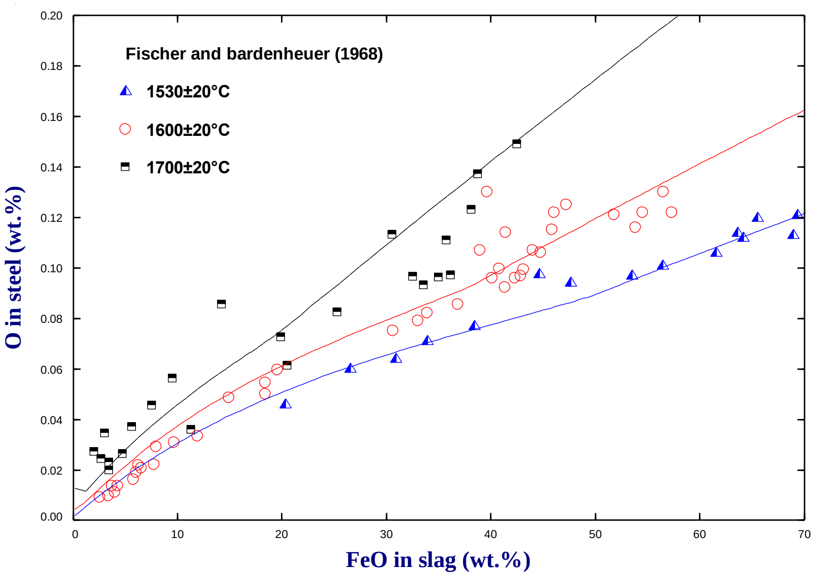

Figure 6.9: Calculated solubility of oxygen in molten iron as a function of mole fraction of FeO in FeO-MnO-Al_2O_3 slags at different temperatures along with the experimental data by Fischer and Bardenheuer [8].

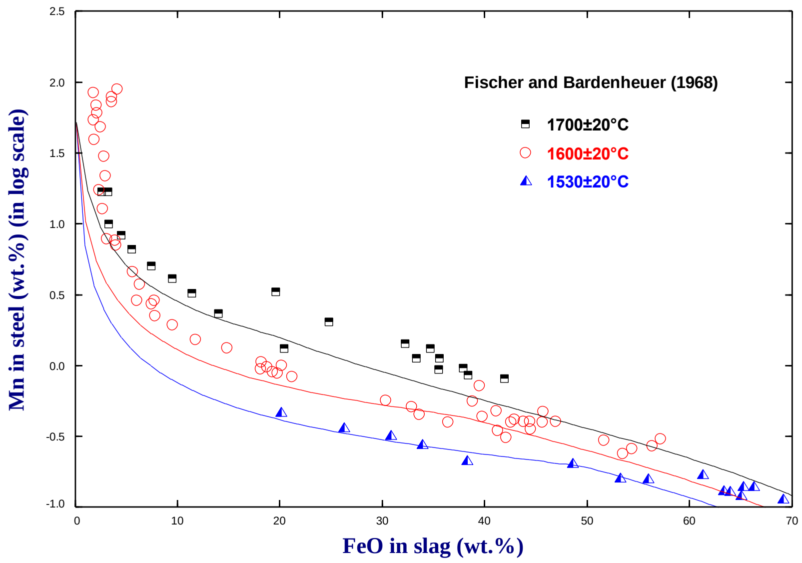

Figure 6.10: Calculated effect of manganese in molten iron as a function of mole fraction of FeO in FeO-MnO-Al_2O_3 slags at different temperatures along with the experimental data by Fischer and Bardenheuer [8].

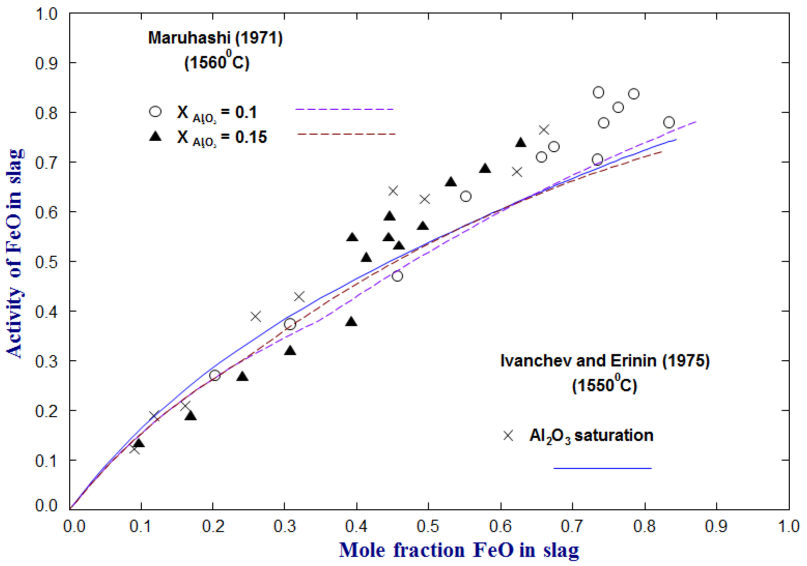

Figure 6.11: Calculated activities of FeO (liquid standard state) as a function of mole fraction of FeO in FeO-MnO-Al_2O_3 slags at different conditions along with the experimental data by Maruhashi [9] and Ivanchev and Erinin [10].

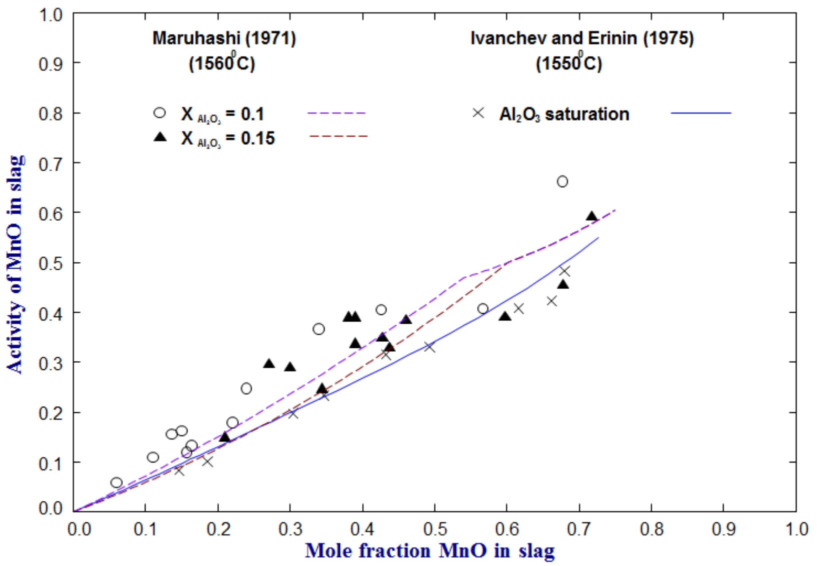

Figure 6.12: Calculated activities of MnO (liquid standard state) as a function of mole fraction of FeO in FeO-MnO-Al_2O_3 slags at different conditions along with the experimental data by Maruhashi [9] and Ivanchev and Erinin [10].

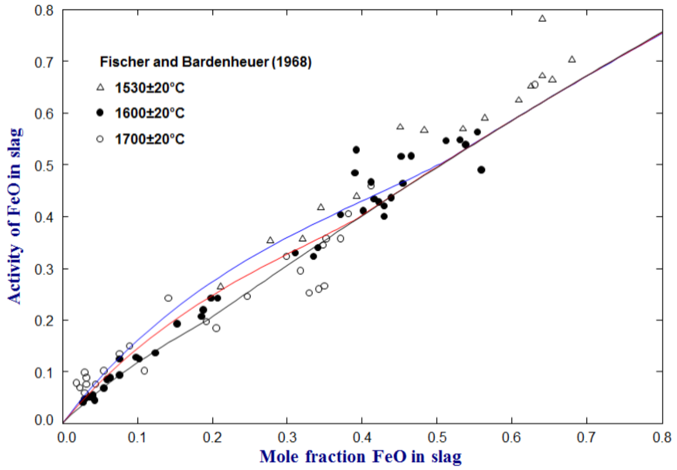

Figure 6.13: Calculated activities of FeO (liquid standard state) as a function of mole fraction of FeO in FeO-MnO-Al_2O_3 slags at different temperatures along with the experimental data by Fischer and Bardenheuer [8].

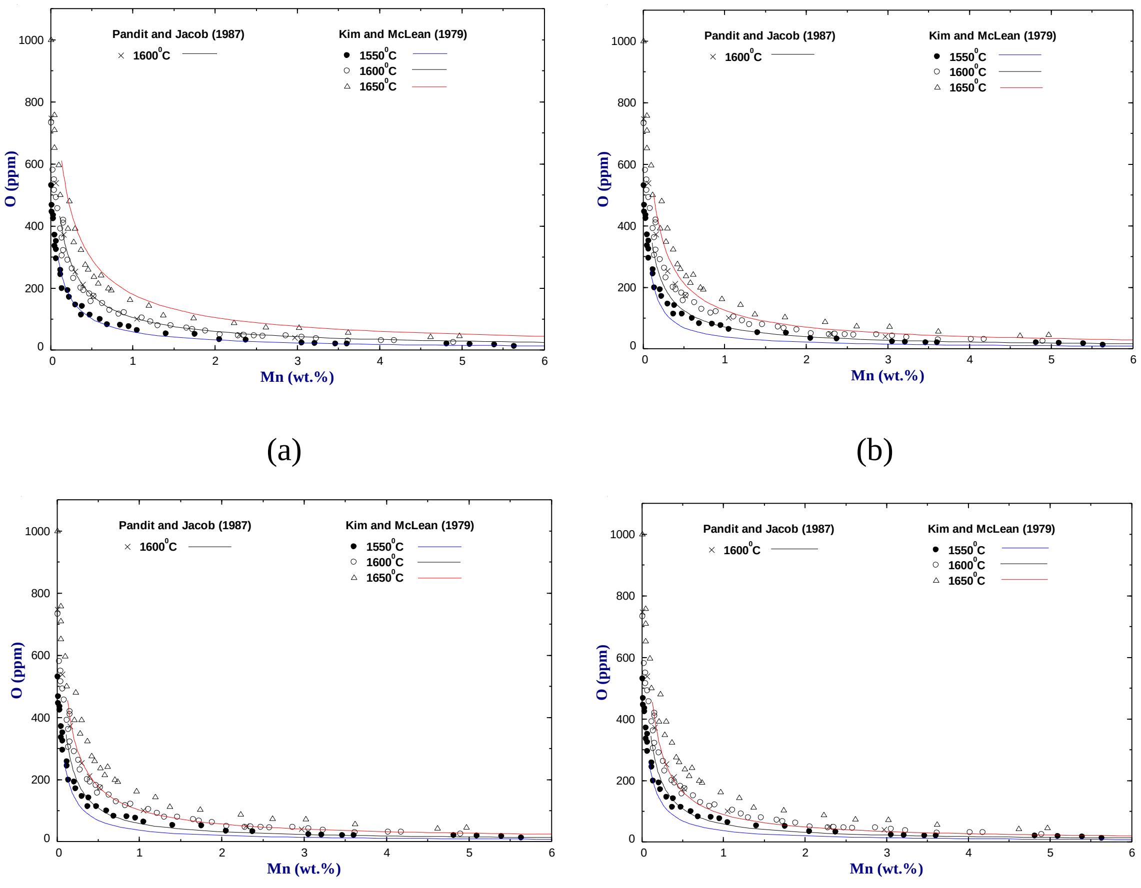

(a)

(b)

(c)

(d)

Figure 6.14: Calculated Mn-O equilibrium in liquid iron at equilibrium with spinel solid solution and (a) 0.1 moles of Alumina, (b) 0.5 moles of Alumina, (c) 1 moles of Alumina and (d) 2 moles of Alumina at different temperatures along with the experimental data by Kim and McLean [11] and Pandit and Jacob [12].

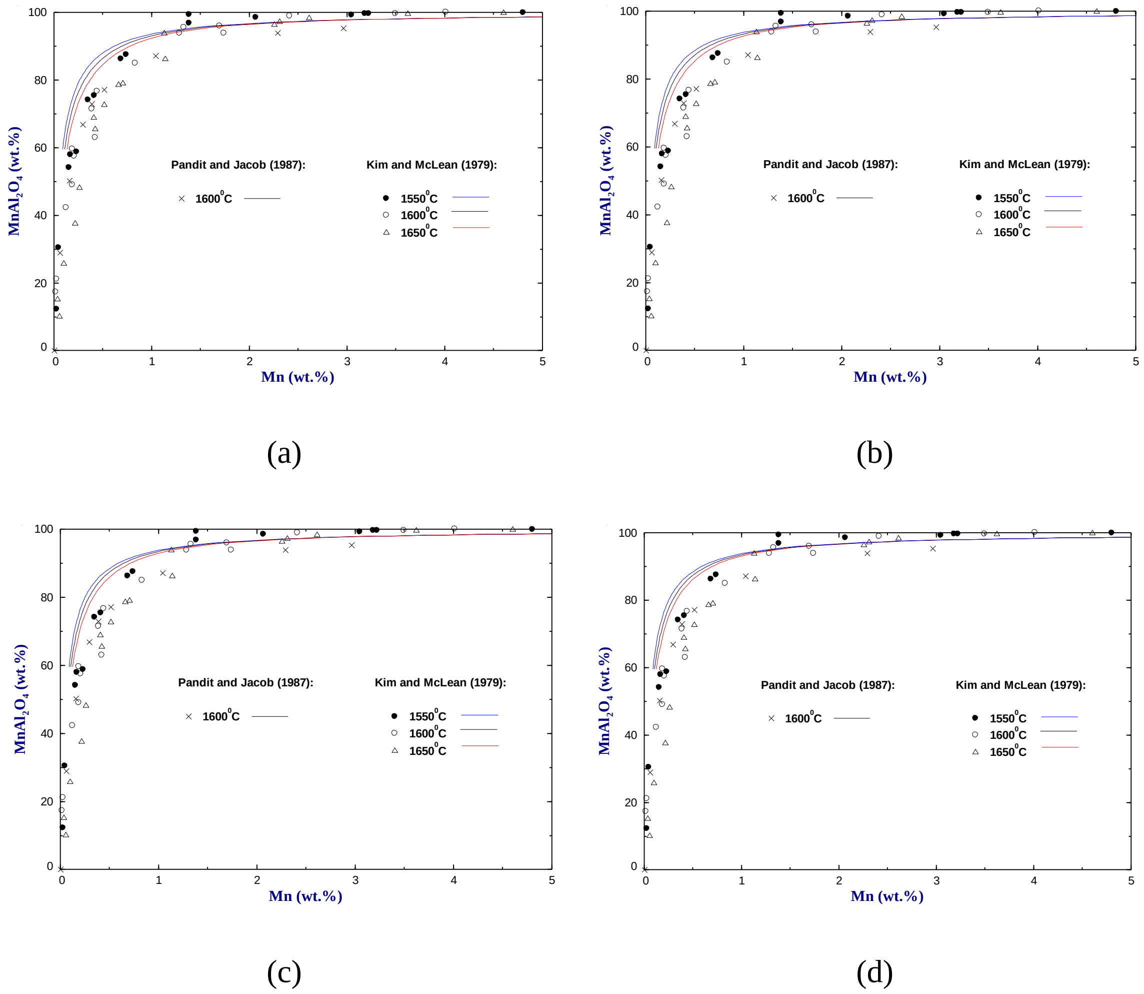

(a) (b)

(c) (d)

Figure 6.15: Calculated variation of the equilibrium composition of the spinel solid solution with manganese content of the alloy. The alloy and the spinel solid solutions are in equilibrium with (a) 0.1 moles of Alumina, (b) 0.5 moles of Alumina, (c) 1 moles of Alumina and (d) 2 moles of Alumina at different temperatures along with the experimental data by Kim and McLean [11] and Pandit and Jacob [12].

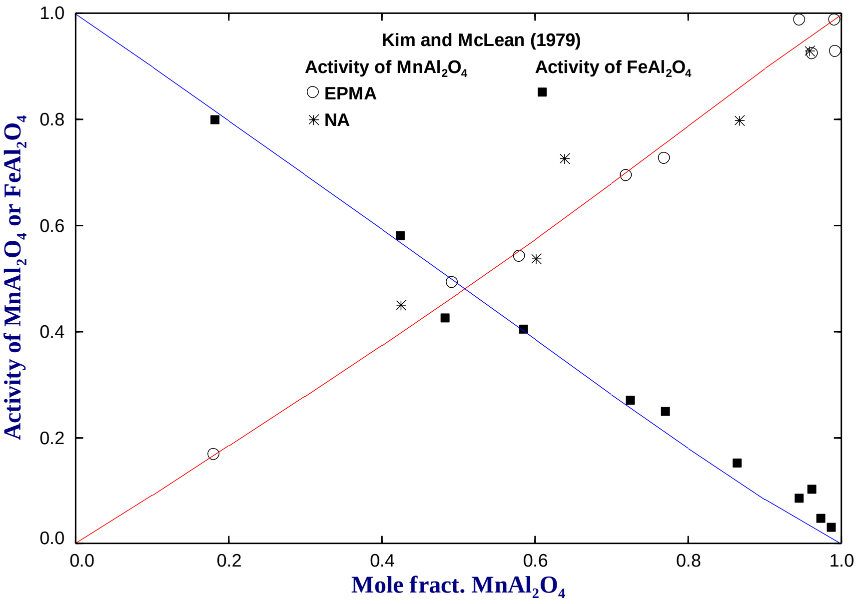

Figure 6.16: Calculated variation of activities with the composition of the components of the spinel solid solution at 1600°C along with the experimental data by Kim and McLean [11].

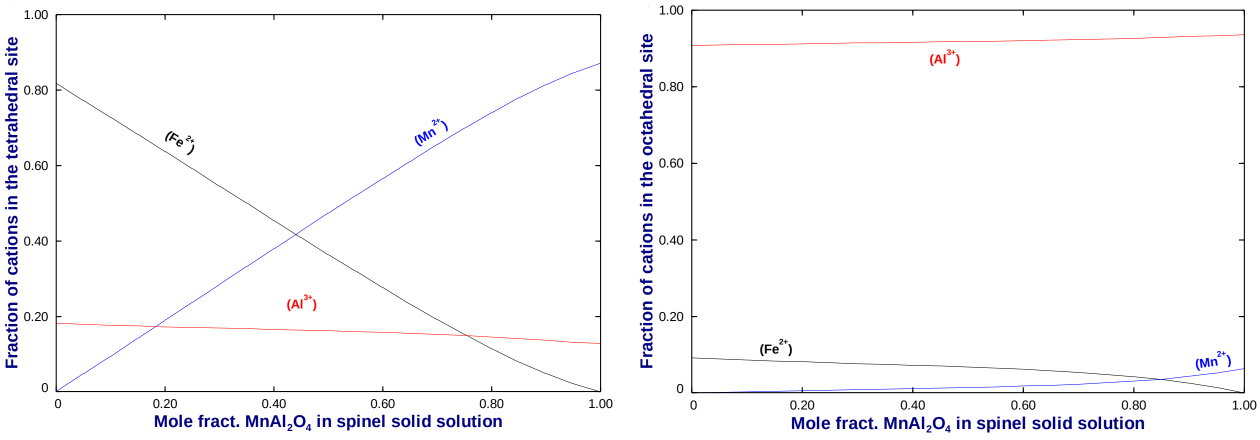

(a) (b)

Figure 6.17: Predicted cation distribution in the (a) Tetrahedral sites and (b) Octahedral sites of the spinel solid solution at 900°C.

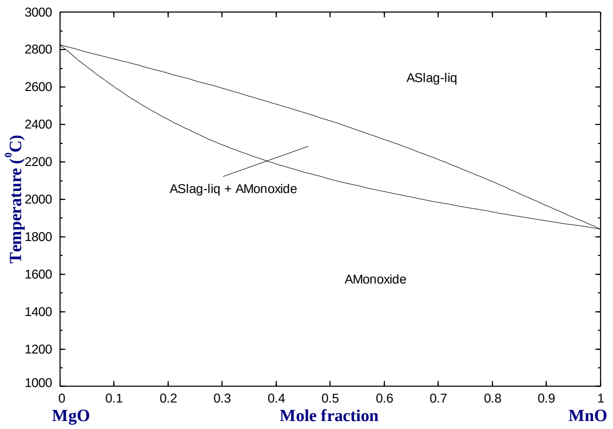

Figure 6.18: Phase Diagram for the MgO-MnO system by Wu *et al.* [1].

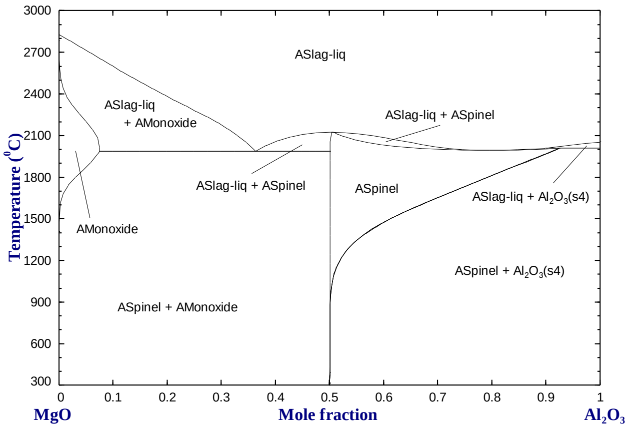

Figure 6.19: Phase Diagram for the MgO-Al_2O_3 system Jung *et al.* [13].

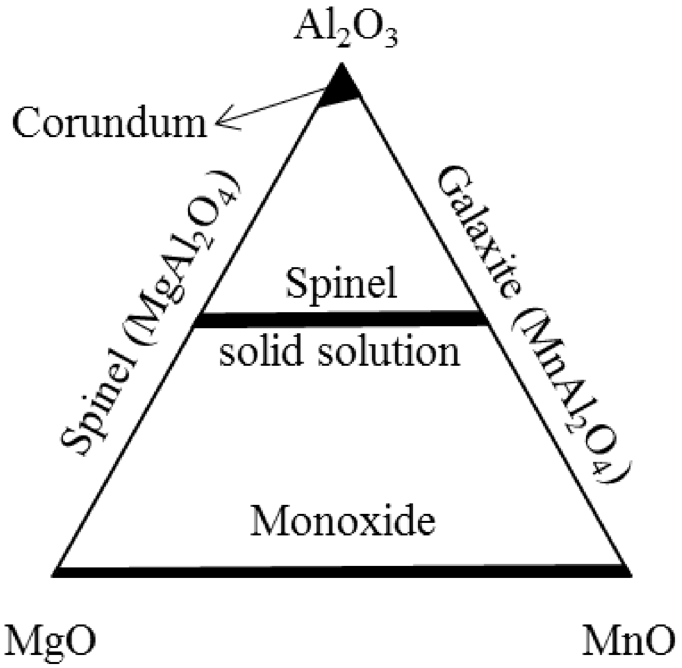

Figure 6.20: Schematic representation of phases in the MgO-MnO-Al_2O_3 system under reducing condition.

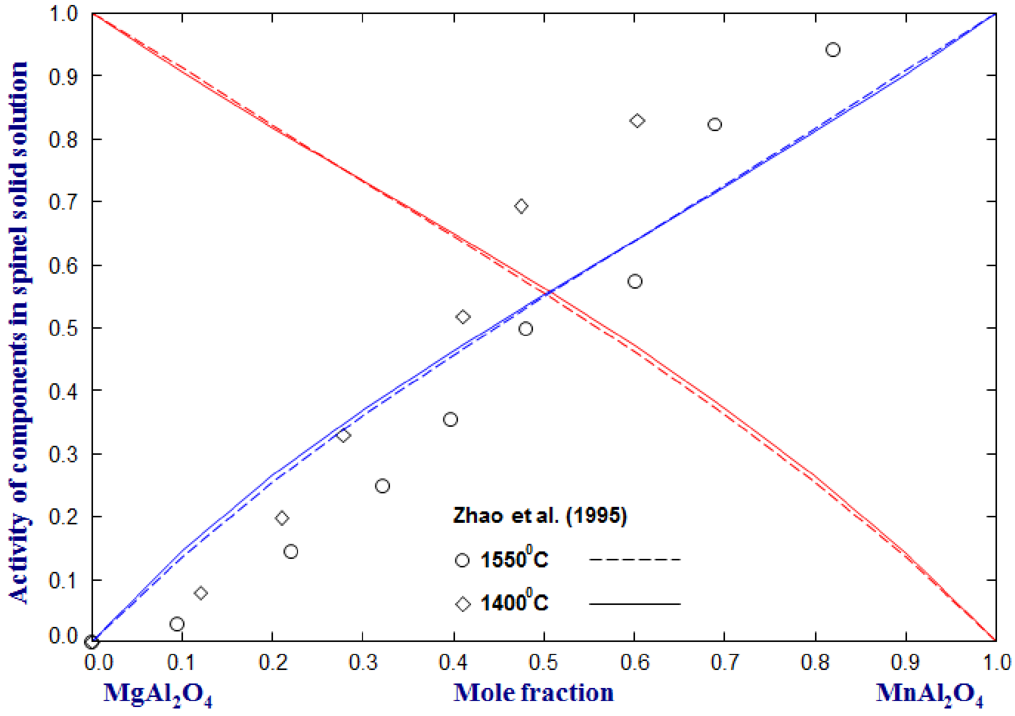

Figure 6.21: Calculated variation of activities of $MnAl_2O_4$ (in blue) and $MgAl_2O_4$ (in red) with their compositions at 1400°C and 1550°C along with the experimental data by Zhao *et al.* [15].

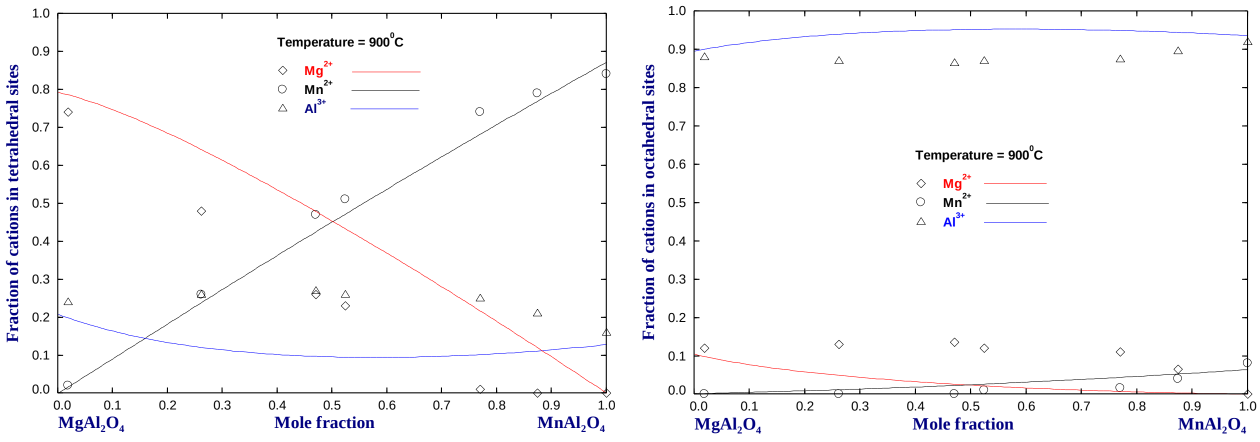

(a) (b)

Figure 6.22: Calculated cation distribution in the (a) Tetrahedral sites and (b) Octahedral sites of the spinel solid solution at 900°C along with the experimental data by Halenius [16].

CHAPTER 7

Conclusion

All the experimental data in the systems MnO-Al_2O_3, MnO-Al_2O_3-SiO_2, CaO-MnO-Al_2O_3, FeO-MnO-Al_2O_3, MgO-MnO-Al_2O_3 and CaO-MnO-Al_2O_3-SiO_2 have been critically assessed and the discrepancies in the available data have been resolved based on thermodynamically consistent way. All the models used in the present study were based on the structure of the solutions so that their configurational entropy was properly taken into account in the Gibbs energy of the solution. A set of optimized model parameters have been obtained which could reproduce all reliable thermodynamic and structural data as well as phase diagrams within the experimental error limits. Two spinel solid solutions (cubic and tetragonal) have been modeled separately in the study related to the binary MnO-Al_2O_3 system. The molten oxide and the bixbyite phases were also optimized in the course of the present work. Asymmetric Toop interpolation techniques were then used in order to predict the Gibbs energies of the ternary liquid solution present in the MnO-Al_2O_3-SiO_2 system with SiO_2 as an asymmetric component and two small ternary parameters were added. In case of the CaO-MnO-Al_2O_3, FeO-MnO-Al_2O_3 and MgO-MnO-Al_2O_3 systems, asymmetric Toop interpolation technique was used with Al_2O_3 as the asymmetric component without any ternary parameters. The calculations in the ternary systems were in good agreement with the available experimental data within the experimental error.

As an application to industrial processes, the thermodynamic databases developed in this study were used to carry out calculations related to inclusion engineering in the steelmaking process. The results obtained from these calculations reiterate the usefulness of the optimized databases.